

# Cooling an electron gas using quantum dot based electronic refrigeration

Jonathan Robert Prance

August 28, 2009

Downing College, University of Cambridge

A thesis submitted for the degree of Doctor of Philosophy

# Preface

---

The work presented in this thesis was carried out in the Semiconductor Physics group at the Cavendish Laboratory from October 2004 to August 2009.

This dissertation is the result of my own work and includes nothing which is the outcome of work done in collaboration except where specifically indicated in the text. It has not been submitted, in whole or in part, for a degree, diploma or other qualification at any other University.

This thesis is less than 60,000 words long.

# Summary

---

Studies of two-dimensional electron gases (2DEGs) in semiconductors form an active and productive field of condensed matter physics research. As well as having interesting inherent properties, they are used as the foundation for constructing various nano-scale electronic devices, such as quantum wires and quantum dots.

Conventionally, low temperature measurements of 2DEGs are made by cooling the sample to 1.5 K with liquid Helium-4, to 300 mK with liquid Helium-3, or even down to a few mK using a dilution refrigerator. However, at lower temperatures the electron gas becomes increasingly decoupled from the lattice in which it resides. Below  $\sim 1$  K the coupling can be weak enough for the electron gas to be significantly elevated in temperature due to parasitic heating.

In this thesis we present the experimental and theoretical investigation of a refrigeration scheme that has the potential to cool 2DEGs below the temperatures currently available. Cooling to ever lower temperatures would be beneficial for studying fragile fractional quantum Hall states, non-Fermi-liquid behaviour in bilayer 2DEGs, or interactions like the Kondo effect that occur between quantum dots and 2DEGs.

The scheme we investigate is called the Quantum Dot Refrigerator (or QDR) and is based upon the energy selective transport of electrons through the single-particle states of quantum dots. By using a pair of dots, both hot electrons and hot holes can be selectively removed from an otherwise electrically isolated 2DEG. The result is a net current that continuously removes heat. This type of refrigerator is best suited to be used in conjunction with a dilution fridge or Helium-3 system to provide a final stage of cooling. The scheme was first investigated theoretically in 1993 by Edwards et al. but, to our knowledge, has never before been demonstrated experimentally.

We detail the fabrication and measurement of a QDR device that is designed to cool an isolated  $6 \mu\text{m}^2$  2DEG. In order to interpret the behaviour of the device, a model was developed to take account of electrostatic interactions between the components of the system (the quantum dots and the isolated 2DEG). Electrostatic interactions were found to be significant for our design, but were neglected in previous work. Our model predicts that their presence complicates, but does not invalidate, the principle of operation of a QDR.

By comparing measurements of the current through the QDR with predictions of the model, we show that the observed behaviour is consistent with cooling of the isolated 2DEG by up to 100 mK at ambient temperatures around 250 mK. Although these temperatures are well within the reach of conventional refrigeration techniques, the results are a compelling proof-of-concept demonstration that the QDR principle is sound and can achieve significant refrigeration in the right conditions.

Finally, we discuss future directions for improving QDR performance and characterisation, and for lowering the achievable base temperature. We also suggest how QDRs could be used to provide cold reservoirs for a nano-scale electronic device, and explore the limitations that would apply to such an experiment.

# Acknowledgements

---

While undertaking the work presented in this thesis I was fortunate to have the invaluable support of several members of the Semiconductor Physics group, whom I would like to thank. Foremost is my supervisor, Charles Smith, for his constant support and trust, and his ready supply of thought-provoking ideas. Simon Chorley and Jon Griffiths both assisted at various stages, from device fabrication to operating the fridge, and were always willing to discuss problems or unexpected results. Ian Farrer and Paola Atkinson grew the material that I used to make my devices, and the e-beam writing was done by Dave Anderson and Jon Griffiths. Adam Thorn installed and maintains the group's distributed computing infrastructure (part of CamGrid), without which my analysis would have taken significantly longer. I also gratefully acknowledge funding from the UK EPSRC, Toshiba Research Europe, and Downing College.

The overall experience of working towards a PhD has been a combination of satisfaction, frustration, fun, and tedium. Occasionally it was all these in a single day. However, I have learnt a huge amount and I am indebted to all the people who gave their time and shared their knowledge to help make that the case. In addition to everyone mentioned above, I would like to thank Chris Ford, Francois Sfigakis, Kanti das Gupta, Rolf Crook, Ken Cooper, Lee Basset and Karl Petersson for their assistance and advice on numerous subjects related and tangential to my project.

Away from the lab my time has been made all the more enjoyable by friends in, around, or passing through Cambridge. Thanks (in no particular order) to Matt C, Saff, James, Matt S, Henry, Ale, Helga, Cos, Camille, Ana, Frieda, Rich, Nico and Tristan, for helping to take my mind off work when I needed it most.

Finally I would like to thank my whole family for their perpetual encouragement and support, and Marcie for her love and patience over the last several years.

# Contents

---

<b>Preface</b>	<b>i</b>
<b>Summary</b>	<b>ii</b>
<b>Acknowledgements</b>	<b>iv</b>
<b>Contents</b>	<b>vii</b>
<b>List of figures</b>	<b>x</b>
<b>1 Introduction</b>	<b>1</b>
1.1 Motivation . . . . .	1
1.2 Outline . . . . .	3
1.3 Publications . . . . .	4
<b>2 Background</b>	<b>5</b>
2.1 Low-dimensional electronic devices . . . . .	5
2.1.1 The 2D electron gas in GaAs . . . . .	7
2.1.2 Confinement with surface gates . . . . .	8
2.2 Quantum dots . . . . .	10
2.2.1 Coulomb blockade . . . . .	10
2.2.2 Quantum confinement . . . . .	11
2.2.3 First order transport . . . . .	13
2.2.4 Higher order transport . . . . .	17

2.2.5	Dots as thermometers . . . . .	18
2.2.6	Point-contact detectors . . . . .	19
2.3	Inelastic scattering of 2D electrons . . . . .	20
2.3.1	Electron-electron scattering . . . . .	20
2.3.2	Electron-phonon scattering . . . . .	21
2.4	Hot carriers . . . . .	23
2.4.1	Reducing unintentional heating . . . . .	23
2.4.2	Intentional heating . . . . .	24
2.5	Low temperature electronic refrigeration . . . . .	25
2.5.1	Superconducting coolers . . . . .	27
2.5.2	The quantum dot refrigerator . . . . .	31
<b>3</b>	<b>Quantum dot refrigerator: experimental realisation</b>	<b>35</b>
3.1	Design . . . . .	35
3.1.1	Size of the cooled electron gas . . . . .	36
3.1.2	Size of the quantum dots . . . . .	38
3.2	Fabrication . . . . .	40
3.3	Measurement setup . . . . .	41
3.4	Device characterisation . . . . .	43
3.4.1	Quantum dots . . . . .	43
3.4.2	Central region spectroscopy . . . . .	48
3.4.3	Fully isolated central region . . . . .	53
3.5	Thermometry measurements . . . . .	56
3.6	Preliminary results . . . . .	61
<b>4</b>	<b>Quantum dot refrigerator: analysis</b>	<b>67</b>
4.1	Temperature dependence results . . . . .	68
4.2	Simple QDR model . . . . .	71
4.2.1	Master equation . . . . .	71
4.2.2	Predictions . . . . .	74
4.2.3	Analysis . . . . .	77
4.3	Full QDR model . . . . .	82
4.3.1	Electrostatics . . . . .	82
4.3.2	Thermal equilibrium . . . . .	86
4.3.3	Predictions . . . . .	91
4.3.4	Determining capacitances . . . . .	97

4.3.5 Analysis . . . . .	99
<b>5 Future measurements and improvements</b>	<b>113</b>
5.1 A quantum dot thermometer . . . . .	113
5.1.1 Measurement setup . . . . .	115
5.1.2 Results . . . . .	115
5.2 An experimental platform . . . . .	121
<b>6 Conclusions</b>	<b>125</b>
<b>A Wafers and devices</b>	<b>I</b>
A.1 Wafers . . . . .	I
A.2 Devices . . . . .	I
<b>B Measurement setup</b>	<b>II</b>
B.1 Current-to-voltage amplifier . . . . .	II
B.2 Cold finger . . . . .	III
B.3 Room temperature electronics . . . . .	IV
<b>C 2DEG thermal coupling</b>	<b>V</b>
<b>References</b>	<b>VII</b>

# List of Figures

---

2.1	Quantum well formation . . . . .	6
2.2	HEMT heterostructure . . . . .	8
2.3	Lateral 2DEG confinement . . . . .	9
2.4	Quantum dot equivalent circuit. . . . .	12
2.5	Dot energy levels with low bias. . . . .	14
2.6	Dot energy levels with high bias. . . . .	15
2.7	Non-linear transport through a quantum dot . . . . .	16
2.8	Co-tunnelling and Kondo processes. . . . .	17
2.9	Temperature dependence of non-linear transport. . . . .	19
2.10	Measurements of 2D carrier scattering . . . . .	21
2.11	Heat flows for normal and direct 2DEG cooling . . . . .	26
2.12	Tunnelling between a normal metal and a superconductor . . . . .	28
2.13	Typical SINIS cooler. . . . .	29
2.14	Energy levels of a QDR . . . . .	32
3.1	QDR device design . . . . .	36
3.2	QDR operating regimes . . . . .	39
3.3	Optical lithography steps. . . . .	40
3.4	PMMA lift-off process . . . . .	41
3.5	SEM images of a completed QDR device. . . . .	42
3.6	Differential conductance measurement setup . . . . .	44
3.7	Direct current measurement setup . . . . .	45

---

3.8	Coulomb blockade signature . . . . .	46
3.9	Coulomb diamonds of quantum dots . . . . .	47
3.10	Excited state in the top dot . . . . .	48
3.11	Outline of central region spectroscopy measurement. . . . .	49
3.12	1D-0D-2D tunnelling results . . . . .	52
3.13	Central region Coulomb blockade . . . . .	54
3.14	Central region Coulomb blockade 2 . . . . .	55
3.15	Capacitive coupling . . . . .	57
3.16	Non-linear DC measurement of the left dot . . . . .	59
3.17	Electron temperature analysis example . . . . .	60
3.18	Electron temperature results . . . . .	61
3.19	Full QDR transport . . . . .	62
3.20	Conduction point with large biases . . . . .	63
3.21	Cross coupling compensation 1 . . . . .	65
3.22	Cross coupling compensation 2 . . . . .	66
3.23	Conduction point with low bias . . . . .	66
4.1	Outline of QDR current line-shape . . . . .	68
4.2	Conduction points at various temperatures . . . . .	69
4.3	Line-shapes while probing central region . . . . .	70
4.4	QDR charge state transitions . . . . .	72
4.5	Simple model results. . . . .	75
4.6	Analytic solution for QDR current . . . . .	77
4.7	Fitting analytic prediction to data 1. . . . .	79
4.8	Fitting analytic prediction to data 2. . . . .	80
4.9	Results of comprehensive fitting. . . . .	80
4.10	Equivalent capacitor network. . . . .	83
4.11	Large bias predictions of the capacitor network. . . . .	85
4.12	Origin of large bias conduction point shape 1. . . . .	87
4.13	Origin of large bias conduction point shape 2. . . . .	88
4.14	Full model prediction for an ideal QDR . . . . .	93
4.15	Full model prediction including back-action. . . . .	94
4.16	Effect of back-action on QDR performance. . . . .	95
4.17	Effect of off-resonance tunnelling on QDR performance. . . . .	96
4.18	Determining top dot capacitances. . . . .	98
4.19	Determining central region capacitances. . . . .	100

---

4.20	Conduction points shapes. . . . .	102
4.21	Example fit to a conduction point. . . . .	103
4.22	Fitting full QDR model to measurements. . . . .	104
4.23	Dependence of line-shape on $T_b$ . . . . .	105
4.24	Fitting full QDR model to averaged measurements. . . . .	107
4.25	Failure of the constant $T_C$ model. . . . .	110
4.26	Lowest temperature results. . . . .	112
5.1	Dot thermometer measurement setup. . . . .	116
5.2	Dot charge-state detection. . . . .	117
5.3	Dot charge-state detection under bias. . . . .	118
5.4	Tuning dot barriers. . . . .	119
5.5	Single electron counting. . . . .	122
5.6	Cooling a pair of biased reservoirs. . . . .	123
A.1	Structure of a standard 90nm HEMT . . . . .	I
C.1	Heat flows in a typical 2DEG device. . . . .	VI

# Chapter 1

## Introduction

---

This thesis details the design, fabrication and measurement of a device for cooling a two-dimensional electron gas (2DEG) with an area of  $6 \mu\text{m}^2$  at temperatures below  $\sim 1$  K. The cooling is achieved by the energy selective injection and removal of electrons from the 2DEG using a pair of quantum dots [1, 2]. To our knowledge, this has never previously been demonstrated experimentally.

While our device is only found to demonstrate cooling at temperatures already easily accessible by dilution refrigerators ( $\sim 100$  mK), this is not a fundamental limitation of the scheme. In principle, Quantum Dot Refrigerators (QDRs) can operate at arbitrarily low temperatures. They are therefore an intriguing candidate for cooling 2DEGs to the sub-mK regime, which has yet to be achieved using more conventional techniques. In this chapter we discuss the motivation for creating such a refrigerator for 2DEGs and outline the structure of this thesis.

### 1.1 Motivation

A 2DEG is formed when free electrons are confined to planar region so thin that they behave as if they were truly two-dimensional. This situation can exist in various materials, but often 2DEGs are created intentionally in layered semiconductor structures (heterostructures). 2DEGs have been shown to be highly interesting physical systems, as typified by the discovery of the quantum Hall effect in 1980 [3], and their behaviour at low temperatures continues to be the subject of active research. In particular, significant efforts are currently focused on studying

the fractional quantum Hall effect, largely because of its potential for realising topological quantum computation [4]. These measurements require extremely low temperatures ( $\lesssim 10$  mK) because of the fragile nature of the fractional quantum Hall states involved.

As well as possessing interesting inherent behaviour, 2DEGs are also the foundation on which a many nano-scale electronic devices are created. A vast number of experiments have studied quantum wires and quantum dots that have been made using semiconductor heterostructures combined with lithographically patterned gate electrodes on the heterostructure's surface. The result is a device that is formed using a small part of the 2DEG in the material. The remainder of the 2DEG is usually used as an electrical reservoir to make contact with the device. When the coupling between a device and its 2DEG reservoirs is strong, the device's behaviour can be strongly affected by the properties of the reservoirs. Phenomena such as the Kondo effect, which involves many-body interactions between an isolated spin trapped in a quantum dot and the sea of nearby spins in the 2DEG, are often strongly temperature dependent. In general, the weaker the interaction, the colder the 2DEG has to be in order to observe it; for example, a recent measurement of the two-channel Kondo effect required a temperature of approximately 10 mK [5].

The usual technique for cooling 2DEG samples to the temperature required for an experiment is to use a Helium-3 cryostat or dilution refrigerator. The latter can cool the crystal lattice of the device down to  $\sim 1$  mK. However, it is common to find that, unless great care is taken with the experimental setup, the temperature of a 2DEG is significantly higher than the lattice it resides in. The reason for this is that the rate of inelastic scattering between 2D electrons and lattice phonons decreases with temperature. This reduces the energy transfer and, therefore, the thermal link between the 2DEG and the lattice. With a weak thermal link, parasitic heating due to noise introduced by the electrical connections can be enough to elevate the 2DEG temperature significantly. The reduction of noise in the measurement setup is therefore of vital importance in obtaining a low temperature electron gas. Heating can also arise from the absorption of environmental radiation and for this reason cold radiation shields are often employed.

It is possible for the thermal contact between the 2DEG and the lattice of the device to become so weak that the 2DEG's primary cooling path is through its electrical connections. Effectively thermalising the wires for these connections to

the coldest point of the dilution fridge is therefore also important. However, this too becomes increasingly difficult with decreasing temperature, since the effectiveness of any thermal contacts used for heat-sinking will also decrease.

One possible solution to the challenge of cooling 2DEGs to sub mK temperatures is to employ direct electronic refrigeration. In this case, heat is pumped out of the 2DEG directly by selectively removing hot electrons and injecting colder ones. The decreasing inelastic electron-phonon scattering rate then becomes advantageous, since it should allow the 2DEG to be cooled below the temperature of the lattice. In this thesis we present the experimental investigation of one particular electronic refrigeration scheme – the Quantum Dot Refrigerator [1, 2] – that has the potential to cool 2DEGs to the sub-mK regime. While the proof-of-concept device that we study did not achieve these exceptionally low temperatures, we present its investigation to demonstrate the soundness of the refrigeration scheme and to inform the design of future experiments.

In addition to providing cooling, QDR devices could be used to study the energy flows in 2DEGs. For example, by observing the power required to change the temperature of a 2DEG, the magnitude and temperature dependence of inelastic electron-phonon scattering could be measured. Also, the operation of the QDR will be sensitive to how quickly the 2DEG can re-equilibrate after the injection (or removal) of electrons at a fixed energy. This energy relaxation is expected to be dominated by inelastic electron-electron scattering. A QDR device could therefore be used to investigate both inelastic electron-phonon and electron-electron scattering in 2D systems.

Finally, although not considered in detail in this thesis, it is possible that a Quantum Dot Refrigerator could eventually be implemented in material systems other than a semiconductor electron gas. Indeed, it is not even necessary for the cooled electron gas to be two-dimensional. The most stringent requirements are placed on the quantum dots, which must be small enough to possess well spaced single-particle states. This is already known to be achievable in systems such as nanowires [6] and carbon nanotubes [7].

## 1.2 Outline

- **Chapter 2** introduces several topics that are of particular relevance to the work in this thesis. An explanation of electronic transport through quantum

dots is given. The difficulties inherent in cooling semiconductor 2D electron gases are then explored in detail, and previous work on several electronic refrigeration schemes is reviewed. Finally, we summarise the original proposal of the Quantum Dot Refrigerator.

- **Chapter 3** details the design, fabrication and measurement of a QDR device. Extensive characterisation of the device is presented to establish that it fulfills the known requirements for achieving refrigeration.
- In **Chapter 4** we present measurements of the QDR device operating in a regime where cooling is expected. To interpret the results, a model is developed. By comparing the predictions of the model with the data, it is shown that the behaviour of the device is consistent with active cooling of the central region.
- **Chapter 5** discusses future directions for investigating QDRs. The details of operating a non-invasive, quantum dot thermometer are demonstrated experimentally. Techniques for using QDRs in conjunction with other experiments are also discussed.
- **Chapter 6** summarises the work presented in this thesis and presents the key conclusions.

## 1.3 Publications

The main results of the QDR experiment have been published in:

- J. R. Prance, C. G. Smith, J. P. Griffiths, S. J. Chorley, D. Anderson, G. A. C. Jones, I. Farrer, and D. A. Ritchie, *Electronic refrigeration of a two-dimensional electron gas*, Phys. Rev. Lett. **102**(14), 146602 (2009).

The above paper was selected for a *Viewpoint* summary in the APS journal *Physics*, published as:

- Jason R. Petta, *Electronic refrigeration on the micron scale*, Physics **2**, 27 (2009)

# Chapter 2

## Background

---

### 2.1 Low-dimensional electronic devices

Quantum mechanics predicts that a particle's momentum will assume one of a discrete set of values when its motion is confined to a finite region of space. A simple example is the well-known 'particle-in-a-box' problem, where solving the Schrödinger equation in a box with side lengths  $L_x$ ,  $L_y$  and  $L_z$  results in states with wavevectors ( $\underline{k}$ ) and energies ( $E$ ) given by:

$$\underline{k} = \left(\frac{n_x\pi}{L_x}\right)\hat{i} + \left(\frac{n_y\pi}{L_y}\right)\hat{j} + \left(\frac{n_z\pi}{L_z}\right)\hat{k} \quad (2.1)$$

$$E = \frac{\pi^2\hbar^2}{2m} \left[ \left(\frac{n_x}{L_x}\right)^2 + \left(\frac{n_y}{L_y}\right)^2 + \left(\frac{n_z}{L_z}\right)^2 \right] \quad (2.2)$$

where the values  $n_x$ ,  $n_y$  and  $n_z$  are positive, non-zero integers. Traditional electronic devices have length scales so large that the separations between the quantised wavevectors and energies can be safely ignored. However, technological advances in semiconductor processing, nanotechnology and low-temperature measurement techniques have opened the possibility of making small enough electronic devices, and measuring them at low enough temperatures, for the quantisation of electronic states to be revealed.

One of the most widely studied low-dimensional electronic systems is the two-dimensional electron gas (2DEG) in semiconductors, in which carriers are confined

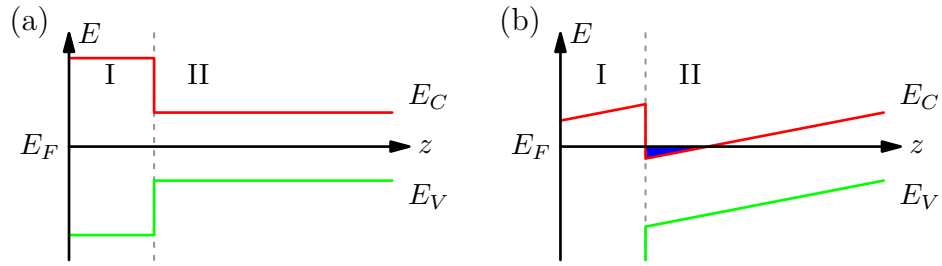


**Figure 2.1:** The formation of a quantum well at a heterointerface. Both plots show the energies of the conduction and valance bands ( $E_C$  and  $E_V$ ) as a function of depth into the material ( $z$ ). The step in band-gap energy ( $E_{gap} = E_C - E_V$ ) between materials I and II creates discontinuities in both bands leading to the situation in (a). With appropriate doping, or the application of an external electric field, the conduction band can be populated with free carriers in a narrow range of  $z$ . This is shown by the small blue region in (b).

in one direction ( $z$ ) on a length scale comparable to the Fermi wavelength. Confinement in the other two directions ( $x$  and  $y$ ) is over large enough distances for the quantisation of momentum in the  $x$ - $y$  plane to be neglected. The energy of a carrier with effective mass  $m^*$  can therefore be written as:

$$E_{2D} = E_n + \frac{\hbar^2}{2m^*} k_{2D}^2 \quad (2.3)$$

where  $\underline{k}_{2D}$  is the wavevector in the  $x$ - $y$  plane, which is assumed to be a continuous quantity, and  $E_n$  is the energy associated with the  $n^{\text{th}}$  quantised wavevector component in the  $z$  direction. For example, in an infinite square well of width  $L_z$ , Equation 2.2 shows that  $E_n = (\pi^2 \hbar^2 n^2) / (2m^* L_z^2)$ . Ideally,  $E_{n=2}$  is large enough that only states with  $n = 1$  are populated. The carriers then behave as if they were purely two-dimensional.

The confinement potential for a semiconductor 2DEG is created by engineering the band-structure in the material. Typically the 2DEG is formed at the interface between two semiconductors with different band gaps, or between a semiconductor and an insulator. In both cases the conduction band edge has a discontinuity at the interface. A potential well is formed in the conduction band by bending the band structure with doping or an externally applied electric field (see Figure 2.1). Once the bottom of the well is pulled below the Fermi energy, it becomes populated with electrons that form the 2DEG. (Alternatively, the valance band can be pushed above the Fermi energy to form a 2D hole gas.)

Measurements of 2D electron and hole gases at low temperatures have lead

to the discovery of a wealth of physical phenomena too extensive to detail fully here. Probably the most notable are the quantum Hall effect [3], the fractional quantum Hall effect [8], and the spin Hall effect [9, 10]. All exhibit fundamentally quantum mechanical behaviour in macroscopically measurable quantities, providing new physical insights.

In the remainder of this section we explain in detail the GaAs/AlGaAs 2DEG system, which all the original work presented in this thesis utilised. We also discuss how the patterning of gate electrodes on the surface of a 2DEG device can allow even more physical effects to be studied, including the creation and manipulation of lower dimensional electron gases.

### 2.1.1 The 2D electron gas in GaAs

The band gap of the semiconductor alloy AlGaAs depends on the Al fraction ( $x$ ) via the relation  $E_{gap} = (1.424 + 1.247x)\text{eV}$  [11]. But while  $E_{gap}$  changes significantly with  $x$ , the lattice constant changes little: for GaAs ( $x = 0$ ) the lattice constant is  $5.635 \text{ \AA}$ , while for AlAs ( $x = 1$ ) it is  $5.660 \text{ \AA}$ . Layers of AlGaAs and GaAs can therefore be grown on top of each other with very little lattice mismatch, minimising the strain and the density of misfit dislocations at the interface. The GaAs/AlGaAs system therefore provides an excellent way to produce high quality interfaces with a tunable band-structure.

The layered structure that forms a 2DEG device is called the ‘heterostructure’. They are produced by molecular beam epitaxy (MBE), which can deposit high purity materials with monolayer precision. A typical 2DEG heterostructure is shown in Figure 2.2. These are sometimes called ‘high electron mobility transistor’ (HEMT) heterostructures.

The mobility of an electron gas is a measure of the drift velocity of the electrons in response to an applied electric field. Normally the mobility in semiconductors is limited by scattering with dopants. However, in a HEMT device the dopants and the carriers are physically separated by a spacer layer, leading to a decrease in scattering and an increased mobility. Typical mobilities in HEMT devices are  $\sim 10^6 \text{ cm}^2\text{V}^{-1}\text{s}^{-1}$ .

As can be seen in Figure 2.2, the 2DEG in a HEMT heterostructure resides a significant distance below the surface (approximately 90 nm in this case). To make an electrical (and preferably ohmic) contact to it, a conducting channel must be formed down through the material. This can be achieved by annealing certain

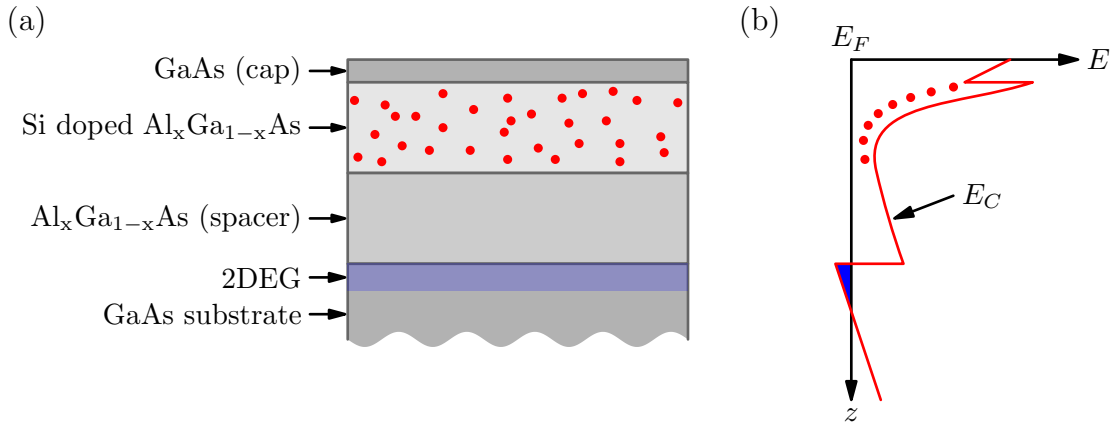


**Figure 2.2:** A standard HEMT heterostructure is shown in (a), and the corresponding conduction band edge profile is shown in (b). The red dots depict the randomly positioned Si dopants. Typically the spacer and dopant layers are 40 nm thick and the capping layer is 10 nm thick. A typical value for the Al fraction in the AlGaAs layers is  $x = 0.33$ .

materials into the heterostructure that provide extra localised doping. A common choice is to pattern AuGeNi on the surface of the material, which on annealing diffuses downwards to form conducting paths that contact the 2DEG.

### 2.1.2 Confinement with surface gates

In addition to their inherent behaviour, semiconductor 2DEGs are also the foundation for a many of studies of mesoscopic 2D effects and lower dimensional electron gases. This work has been facilitated by the rapid development of semiconductor processing technology that allows sub- $\mu\text{m}$  scale patterning on the surface of devices.

By varying the voltage applied to a gate electrode on the surface of a heterostructure, the carrier density in the 2DEG beneath the gate is changed. If a sufficiently negative voltage is applied, the electron gas beneath the gate can be completely depopulated (the conduction band is pushed back above the Fermi energy). This depopulation can be used as a way to create lateral confinement of the 2D carriers. Lateral confinement can also be achieved by etching the heterostructure in certain places, leaving the 2DEG intact in only the unetched regions. These techniques are illustrated in Figure 2.3.

With the ability to laterally confine the 2D carriers on sub- $\mu\text{m}$  length scales came the possibility to observe mesoscopic effects in 2DEGs, for example the ballistic motion of carriers [12, 13, 14] or single-particle interference [15, 16]. It also became

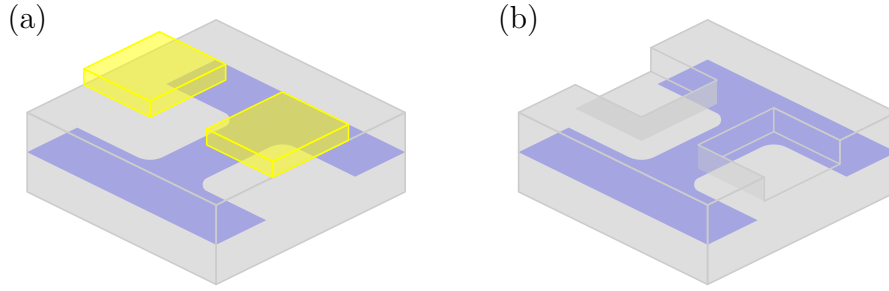


**Figure 2.3:** Lateral confinement in a 2DEG using surface gate electrodes (a), and etching (b). The extent of the 2DEG is shown by the blue layer. In (a) the 2DEG is depleted below the gates when a sufficiently negative voltage is applied to them. In (b) the 2DEG is removed from below the etched pits when they are deep enough to have a significant effect on the band structure. Etching away the doped layer from the heterostructure will ensure that this happens.

possible to produce sufficiently strong lateral confinement to form lower dimensional electron gases. Some of the earliest demonstrations of this were the formation of a conducting channel less than  $1\ \mu\text{m}$  in width confined by two closely spaced surface gates [17, 18]. The conductance of the constriction was found to be quantised in units of  $2e^2/h$ , which is now known to be the case for ballistic transport through a 1D electron gas. Subsequently, strong confinement in all directions was also demonstrated using both surface gates [19, 20, 21] and etched pillar structures [22]. These systems, in which a small puddle of electrons are completely confined, are known as ‘quantum dots’.

Early investigations of transport through quantum dots did not immediately show any direct evidence for the formation of a 0D electron gas. This is because the behaviour of dots is primarily governed by a purely classical effect known as ‘Coulomb blockade’ (this is explained in detail in Section 2.2.1). However, non-linear transport measurements soon revealed the zero-dimensional nature of the states in the confinement potential [23, 24, 25].

The study of quantum dots has expanded to become an immensely productive field of solid state physics. Gated semiconductor dots in particular provide highly tunable, few-particle, quantum mechanical systems. They have attracted attention both for their versatility for studying fundamental physics, as well as being promising candidates for implementing several solid state quantum computation architectures. For reviews of progress in the field, see [26, 27, 28, 29, 30].

## 2.2 Quantum dots

This section outlines the effects that dominate the behaviour of quantum dots, as observed in transport measurements. We mostly restrict discussion to the regime of weak tunnel coupling between a dot and any nearby conductors, as this is most relevant to the scope of this thesis.

### 2.2.1 Coulomb blockade

When an isolated island of charges has a sufficiently small capacitance, the energy required to change its charge by even one electron may be large. Until this energy is somehow supplied, no charge may move onto or off the island and it is said to be ‘Coulomb blocked’. Any current through the island will be suppressed. This phenomenon was first observed in the tunnel current through dielectric films in which small conducting impurities were present, and was explained in detail by Shekhter and Kulik [31, 32].

How small must the capacitance be for Coulomb blockade to be observable? For an island with a charge  $Q$  and a total capacitance of  $C$ , its electrostatic energy is given by  $U = Q^2/2C$ . The energy required to add the  $N$ th electron will therefore be:

$$\mu_N = U(N) - U(N-1) = \frac{(Ne)^2}{2C} - \frac{([N-1]e)^2}{2C} = \left(n - \frac{1}{2}\right) \frac{e^2}{C} \quad (2.4)$$

This value is the electrochemical potential of the island. The ‘charging energy’ for the island is defined as the difference in electrochemical potentials for adding two successive charges:

$$E_{CB} = \mu_{N+1} - \mu_N = \frac{e^2}{C} \quad (2.5)$$

Two conditions must be satisfied for Coulomb blockade to be observable. Firstly, the charging energy must be greater than any thermal fluctuations:  $e^2/C \gg k_B T$ , where  $k_B$  is Boltzmann’s constant. For a typical experimental temperature of 100 mK, this implies that the total island capacitance must be much less than 19 fF. Secondly, the charges must be well localised on the island. For an isolation resistance of  $R$ , the charging (or discharging) time of the island is given by  $t = RC$ . If the energy uncertainty associated with this time ( $\hbar/RC$ ) is greater than  $E_{CB}$ , then the number of electrons on the dot will not be well defined. We find that a resistance  $R \gg \hbar/e^2$  ( $R \gg 26 \text{ k}\Omega$ ) is sufficient to ensure that this is not the case.

The typical configuration of a quantum dot is depicted by an equivalent circuit

diagram in Figure 2.4. The total capacitance of the island ( $C_\Sigma$ ) is small enough, and the tunnel barrier resistances ( $R$ ) large enough, that the dot will exhibit Coulomb blockade at its operating temperature. The dot is tunnel coupled to conducting source and drain reservoirs. The inclusion of a capacitively coupled gate electrode allows the potential of the dot to be controlled. To understand how, we consider the electrostatics of the system in Figure 2.4. The voltage of the dot ( $V$ ) is given by:

$$V = \frac{Q + C_S V_S + C_D V_D + C_g V_g}{C_\Sigma} \quad (2.6)$$

The electrostatic energy for an island with a charge of  $-Ne$  is found by integrating the voltage:

$$U(N) = \int_0^{-Ne} V(Q) dQ = \frac{(Ne)^2}{2C_\Sigma} - Ne \frac{C_S V_S + C_D V_D + C_g V_g}{C_\Sigma} \quad (2.7)$$

The electrochemical potential of the dot [ $\mu_N = U(N) - U(N-1)$ ] is then found to be:

$$\mu_N = \left(N - \frac{1}{2}\right) \frac{e^2}{C_\Sigma} - (C_S V_S + C_D V_D + C_g V_g) \frac{e}{C_\Sigma} \quad (2.8)$$

For certain sets of voltages it is possible to make  $\mu_N$  lie between the potentials of the source and drain reservoirs (assuming that  $V_S \neq V_D$ ). In this situation the Coulomb blockade has been lifted and current may flow between the source and drain, as the charge state of the dot alternates between  $N$  and  $N-1$ . The presence of the gate electrode allows this to be achieved regardless of the values of  $V_S$ ,  $V_D$  and  $N$ .

For quantum dots defined in a semiconductor 2DEG the situation is slightly different to the description above. Instead of the dot being a fixed size island, gated semiconductor dots maintain a roughly constant charge density with their size being dependent on their occupation number ( $N$ ). However, the resulting behaviour is essentially the same.

### 2.2.2 Quantum confinement

In many material systems it is possible to create quantum dots with dimensions comparable to the wavelength of electrons in the dot. In this case, the presence of quantised states in the confinement potential can be observed. Such quantum dots are sometimes called ‘artificial atoms’ because they exhibit phenomena also seen for states in the potential well of an atomic nucleus, such as magic numbers, shells,

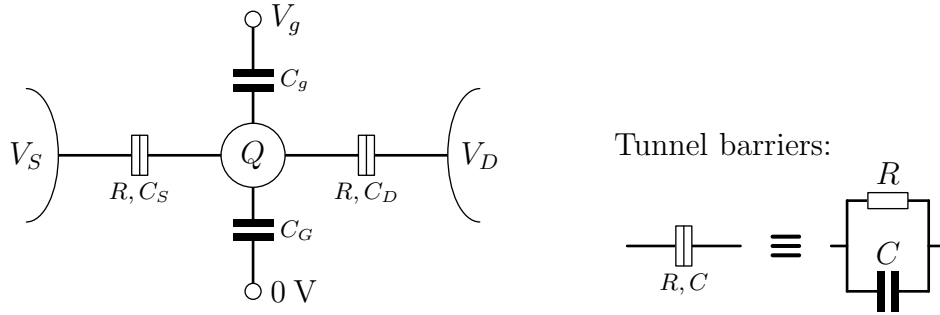


**Figure 2.4:** Equivalent circuit for a typical quantum dot. The dot has a charge  $Q$ , and is connected by two tunnel barriers to source and drain reservoirs, which are at voltages of  $V_S$  and  $V_D$  respectively. The electrochemical potential of the dot can be controlled by the voltage of a capacitively coupled gate electrode ( $V_g$ ). The charging energy is determined by the total capacitance:  $C_\Sigma = C_S + C_D + C_g + C_G$ .

and filling rules [33].

The energy of an artificial-atom-like dot with an occupation number  $N$  is determined by the energies of single-particle states in the confinement potential and the interaction energy between the electrons. At high magnetic fields and low electron densities the details of the interaction are significant [34], but otherwise it is usual to approximate the interaction energy as being constant. This assumption is called the *constant interaction model*. The interaction energy is synonymous with the charging energy of the dot from the purely classical description of Coulomb blockade given in the previous section. The electrochemical potential of the dot in this situation is modified to be:

$$\mu_N = \Delta E_N + \left(N - \frac{1}{2}\right) \frac{e^2}{C_\Sigma} - (C_S V_S + C_D V_D + C_g V_g) \frac{e}{C_\Sigma} \quad (2.9)$$

The new term,  $\Delta E_N$ , is the spacing between the  $N$ th and the  $(N - 1)$ th single-particle states for the specific confinement potential of the dot.

In general it is not possible to determine precisely the shape of the potential well in a gate defined quantum dot. The 2D harmonic potential is a commonly used approximation for etched-pillar quantum dots, and results in single-particle states that lie in equally spaced shells. The  $n$ th shell has a degeneracy (including spin) of  $2(n + 1)$  (with  $n \geq 0$ ). Applying an out-of-plane magnetic field lifts both the orbital and spin degeneracy, leading to the well known Darwin-Fock spectrum. The orbital degeneracy can also be lifted if the potential is not circularly symmetric [34].

For gate defined dots it is usual to assume that the confinement potential will not have a particular symmetry. This implies that the spectrum of single-particle states will be a series of spin-degenerate levels, but that the exact level spacings are hard to predict. (This is further complicated by the fact that it is not always possible to determine the dot's occupancy.) Values of  $\Delta E_N$  can be found experimentally by observing variations in the addition energy ( $\mu_{N+1} - \mu_N$ ) [33]. The spacing of states can also be seen in non-linear transport measurements.

### 2.2.3 First order transport

The transport of electrons through a quantum dot device can be largely understood by considering sequential tunnelling across the two tunnel barriers, where the duration of tunnelling events is far shorter than the time between them. A theory of linear transport ( $V_{SD} = V_S - V_D = 0$ ) in this situation was given by Beenakker [35], and for non-linear transport ( $V_{SD} \neq 0$ ) by Averin, Korotkov and Likharev [36, 37].

The energy levels for a quantum dot in the linear regime are depicted in Figure 2.5. If the electrochemical potential for adding a the  $N$ th charge is close to the potentials of the reservoirs, then the dot's charge state can fluctuate between  $N$  and  $N - 1$  and charge can be transported between the source and drain by the application of a small bias. The dot's conductance ( $G = dI/dV_{SD}$ ) is therefore non-zero. If  $\mu_N$  is far from the reservoir potentials, the dot is Coulomb blocked and has zero conductance. We can move between the two situations by changing the value of  $\mu_N$  with a gate electrode.

The periodic peaks in the conductance of a quantum dot are commonly referred to as 'Coulomb blockade peaks'. They are separated by a gate voltage that corresponds to a change in  $\mu_N$  of the charging energy plus the energy spacing of the lowest available single-particle state. The line-shapes of the peaks depend on the relative values of the temperature of the reservoirs ( $k_B T$ ), the total tunnel coupling ( $\hbar\Gamma_{TOT}$ , where  $\Gamma_{TOT}$  is the sum of the tunnel rates of the two barriers), and the spacing of single-particle states ( $\Delta E$ ). The functional forms of the peak shapes for first-order transport are given by Beenakker [35]. The width of the peaks is determined by the thermal broadening of the source and drain ( $k_B T$ ) if  $k_B T \gg \Delta E, \hbar\Gamma_{TOT}$  or if  $\hbar\Gamma_{TOT} \ll k_B T \ll \Delta E$ . For strong coupling between the dot and the reservoirs (large  $\Gamma_{TOT}$ ), the single-particle states are broadened by energy uncertainty due to their short lifetimes. When  $k_B T \ll \hbar\Gamma_{TOT} \ll \Delta E$ , the width of the peaks is determined by  $\hbar\Gamma_{TOT}$  and their line-shape has a different

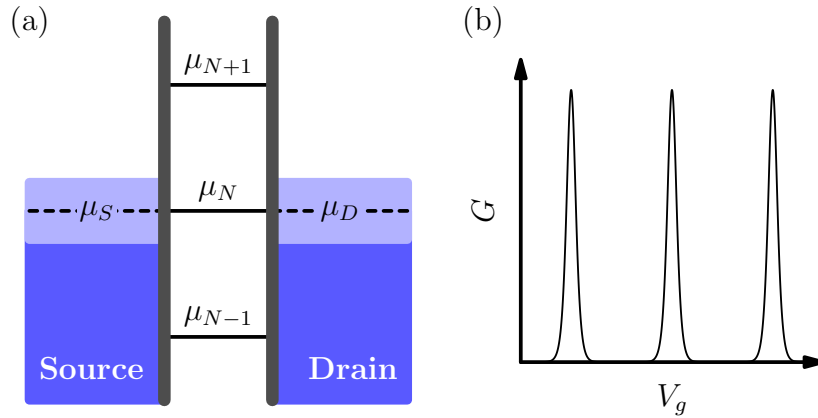


**Figure 2.5:** (a) Energy level diagram for a typical quantum dot in the linear transport regime. The blue shaded regions represent filled states in the source and drain reservoirs. The states are filled up to their chemical potentials ( $\mu_S$  and  $\mu_D$ ). The thermal broadening of reservoirs is indicated by the light blue shaded regions around their potentials. The conductance of the dot is non-zero only when its electrochemical potential lies close to the potentials of the reservoirs. (b) Conductance of the dot as a function of the gate electrode voltage  $V_g$ , which linearly shifts the ladder of dot states.

functional form to the thermally broadened cases.

For biases larger than the blockade peak widths, the dot can no longer be characterised by a linear conductance. This is the non-linear transport regime. With increasing  $V_{SD}$ , a window of energies is opened over which states in the source are full and states in the drain are empty. If the potential of the dot lies within this ‘bias window’, electrons will flow from the source to the drain.

If the bias exceeds the spacing of single-particle states in the dot, it is possible for higher energy states to participate in transport. In this case, it is necessary to extend the notation for the electrochemical potential of the dot: we define  $\mu_{N:i,j} = U_i(N) - U_j(N-1)$ , where  $U_i(N)$  is the energy of the dot holding  $N$  electrons with the last electron in the  $i$ th excited state. For example, the previous definition of  $\mu_N$  is equivalent to  $\mu_{N:0,0}$ . (The electrochemical potential for adding an electron to the  $N$  electron ground state, with the dot starting in the  $N-1$  electron ground state.) If the bias is larger than the energy difference to the first  $N$  electron excited state, then  $\mu_{N:1,0}$  may also lie within the bias window. Transport can then involve this excited state. Similarly, the first  $N-1$  electron excited state may be involved if  $\mu_{N:0,1}$  is available. Figure 2.6 shows the energy levels for a dot in the non-linear regime with single-particle spacings smaller than the bias.

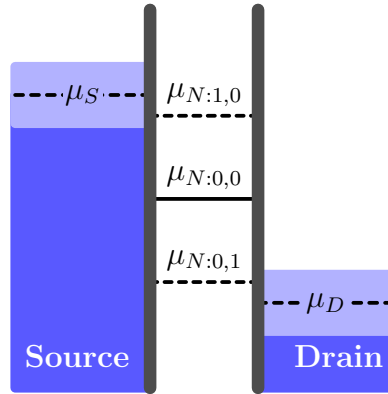


**Figure 2.6:** Energy level diagram for a quantum dot, with well separated single-particle states, in the non-linear transport regime. The electrochemical potentials for two transitions involving excited states are shown ( $\mu_{N:1,0}$  and  $\mu_{N:0,1}$ ).

Even with excited states present, transport through the dot can only occur when  $\mu_{N:0,0}$  lies in the bias window. Consider, for example, the situation where  $\mu_S > \mu_D$  and  $\mu_S > \mu_{N:1,0} > \mu_D$ , but  $\mu_{N:0,0} < \mu_D$ . While it is possible for the  $N^{\text{th}}$  electron to enter the dot in either the ground or excited state, only an electron in the excited state is subsequently able to leave (to the drain). Therefore, when a ground state electron eventually enters, the dot will become ‘stuck’ in the  $N$  electron ground state and no further transport may occur. An equivalent argument applies when considering transport through  $\mu_{N:0,1}$ : the dot becomes stuck in the  $N - 1$  electron ground state when  $\mu_{N:0,0} > \mu_S$ .

The total current through the dot is determined by the tunnel rates of all the available processes. If they are all similar, the result is an increase in current every time a new level moves within the bias window. However, if some processes have an especially low tunnel rate, they can actually reduce the current when they become available. In a conductance measurement this appears as a negative value. The effect is sometimes referred to as ‘negative differential resistance’ (NDR).

The expected characteristics of the dot current as a function of the bias ( $V_{SD}$ ) and the gate electrode voltage ( $V_g$ ) are shown in Figure 2.7. The figure shows the widening of a single Coulomb blockade peak with bias. With a large enough bias, the widened peaks from adjacent charge states overlap leaving diamond shaped regions of zero current between them. These are commonly referred to as ‘Coulomb diamonds’.

The boundaries of the the Coulomb diamonds are labelled as ‘source resonance’

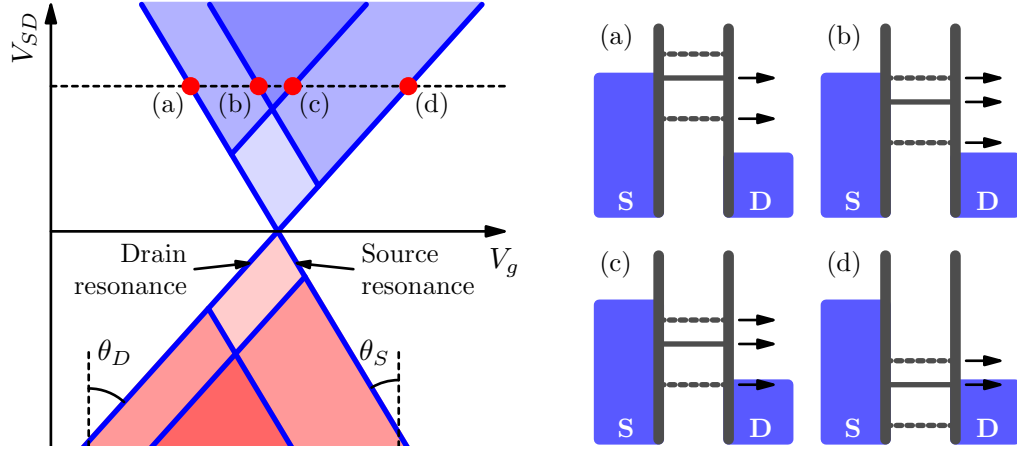


**Figure 2.7:** Features of non-linear transport through a quantum dot with a biased drain. Darker filled blue (red) regions, in the axes on the left, indicate regions of greater positive (negative) current from drain to source. The blue lines show non-zero differential conductance. The angles  $\theta_S$  and  $\theta_D$  are used to determine the conversion factor between  $V_G$  and dot energy. Insets (a)-(c) show the energy levels of the dot at the corresponding points on the axes.

and ‘drain resonance’ in Figure 2.7. This is because they correspond to, respectively, the dot level  $\mu_{N:0,0}$  being aligned with the source and drain potentials. The gradient of these resonances can be used to calibrate the conversion factor (often called ‘lever-arm’), between  $\Delta V_g$  and the change in dot energy. Following the argument of Fühner [38], the gradients are defined as:

$$m_S = \tan(\theta_S) = \left( \frac{\Delta V_g}{\Delta V_{SD}} \right)^{(S)} \quad (2.10)$$

$$m_D = \tan(\theta_D) = \left( \frac{\Delta V_g}{\Delta V_{SD}} \right)^{(D)} \quad (2.11)$$

The superscript in the right hand expression denotes whether the gradient is of the source or drain resonance line. The values of  $m_S$  and  $m_D$  determine the gate electrode lever-arm ( $\alpha_G$ ), which is the conversion factor between changes in  $V_g$  and the electrochemical potential of the dot:

$$\alpha_G = \frac{1}{m_D - m_S} \quad (2.12)$$

The lever-arm for the gating effect on the dot energy from the biased reservoir (in

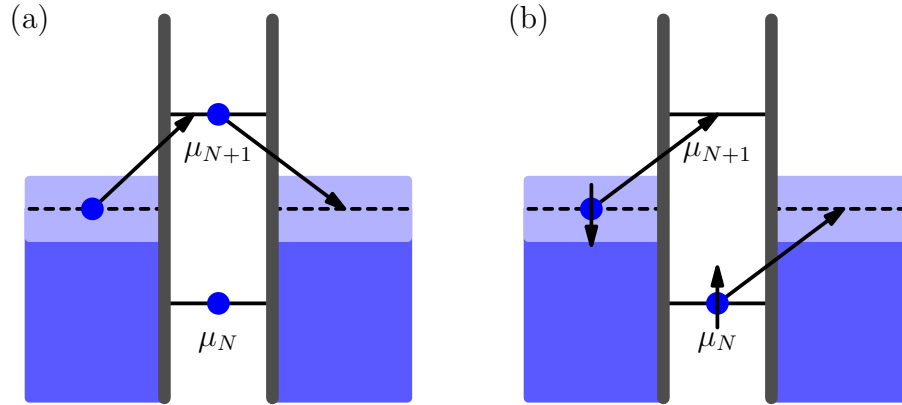


**Figure 2.8:** Energy level diagrams for elastic co-tunnelling (a), and the Kondo effect (b).

this example, the drain) can also be found:

$$\alpha_D = \frac{1}{1 - (m_D/m_S)} \quad (2.13)$$

With the bias applied to only the drain reservoir,  $\alpha_S$  cannot be found.

The extra structure inside the bias window reveals the presence of single-particle states in the dot. Those involving  $N$  electron excited states are commonly referred to as ‘electron excited states’. They appear as lines parallel to the biased reservoir resonance for positive bias, and the unbiased reservoir resonance for negative bias. Those involving  $N - 1$  electron excited states are called ‘hole excited states’ and they have the opposite behaviour. The energy spacing between the states is given by the distance between them in the direction of changing  $V_{SD}$ .

## 2.2.4 Higher order transport

So far we have considered dots that are weakly coupled to their reservoirs and tunnelling events that occur one at a time. However, if the coupling is increased, higher order processes involving two or more correlated tunnelling events can become important. Two examples are co-tunnelling and the Kondo effect. Both allow an electron to tunnel through a dot in an energetically unfavourable situation via an intermediate virtual state.

Co-tunnelling can produce non-zero conductance throughout the normally blockaded region of a Coulomb diamond [39, 40, 41]. Transport occurs when the dot temporarily occupies the energetically forbidden  $N + 1$  electron state. This is al-

lowed by uncertainty if a correlated tunnelling event quickly returns it to the  $N$  electron state. The net result is the transfer of an electron between the source and drain. This is illustrated in Figure 2.8(a). Co-tunnelling can be either elastic or inelastic. In elastic co-tunnelling an electron emerges at the same energy at which one entered, and the dot is left in its ground state. In inelastic co-tunnelling an electron leaves with a lower energy, and the dot is left in an excited state. Inelastic co-tunnelling may only occur when an excited state lies within the bias window, and is therefore suppressed at low bias.

The Kondo effect is a second order tunnelling process that involves the flip of an unpaired spin in the dot [shown in Figure 2.8(b)]. An equivalent explanation is that the reservoir electrons screen the dot's spin by continually causing it to flip via an intermediate virtual state. This many-body interaction is usually described within the context of the Anderson impurity model [42], which was developed to explain Kondo scattering processes in metals with magnetic impurities. The Kondo effect was first observed experimentally in quantum dots in 1998 [43, 44, 45], and since then has attracted continued interest as a controllable system in which many-body physics can be studied.

The typical signature of the Kondo effect in transport through a dot is a finite conductance between blockade peaks that is suppressed by the application of a small bias. Kondo mediated transport can only occur via a singly occupied, spin degenerate energy level, and so only between certain pairs of blockade peaks. The strength of the process is characterised by the 'Kondo temperature', above which it is suppressed.

### 2.2.5 Dots as thermometers

If the lifetime broadening of a state in a dot is significantly less than  $k_B T$ , then transport through the dot will be sensitive to the electron temperature of its reservoirs. This is often used as a method of thermometry, usually by observing the width or height of Coulomb blockade peaks in the linear transport measurement. Both the width and height are sensitive to temperature in different regimes [21, 35, 46].

It is also possible to extract the temperatures of the reservoirs in a non-linear measurement, provided that the dot has a large single-particle state spacing compared to  $k_B T$ . In this situation, the change in current at the edge of a Coulomb diamond is directly determined by the changing density of occupied states in the

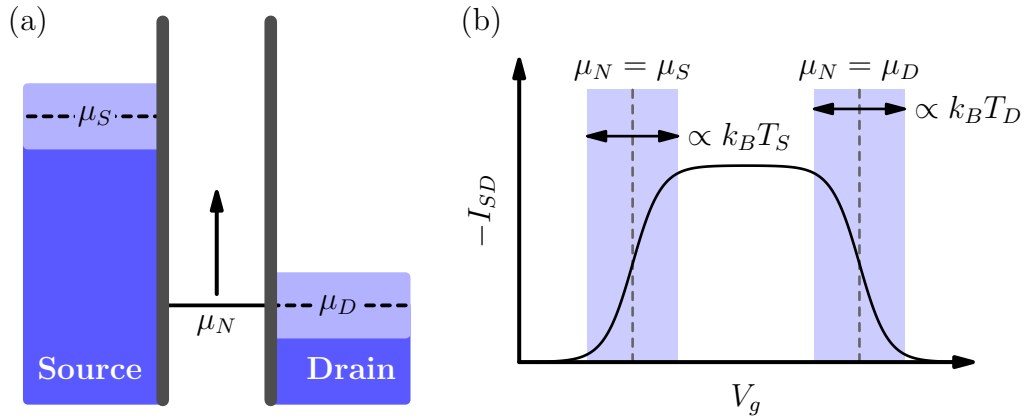


**Figure 2.9:** The effect of a finite reservoir temperature on non-linear transport through a weakly coupled dot. The energy level diagram is shown in (a), and the corresponding current as a function of electrode voltage ( $V_g$ ) is shown in (b). As  $V_g$  is made more negative,  $\mu_N$  increases. Current begins to flow when  $\mu_N$  passes the potential of the drain and stops when it passes the source. These two transitions are given by Fermi functions ( $f(x) = [1 + \exp(x/w)]^{-1}$ ) with widths ( $w$ ) proportional to the appropriate reservoir's temperature.

reservoir [36, 37], which, in turn, is given by a thermally broadened Fermi function. Figure 2.9 shows how a non-linear transport measurement can be used to determine the temperature of the two reservoirs independently.

## 2.2.6 Point-contact detectors

One of the most significant experimental advances in gated semiconductor quantum dot measurements was the realisation of the ‘point-contact detector’ [47]. This tool allows the experimenter to measure changes in the charge state of a dot without making any direct electrical connection to it. The principle of the point-contact detector (also called ‘quantum point-contact’ or QPC detector) is to use the highly non-linear conductance characteristics of a 1D wire (the point-contact) placed in close proximity to the dot as a sensitive probe of the local electrostatic environment. A change of the dot’s average charge by less than a single electron can alter the electrostatic potential of the 1D channel significantly enough to produce a measurable change in its conductance.

Detectors have proved an invaluable tool for probing the behaviour of very weakly coupled quantum dots for which the transport signal is too small to measure. This is often the case when approaching the few- or single-electron regime, as

depopulating a dot this far usually results in very opaque tunnel barriers. In particular, the study of spin effects in few-electron dots has benefited greatly from this technique [30].

If the bandwidth of the point-contact conductance measurement is less than the tunnel rates of the dot barriers, the detector signal reflects the average charge state. However, if the bandwidth is increased it becomes possible to detect individual tunnelling events in real time [48, 49]. This makes it possible to measure the full counting statistics of a system, which provide more information than normal current or noise measurements [50]. It is also possible to measure sub-atto-ampere currents by counting individual electrons passing through a device one at a time [51].

## 2.3 Inelastic scattering of 2D electrons

The low temperature mobility of semiconductor electron gases is limited by elastic scattering from impurities. However, more important to the work presented in this thesis is inelastic scattering, which is necessary for a 2DEG to be able to exchange energy with its environment and to achieve thermal equilibrium. In this section we briefly outline the expected behaviour of various inelastic scattering mechanisms.

### 2.3.1 Electron-electron scattering

In low temperature 2D electron gases with finite disorder, electron-electron scattering is found to be dominated by two processes. The first is due to the fluctuating background potential produced by the movement of all the electrons in the 2DEG, which is experienced by every electron [52]. This is known as Nyquist scattering and it transfers only small amounts of energy between pairs of electrons, compared to the temperature or their excess energy. The scattering rate is linearly dependent on temperature. The second scattering mechanism transfers energies comparable with the temperature or the scatterers' excess energy [53, 54, 55]. For this process, the lifetime for an electron with an excess energy  $\varepsilon$  above the Fermi energy ( $\varepsilon_F$ ) of

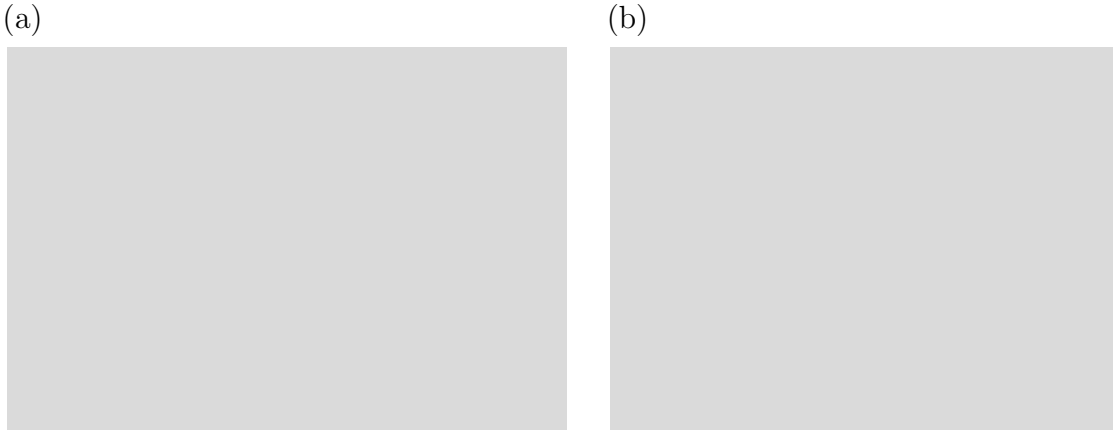


**Figure 2.10:** (a) Electron-electron scattering induced peak broadening in a tunnelling spectroscopy measurement [59]. The calculated broadening is from the theory in [53], from where the plot is reproduced. The ‘GQ’ prediction is from an earlier theory [55]. (b) Measured electron energy loss rate as a function of temperature, reproduced from [61]. The ‘B = 0’ data shows a  $T^5$  dependence, as expected for electron-phonon coupling, with a prefactor similar to the value predicted by equation 2.17, which is  $88 \text{ eVs}^{-1}\text{K}^{-5}$ . The  $T^2$  dependence comes from a different mechanism in the experiment.

a 2DEG at a temperature  $T$  is given by [53];

$$\tau_{e-e}^{-1}(T) = -\frac{\pi\varepsilon_F}{8\hbar} \left(\frac{k_B T}{\varepsilon_F}\right)^2 \ln\left(\frac{k_B T}{\varepsilon_F}\right) \quad [\text{for } \varepsilon_F \gg k_B T \gg \varepsilon] \quad (2.14)$$

$$\tau_{e-e}^{-1}(\varepsilon) = -\frac{\varepsilon_F}{8\pi\hbar} \left(\frac{\varepsilon}{\varepsilon_F}\right)^2 \ln\left(\frac{\varepsilon}{\varepsilon_F}\right) \quad [\text{for } \varepsilon_F \gg \varepsilon \gg k_B T] \quad (2.15)$$

Measurements of electron dephasing have explored the behaviour of these scattering mechanisms and broad agreement with theory is found [56, 57, 58]. Quantitative agreement with the predicted large energy transfer scattering rate (i.e. the combination of Equations 2.14 and 2.15, but excluding Nyquist scattering) has also been measured directly by tunnelling spectroscopy [59, 60] [see Figure 2.10(a)].

### 2.3.2 Electron-phonon scattering

The interaction between electrons and phonons in GaAs is mediated by both the deformation-potential interaction and the piezoelectric interaction. In the first, phonons change the relative positions of the crystal atoms so as to change the electrostatic potential experienced by the electrons. In the second, the change

of atomic positions also changes the polarization of the unit cell. (In GaAs, for example, by changing the relative positions of the Ga and As ions.) This produces an electric field, which is also experienced by the electrons. The relative importance of the two interactions depends on temperature, and for a GaAs 2D electron gas it is found that the piezoelectric interaction dominates below approximately 2.5 K [62].

In a crystal with more than one atom per unit cell, the spectrum of phonon states has multiple branches. These are divided into ‘acoustic’ and ‘optical’ branches [63]. For an acoustic phonon the atoms in a unit cell move in phase, while for an optical phonon they vibrate with respect to each other. Acoustic phonons have zero energy at zero wavevector, while optical phonons always have some minimum energy, and a higher energy than acoustic phonons of the same wavevector. In GaAs, the energy of (longitudinal) optical phonons is approximately 30 meV. At the energies and temperatures we are concerned with in this thesis, it is safe to neglect optical phonons entirely [64].

In the temperature range where optical phonons modes are not thermally populated ( $\ll 100$  K), the strength of electron-phonon scattering in a 2D electron gas splits into two regimes: ‘equipartition’ and ‘Bloch-Grüneisen’. In the first,  $k_B T$  is much greater than the energy of phonons with a wavevector of  $2k_F$ . ( $k_F$  is the Fermi wavevector of the electron gas.) There is therefore a thermal population of phonons available over the whole range of electron energies. The thermal occupation of phonons results in an energy of approximately  $k_B T$  per phonon mode, hence the name ‘equipartition’. The energy relaxation rate of 2D electrons in this regime is proportional to  $T$ .

At temperatures below approximately 5 K, phonons modes with a wavevector of  $2k_F$  cease to be populated and we move to the Bloch-Grüneisen regime [65]. Scattering is dominated by spontaneous phonon emission, and becomes dramatically suppressed by the decreasing availability of empty states near the Fermi surface of the electron gas. In this regime, the energy relaxation rate depends on  $T^3$  for the piezoelectric interaction, and  $T^5$  for the deformation-potential [66]. Both interactions are screened when the typical emitted phonon wavelength is greater than the screening radius in the 2DEG. This increases the exponent of both temperature dependences by 2. Since the screening radius is usually larger than the Fermi wavelength, the temperature below which screening is significant is lower than the cross-over to the Bloch-Grüneisen regime. In typical density GaAs 2DEGs, this

temperature is expected to be approximately 4 K [67].

All the experiments that will be presented in this thesis were performed at temperatures less than 0.5 K. We therefore expect electron-phonon scattering to be dominated by a screened piezoelectric interaction with acoustic phonons in the Bloch-Grüneisen regime. In this case, the energy loss rate from a 2D electron gas at a temperature  $T_e$  to phonons at temperature  $T_l$  is predicted to be [62, 66]:

$$\dot{Q}_P = \Sigma A(T_e^5 - T_l^5) \quad (2.16)$$

where  $A$  is the area of the 2DEG, and  $\Sigma$  is a material dependent parameter. Including the effect of phonon spectrum anisotropy in GaAs,  $\Sigma$  is found to be [68, 61]:

$$\Sigma = (43.3n^{-1/2})\text{fW}\mu\text{m}^{-2}\text{K}^{-5} \quad (2.17)$$

where  $n$  is the 2DEG carrier density in units of  $10^{11}\text{ cm}^{-2}$ . Experimental results have shown reasonable agreement with these theoretical predictions [69, 61, 70, 67] [see Figure 2.10(b)].

## 2.4 Hot carriers

In the Bloch-Grüneisen regime, inelastic scattering between the electrons in the 2DEG and the phonons in the host lattice decreases dramatically with falling temperature. Essentially, the electron gas becomes thermally decoupled from the lattice. Thermalisation with the lattice may occur more readily in the largely metallic ohmic contacts, but the cooling of the 2DEG that can occur via this route is severely limited by the contact resistance between the two (see Appendix C, Figure 2.11). The common result is to find that the 2DEG is elevated to a temperature ( $T_e$ ) that exceeds the temperature of the lattice ( $T_l$ ). The elevated 2DEG temperature is referred to as the ‘electron temperature’. Here we discuss successful techniques for reducing electron temperatures and, conversely, experiments that make use of intentionally elevated electron temperatures.

### 2.4.1 Reducing unintentional heating

The task of trying to cool a sample becomes increasingly difficult at lower temperatures. Increasing thermal boundary resistances make it harder to thermalise the

sample and any wires contacting it. The thermal conductivity of a metal-to-metal contact decreases with temperature as  $T^{-1}$ , and for a metal-to-insulator contact, acoustic mismatch between the phonons in the two materials typically leads to a  $T^{-3}$  dependence [71]. None the less, impressively low electron temperatures can be achieved with careful heat sinking and radiation shielding. For example, in the work of Xia et al. [72] liquid Helium-3 was used as an electrically insulating thermal conductor to heat sink a sample containing a 2DEG heterostructure, and all electrical connections to the sample. Thermal contact with the liquid was made via sintered silver posts, which have an extremely large surface area to counteract the large Kapitza resistance. The final stage of cooling was provided by a PrNi<sub>5</sub> nuclear refrigerator, which was also connected to the Helium-3 via sintered silver. Using this arrangement, electron temperatures of 8 mK were achieved in the 2DEG at a lattice temperature of 4 mK.

Low electron temperatures also require effective filtering of electrical noise in the contact wires. This will otherwise cause heating across any resistive part of the device. Some common techniques are: extensive room temperature filtering; low temperature resistive loads or RC filters, which dissipate noise energy to a well heat sunk point; and metal powder filters, which absorb high frequency noise as the wires pass through a resistive epoxy loaded with metal particles. Using some of these techniques, electron temperatures down to 10 mK have been achieved in dilution refrigerators [73, 5]. However, implementing sufficient filtering becomes harder at lower temperatures, where the same dissipated power will cause a greater increase in temperature.

### 2.4.2 Intentional heating

The weak electron-phonon coupling also makes it possible to locally increase the temperature of a 2DEG using a local source of heat. This has been used as a tool to study the thermal conductance and thermopower of various devices, as well as energy relaxation of hot 2D electrons [74, 75, 76, 77, 78, 79, 80, 81, 67, 82].

The usual technique is to pass a current through a long, narrow region of a 2DEG. The balance between Joule heating in the channel and thermal conduction out of its ends results in an increase in  $T_e$  at its middle. A device placed in contact with this part of the channel then has access to a hot 2D reservoir, the temperature of which is controlled by the heating current. By modulating the heating current at a known frequency ( $f$ ), it is also possible to identify purely thermal signals in

the measurement: since Joule heating depends on  $I^2$ , the temperature will be modulated at twice the frequency of the current. Any signals due to the temperature change can be detected by a lock-in measurement at a frequency of  $2f$ .

## 2.5 Low temperature electronic refrigeration

As previously discussed, traditional techniques for cooling 2DEGs are destined to become increasingly difficult for temperatures in the mK regime and below. With lower base temperatures it becomes increasingly hard to heat sink the 2DEG effectively, but it also becomes increasingly difficult to achieve the lower base temperatures in the first instance. Typical dilution refrigerators are limited to a few mK, and to go below this requires the additional use of one or more nuclear demagnetisation refrigeration stages. While this approach has been successfully used to reach extremely low temperatures (less than 1  $\mu$ K [83]), it adds an extra level of significant complexity and does not solve the thermalisation issues.

An attractive solution to the problem is to refrigerate a 2DEG by directly removing energy from its carriers. In doing this, decoupling from the lattice phonons is an advantage, since it makes it easier to cool the electrons below the temperature of their environment. Figure 2.11 illustrates the difference in heat flows between traditional and direct refrigeration. With sufficient direct refrigeration providing the final stage of cooling, the 2DEG could be driven below the base temperature of whatever conventional refrigeration was used to cool the sample's lattice and the measurement wiring.

One well established method for direct electronic cooling is by using the Peltier effect. When a current is passed across the boundary of two materials with different Peltier coefficients ( $\Pi$ ), heat will be deposited or removed at the junction, depending on the direction of the current. In a typical Peltier refrigerator a cooled bath is connected to two leads made of materials with opposite signs of  $\Pi$  (such as  $n$  and  $p$  type semiconductors). A current flowing from one lead to the other, via the bath, will then either cool or heat both junctions. Unfortunately the efficiency of Peltier cooling decreases drastically with temperature (the maximum temperature reduction is  $\propto T^2$  [84]). To date the technique has been demonstrated only down to temperatures of  $\sim 4$  K. (A temperature reduction of 0.17 K at 3.5 K has been reported by Harutyunyan et al. [85].) While this may be improved in the future by using exotic materials with larger thermoelectric coefficients, conventional Peltier

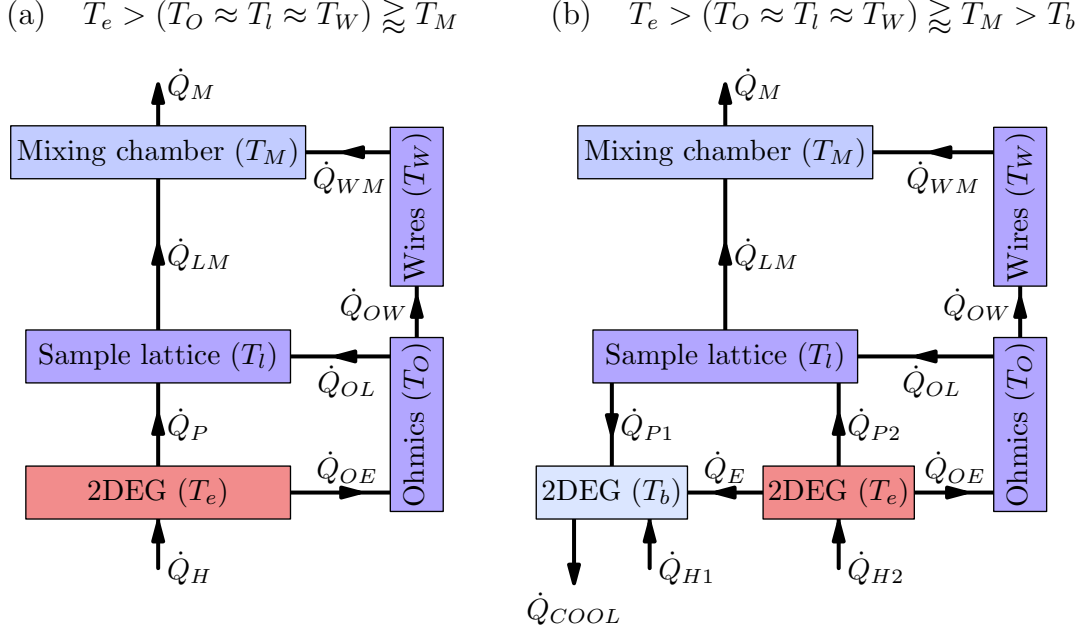


**Figure 2.11:** Heat flows for cooling a 2DEG in the normal way [in (a)] and by direct cooling [in (b)]. For the normal case, the only heat flow out of the system is through the mixing chamber ( $\dot{Q}_M$ ). Any parasitic heating of the 2DEG ( $\dot{Q}_H$ ) is removed via electron-phonon coupling with the lattice ( $\dot{Q}_P$ ) or electrical connection with the ohmic contacts ( $\dot{Q}_{OE}$ ). The temperature of the 2DEG ( $T_e$ ) is elevated because of the high thermal resistances of these two paths. The ohmic contacts are cooled by their coupling to the lattice and the measurement wires ( $\dot{Q}_{OL}$  and  $\dot{Q}_{OW}$ ), both of which are in turn cooled by heat-sinking to the mixing chamber ( $\dot{Q}_{LM}$  and  $\dot{Q}_{WM}$ ). It is usual to assume that the heat-sinking is good, so  $T_l \approx T_W \approx T_M$ . We also assume that  $T_O \approx T_l$ , which is reasonable for a typical sample (see Appendix C).

In (b), a 2DEG region is cooled directly by some mechanism ( $\dot{Q}_{COOL}$ ). Parasitic heating ( $\dot{Q}_{H1}$ ), phonon heating ( $\dot{Q}_{P1}$ ), and heating from electrical connections to other 2DEG regions ( $\dot{Q}_E$ ) are all balanced by  $\dot{Q}_{COOL}$ . Cooling from the mixing chamber is required to maintain a low  $T_l$  and  $T_e$  in order to minimise  $\dot{Q}_{P1}$  and  $\dot{Q}_E$ . At ever lower temperatures, increasing thermal resistances to the cooled 2DEG now reduce its *heating*, whereas in the normal case they reduced *cooling*.

cooling is currently not a viable mechanism for providing direct refrigeration of a 2DEG at mK temperatures.

Another potential technique for directly cooling a 2DEG is by thermionic emission. In this scheme hot electrons are selectively removed from one electrode by being pulled over (or through) a potential barrier, by an electric field, to a second electrode. The barrier can either be in a material between the two electrodes [86, 87] or be a vacuum gap in between them [88]. For the former case, cooling has been demonstrated in semiconductor structures [89, 90, 91], but only at room temperature or warmer. Cooling by emission across a vacuum gap has also only been demonstrated at room temperature [92]. It may be possible to reduce the operating temperature of vacuum gap devices by incorporating resonant tunnelling through a quantum well into the emission process [93], but even this approach is limited to  $\sim 10$  K. So, as with the Peltier coolers, thermionic emission devices cannot currently operate at low enough temperatures to be used for cooling a 2DEG.

Recent experiments have demonstrated cooling using superconducting flux qubit devices; by microwave pumping of a three-level system [94], and by ‘Sisyphus cooling’ of a coupled tank circuit [95]. Impressively, the former work showed cooling of a superconducting flux-qubit to approximately 3 mK at a 400 mK ambient temperature. Unfortunately, while this is the appropriate temperature regime, these techniques could not be applied to directly cool a 2DEG since they both operate on systems with well separated energy levels.

The only experimentally realised technique for directly cooling an electron gas in the mK regime is the ‘superconducting refrigerator’ (for a review, see [96]). In the following section we discuss previous work with these devices and their applicability for direct cooling of a 2DEG. We then review a theoretical proposal that is conceptually similar, but utilises quantum dots instead of superconductors. This ‘quantum dot refrigerator’ is a closely related, but more attractive, approach to direct 2DEG cooling.

### 2.5.1 Superconducting coolers

The basic principle behind the operation of superconducting coolers is the energy-dependent tunnelling of electrons between a superconductor and a normal metal (see Figure 2.12). This arises because the density of states of quasiparticles in a superconductor possesses a gap, corresponding to the binding energy of a single Cooper pair. An electron cannot tunnel from the normal metal without having

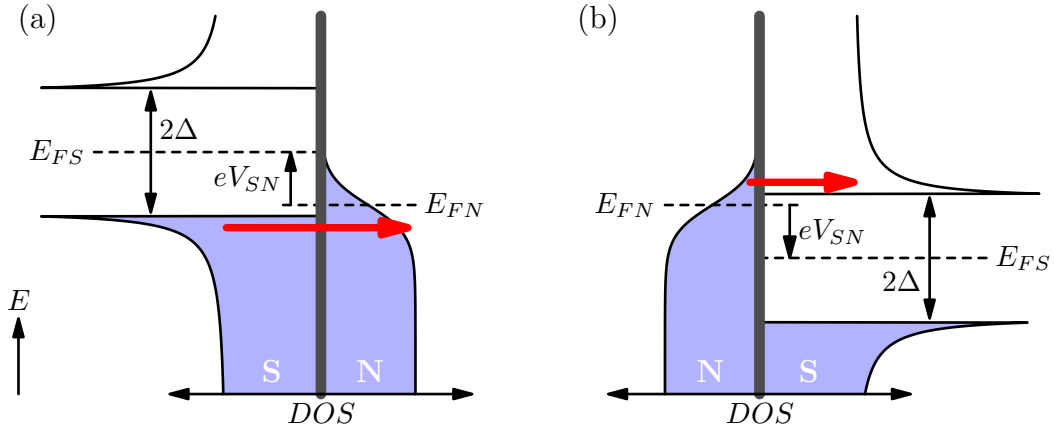


**Figure 2.12:** Density-of-states vs. energy at a normal-metal-superconductor tunnel junction, with opposite bias voltages ( $V_{SN}$ ) shown in (a) and (b). Filled states are shown in blue. Tunnelling occurs when there are empty states on one side of the barrier and full states on the other. The red arrows indicate the small energy range over which this is the case in the two situations. In (a) electrons are only injected into the normal metal below  $E_{FN}$  (its Fermi energy), and in (b) electrons are removed from the normal metal above  $E_{FN}$ . As long as the occupation of states in the normal metal can relax quickly back to a Fermi function (by electron-electron scattering), the net result of tunnelling in both cases will be a slight lowering of its temperature.

enough energy to break a Cooper pair, and so the tunnelling process is energy-dependent. Furthermore, by biasing the junction, the cut-off energy relative to the Fermi energy of the normal metal can be changed. The system is often referred to as a ‘SIN’ junction (S = superconductor, I = insulator (the tunnel barrier), and N = normal metal).

By biasing a SIN junction appropriately, as shown in Figure 2.12, the energy-selective tunnelling at the junction can be made to cool the electron gas in the normal metal. A SIN junction can also be used as a thermometer of the normal metal, as the characteristics of  $I$  vs.  $V_{SN}$  are temperature dependent. The first demonstration of a refrigerator of a normal metal based on these techniques used one SIN junction for cooling and another as a thermometer [97]. This work showed cooling of the normal metal electron gas by about 10 mK below a lattice temperature of 100 mK.<sup>1</sup>

Further work on superconducting coolers showed that a superior arrangement

<sup>1</sup>Similar experiments had been done previously, but with a different superconducting material in the place of the normal metal island [98, 99, 100, 101, 102, 103]. These experiments studied the enhancement of superconductivity in the island that could be achieved by the energy-selective removal of normal carriers from above the gap.

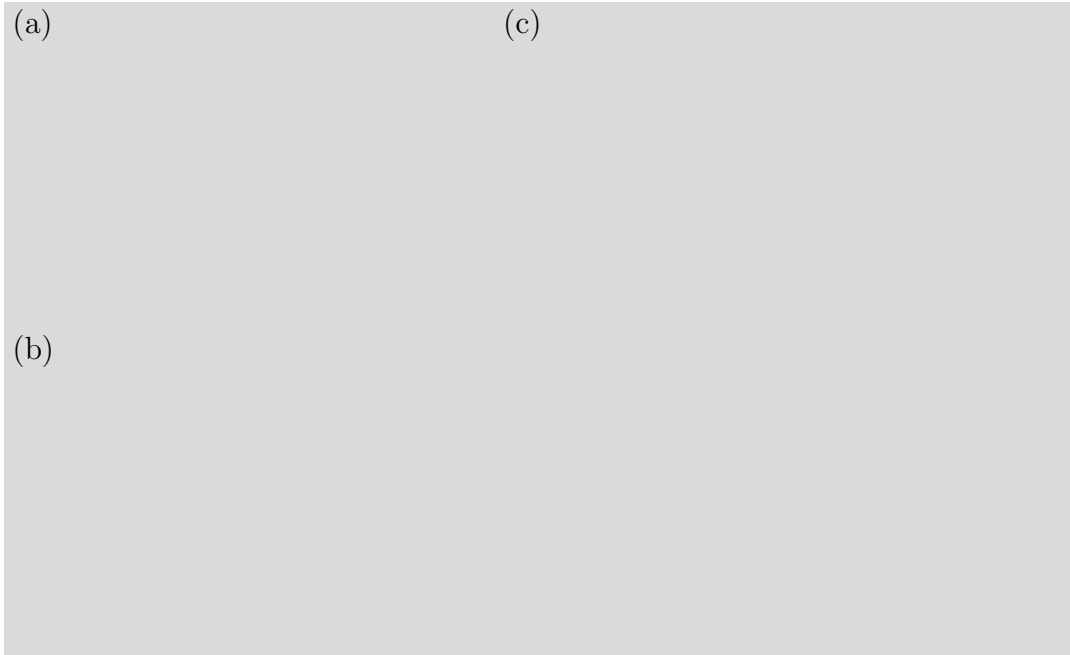


**Figure 2.13:** Details of a SINIS cooler from [104]. (a) shows the experimental setup, with the NIS junctions indicated by the four bisected rectangles in the shaded square. The cooling current is driven through two junctions by  $V_{refr}$ . The voltage between the other two junctions with a current bias of  $I_{th}$  is used to measure the temperature of the normal metal island. (b) shows an AFM image of the device, which was fabricated using shadow mask evaporation. The normal metal island is Cu, the superconducting leads are Al, and the tunnel barriers are a native oxide layer. (c) shows the measured island temperature as a function of bias voltage. The two temperature minima are centred at the optimum biases of  $V_{refr} = \pm\Delta/e$ .

was to use two SIN junctions in series to form a SINIS structure, similar to a traditional Peltier cooler [104] (see Figure 2.13). One junction is biased to inject electrons below the Fermi energy of the normal metal, and the other to extract above it (as if the two halves of Figure 2.12 were joined in the middle). Numerous measurements of such devices have shown them able of achieving cooling powers up to 30 pW [105, 106] and temperature reductions up to 200 mK [104] at ambient temperatures around 300 mK.

The base temperature of SINIS coolers is found to be limited by several factors. Firstly, at ambient temperatures below approximately 100 mK the rate of electron-electron scattering in the normal metal is usually found to be small compared to the rate of electron injection and removal [97, 107]. In this case, the electron gas in the normal metal does not have sufficient time to relax between tunnelling events and

the distribution of occupied states is driven from the equilibrium Fermi function. Such non-equilibrium distributions can be observed in the  $I$ - $V$  characteristics of a probe NIS junction [108, 107], but it is not easy to apply a temperature to the electron gas in this situation. Furthermore, the cooling power also becomes significantly reduced. To lower the temperature at which this out-of-equilibrium regime occurs, the cooled area must be made larger, or the tunnel junctions more resistive [2]. Naturally, both changes will lower the performance of the cooler, requiring the device to operate at a lower ambient temperature.

A second factor limiting the performance of SINIS coolers is the presence of states within the superconducting gaps in the leads. These can be caused by the proximity effect from contact with normal metals, or by inelastic scattering in the superconductor. Tunnelling to and from these states leads to parasitic heating of the normal metal. Pekola et al. [107] find that the minimum temperature achievable in a SINIS cooler is given by:  $T_{min} = 2.5T_C\eta^{2/3}$ , where  $T_C$  is the critical temperature of the superconductors and  $\eta$  is the density of extra states in the gaps. They also find an upper limit for  $\eta$  in their device of 0.01.

A third limitation is due to heat deposited in the superconducting electrodes. This directly reduces the cooling power and also heats the cooled island indirectly by the emission of hot phonons [109]. Clark et al. showed how this effect could be reduced by increasing the volume of the superconducting electrodes in the vicinity of the tunnel junctions [110].

As well as cooling normal metal islands affixed to a substrate, superconducting refrigerators have also been used to cool the lattice of various suspended micro-structures [111, 112, 113, 114, 115], a thermally contacted Germanium resistance thermometer [116], and the leads of a superconducting single electron transistor [117]. However, of particular relevance here are experiments where the electron gas in a semiconductor, instead of in a normal metal, is cooled [118, 119, 120]. In these experiments the Schottky barrier between a superconducting electrode and heavily doped silicon forms an ‘SSm’ tunnel junction (Sm = semiconductor). Cooling in ‘SSmS’ devices has been successfully demonstrated, achieving reductions in the semiconductor electron temperature of almost 100 mK from an equilibrium value of 150 mK [120].

The ‘SSmS’ scheme initially seems an ideal candidate to provide direct cooling of a 2DEG; however, the formation of the Schottky barriers presents a significant obstacle. In the experiment of Savin et al., [120], the best refrigerator performance

was found with a carrier concentration in the silicon of  $(4 \cdot 10^{19}) \text{ cm}^{-3}$ , and tunnelling contact-resistances of  $(7 \cdot 10^{-3}) \Omega \text{ cm}^2$ . In contrast, typical 2DEG carrier concentrations are  $\sim (1 \cdot 10^{11}) \text{ cm}^{-2}$ , and since the 2DEG resides some significant distance below the surface of its heterostructure, tunnelling contact resistances are many orders of magnitude larger. It is not clear how a suitable tunnel contact between a superconductor and a 2DEG could be formed, and for this reason it seems unlikely that a superconducting cooler could provide the direct cooling we require. However, much of the physics underlying such devices, and the behaviour they exhibit, is shared with a more promising direct cooling scheme that we discuss below.

### 2.5.2 The quantum dot refrigerator

The ‘quantum dot refrigerator’, or ‘QDR’, was proposed by Edwards et al. [1, 2] as a scheme for cooling a 2DEG. The basic principle of operation is similar to the SINIS coolers discussed above: electrons are injected into and removed from an electron gas through two points of energy-dependent tunnelling. When the injection is made to occur at a lower energy than the removal, the net effect of the resulting current is to continuously pump energy out of the electron gas. In a QDR, the energy-dependent tunnelling is achieved by using quantum dots with well separated single-particle states. The principle of QDR operation is illustrated by the energy level diagram given in Figure 2.14.

The work of Edwards et al. studied the theoretical behaviour and limitations of a QDR and provides some interesting results, which we now summarise. The current ( $I$ ) and energy flow to the cooled 2DEG ( $\dot{Q}_T$ ) were calculated for the system shown in Figure 2.14. The central region was assumed to be at a constant potential ( $\mu_C$ ). The two dots were given a ladder of well separated single particle states, spaced by an energy  $\Delta E$ . Lifetime broadening of the dot states (of width  $\delta$ ) was included in the calculation. The dots were generally given a large state spacing ( $\Delta E \gg k_B T_e$ ) to provide the energy selectivity required for cooling.

A simulation of the QDR was performed to find the lowest temperatures attainable in the central region. This is defined as the ‘base temperature’ ( $T_b$ ). Although trivially it seems as though cooling might continue indefinitely, it was found that off-resonance tunnelling through the wide Lorentzian tails of the dot states results in a heat-leak. At a low enough temperature this negates the cooling effect, leading to  $\dot{Q}_T = 0$  and a minimum attainable value of the central region temperature. The

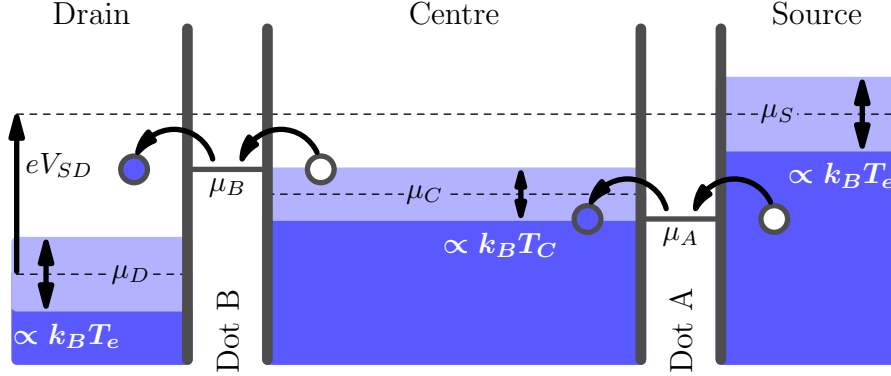


**Figure 2.14:** Energy levels of a QDR operating in the cooling regime. Occupied states in the ‘Source’, ‘Centre’ and ‘Drain’ 2DEGs are shown by the blue shaded areas, and the light blue shading around their respective Fermi energies ( $\mu_S$ ,  $\mu_C$ , and  $\mu_D$ ) indicates their thermal broadening. Dots A and B both have a single-particle state available for transport in the energy range shown, with electrochemical potentials of  $\mu_A$  and  $\mu_B$  respectively. The net transfer of an electron from source to drain removes an energy ( $\mu_B - \mu_A$ ) from the central region.

results of the simulations showed that the temperature reduction ( $T_e/T_b$ ) is maximised by increasing the separation of the dot states and decreasing their lifetime broadening. Cooling is also maximised when  $(\mu_B - \mu_A) \approx k_B T_b$  and  $\delta \lesssim k_B T_b$ .

The results of the simulations were also used to justify the validity of two approximate expressions for  $I$  and  $\dot{Q}_T$ . These were found by assuming that  $(\mu_B - \mu_A) = k_B T_b$ , that each dot has only a single state involved in transport, and that the lifetime broadening of the dot states can be approximated by a step function of width  $\delta$ . This leads to:

$$I = (1.8 \text{ nAK}^{-1}) \cdot T_b \quad (2.18)$$

$$\dot{Q}_T = (0.31 \text{ pWK}^{-2}) \cdot T_b^2 \quad (2.19)$$

These expressions are approximately equal to the results of the full calculation, provided  $T_b$  does not approach its fundamental limit. One significant limitation of the theory presented in [2] is that the peak conductance of the two dots is assumed to be  $2e^2/h$ . In reality this situation is rarely achieved, and would in any case be associated with a large lifetime broadening. The expressions above are therefore upper estimates corresponding to a physically unlikely situation, but are still correct to within a common constant factor.

Having investigated the fundamental limitations of a QDR, Edwards et al. then

included the effects of heat flow due to electron-phonon coupling. This was modelled as  $\dot{Q}_P \propto A(T_l^5 - T_b^5)$  (where  $T_l$  is the lattice temperature), with a constant of proportionality approximately in agreement with that given by Equation 2.17. By solving for the steady thermal state ( $\dot{Q}_T + \dot{Q}_P = 0$ ), the following approximate expression linking the base temperature, ambient temperature, and 2DEG area was found;  $10.3T_b^2 = A(T_l^5 - T_b^5)$ .

So far it has been implicitly assumed that the occupation of states in the central 2DEG is always given by a Fermi function; however, the energy-dependent injection and removal of electrons will try to drive away from this situation. If the injected electrons cannot quickly scatter out of the injection energy window, then the occupation of states will be given by some non-equilibrium distribution with which a temperature cannot be easily associated. The cooling power will also be drastically reduced. The rate of scattering out of the injection energy window is given by the large-energy-transfer electron-electron scattering rate ( $\tau_{e-e}^{-1}$ , given by Equations 2.14 and 2.15), multiplied by the number of states in the central 2DEG that lie within the window ( $N \approx nA\delta$ , where  $n$  is the carrier density,  $A$  is the central 2DEG area, and  $\delta$  is the dot state's lifetime broadening).

Taking into account both the electron-phonon coupling and the electron-electron scattering rates, the expected behaviour of a QDR is split into three regimes:

- *Equilibrium*: the phonon heating overwhelms the QDR cooling, leaving the central 2DEG in equilibrium with the lattice.
- *Quasi-equilibrium*: the QDR cooling successfully overcomes the phonon heating, and the electron-electron scattering is fast compared to the injection rate. The density of occupied states in the centre is therefore given by a Fermi function but at a temperature different from the lattice.
- *Out-of-equilibrium*: The rate of electron-electron scattering is slow, and so the central 2DEG is driven from equilibrium by the cooling current. Equations 2.18 and 2.19 are no longer valid and the cooling power is reduced.

Edwards et al. determined that, in general, a QDR with a larger central 2DEG can be cooled to lower temperatures before entering the out-of-equilibrium regime; however, it must be operated at a lower ambient temperature to minimise phonon heating. Two specific examples that are given are: a  $100 \mu\text{m}^2$  2DEG can be cooled from 200 mK to 120 mK, and a  $1 \text{cm}^2$  2DEG can be cooled from 1 mK to 120  $\mu\text{K}$ . Provided the cooled 2DEG can be made large enough, the dot states made narrow

enough, and the operating temperature low enough, there should be no limit on the base temperature that a QDR can achieve.

# Chapter 3

## Quantum dot refrigerator: experimental realisation

---

This chapter details the design, fabrication and characterisation of a proof-of-concept Quantum Dot Refrigerator (QDR). The device was found to satisfy the known requirements for QDR operation, but also exhibited unexpectedly large electrostatic effects. The significance of this is discussed, and an analysis that takes account of electrostatic coupling in a QDR is subsequently detailed in Chapter 4.

### 3.1 Design

The design of the QDR device was primarily based on the requirement that it functions in the temperature range accessible by a dilution refrigerator: approximately 50 mK to 300 mK. It was also desirable for all regimes of operation to be accessible within this range to allow a full investigation of the device's behaviour.

The final design is shown in Figure 3.1. It shows surface gates for isolating a small area of 2D electron gas, and for forming up to three quantum dots around its perimeter. Only two dots are required for a QDR device. The third was to be used as a thermometer of the isolated region. There are also three gates for defining short 1D channels adjacent to each of the dots. These can serve as sensitive detectors of the charge states of the dots, as discussed in Section 2.2.6. The remainder of this section discusses the considerations behind this design in detail.

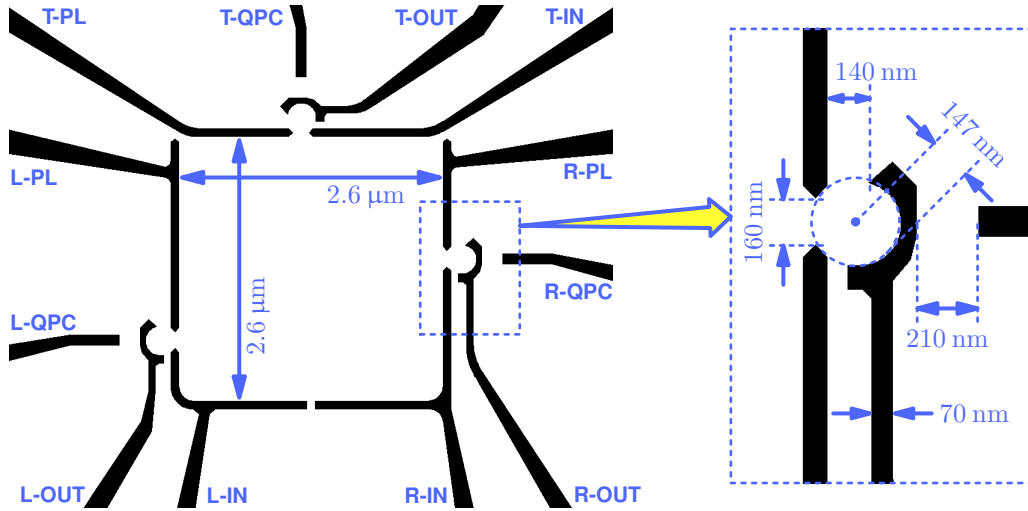


**Figure 3.1:** QDR surface gate design with a central region of  $6.76 \mu\text{m}^2$  area. The actual area of an electron gas in this region, accounting for lateral depletion from the gates, is expected to be less than  $5.8 \mu\text{m}^2$ . All three of the dots around the perimeter have identical proportions.

### 3.1.1 Size of the cooled electron gas

The primary factor in designing a QDR is the size of the cooled electron gas; if it is too large the available cooling power will be less than heating from the phonon bath; if it is too small the distribution of occupied states will be too easily driven from quasi-equilibrium by the cooling current. More fundamentally, the electron gas must also be large enough that its discrete energy level spectrum may be approximated as a continuum.

We consider first the average energy separation between states ( $\Delta E_C$ ). In a 2D electron gas of area  $A$ , this can be found from the density of states:  $g_{2D}(\varepsilon) = (m^*/\pi\hbar^2)$ . Discounting the zero energy separation between spin degenerate states, the average energy separation is given by:

$$\Delta E_C = (2\pi\hbar^2/m^*A) \quad (3.1)$$

For the spectrum of states to be approximately continuous, we require that  $\Delta E_C$  be less than  $k_B T$ . At 50 mK, this implies  $\Delta E_C < 4.3 \mu\text{eV}$ . The isolated electron gas must therefore have an area larger than  $1.7 \mu\text{m}^2$ . Solutions to  $\Delta E_C = k_B T$ , in the range 10 mK to 300 mK, are given as the solid line in Figure 3.2.

A second consideration for the size of the cooled electron gas is the requirement

that the distribution of its occupied states should ideally be in quasi-equilibrium (determined by a Fermi function, but at a non-equilibrium temperature). While it is true that cooling, i.e. energy extraction, still occurs if the distribution of occupied states is driven out of equilibrium, the temperature becomes hard to define. Furthermore, the cooling power is expected to be significantly reduced in this regime [2].

To maintain quasi-equilibrium in the isolated electron gas, the rate at which carriers are injected must be less than the rate at which they scatter out of the states they are injected into. The injection rate is  $I/e$ , where  $I$  is the current through the QDR. The size of the energy range over which carriers are injected into the isolated, central 2DEG is determined by the lifetime broadening of the dot states ( $\approx 4\hbar I/e$ ).<sup>1</sup> The scattering rate out of the energy range is given by the product of the temperature dependent, large energy-transfer scattering rate ( $\tau_{e-e}^{-1}$ , from Equation 2.14 and 2.15), and the number of states available within that range;  $4g_{2D}A\hbar I/e$ . By requiring that

$$(4g_{2D}A\hbar I/e)\tau_{e-e}^{-1} > I/e \Rightarrow 4g_{2D}A\hbar\tau_{e-e}^{-1} > 1 \quad (3.2)$$

we find that the cooled electron gas must have an area greater than  $80 \mu\text{m}^2$  to remain in quasi-equilibrium when cooled to a base temperature of  $T_b = 50 \text{ mK}$ . Similarly, for  $T_b = 150 \text{ mK}$  the area must be greater than  $10 \mu\text{m}^2$ , and for  $T_b = 300 \text{ mK}$  it must only be larger than  $3 \mu\text{m}^2$ . The solutions to  $4g_{2D}A\hbar\tau_{e-e}^{-1} = 1$ , calculated from  $10 \text{ mK}$  to  $300 \text{ mK}$ , are given as the dashed line in Figure 3.2.

The upper bound for the size of the cooled electron gas is determined by comparing the incoming heat from the phonon bath ( $\dot{Q}_P$ ) with the available cooling power of the system due to charge transport ( $\dot{Q}_T$ ). For a fully optimised QDR, cooling to a base temperature of  $T_b$ , the cooling power is given by (see Section 2.5.2):

$$\dot{Q}_T \approx (0.31 \text{ pW K}^{-2}) \cdot T_b^2 \quad (3.3)$$

As discussed in Section 2.3.2, the heat transfer between a 2D electron gas, of area  $A$  and at a temperature  $T_e$ , and lattice phonons, at a temperature  $T_l$ , is given by:

$$\dot{Q}_P = \Sigma A(T_e^5 - T_l^5) \quad (3.4)$$

<sup>1</sup>The current through both dots is  $I \approx e\Gamma_0/2$ , where  $\Gamma_0$  is the tunnel rate of the dot barriers. The lifetime broadening of the states in each dot is  $\hbar\Gamma_{total} = 2\hbar\Gamma_0 = 4\hbar I/e$ .

where  $\Sigma$  is a material parameter. The material chosen for fabricating the devices (wafer *T567*; see Appendix A.1) has a 2D carrier density of  $n = 1.37 \cdot 10^{11} \text{ cm}^{-2}$ , giving  $\Sigma \approx 40 \text{ fW}\mu\text{m}^{-2} \text{ K}^{-5}$  according to Equation 2.17.

For a QDR cooling an isolated electron gas to a base temperature of  $T_b = 50 \text{ mK}$ , Equation 3.3 estimates the available cooling power as  $0.78 \text{ fW}$ . For a lattice temperature of  $T_l = 300 \text{ mK}$ , Equation 3.4 implies that this cooling power can overcome the incoming heat from phonons if the electron gas has an area less than  $8 \mu\text{m}^2$ . Solutions to  $\dot{Q}_T < \dot{Q}_P$ , for lattice temperatures between  $50 \text{ mK}$   $300 \text{ mK}$  and base temperatures from  $10 \text{ mK}$  to  $300 \text{ mK}$ , are indicated by the shaded regions in Figure 3.2.

Motivated by these considerations, but also taking into account that Equation 3.3 is based upon a fully optimised QDR, an area of approximately  $6 \mu\text{m}^2$  was chosen for the cooled electron gas. Such an area should be large enough for the energy spectrum of states to be continuous, and also small enough for the QDR to overcome phonon heating, even if the available cooling power is significantly less than expected.

For a  $6 \mu\text{m}^2$  2DEG, the calculations here predict that the cross-over from the quasi-equilibrium to out-of-equilibrium regimes will occur at  $T_b \approx 200 \text{ mK}$ . This would allow the study of both regimes within the available temperature range, although it would also limit the lowest achievable temperature.

### 3.1.2 Size of the quantum dots

The only constraint on the design of the dots for a QDR is that they have a significant energy separation between their states due to quantum confinement. Specifically, the state separation should be much greater than  $k_B T_e$ , where  $T_e$  is the electron temperature in the reservoirs.

To ensure a large level separation in the dots they were made as small as practically possible. The material chosen for fabrication is a standard  $90 \text{ nm}$  HEMT, meaning that the 2DEG resides  $90 \text{ nm}$  below the surface. As such, no feature smaller than this can be defined in the 2DEG by surface gates. The dots were designed to have a radius of  $150 \text{ nm}$ , and also to have around  $150 \text{ nm}$  wide entrance and exit channels.

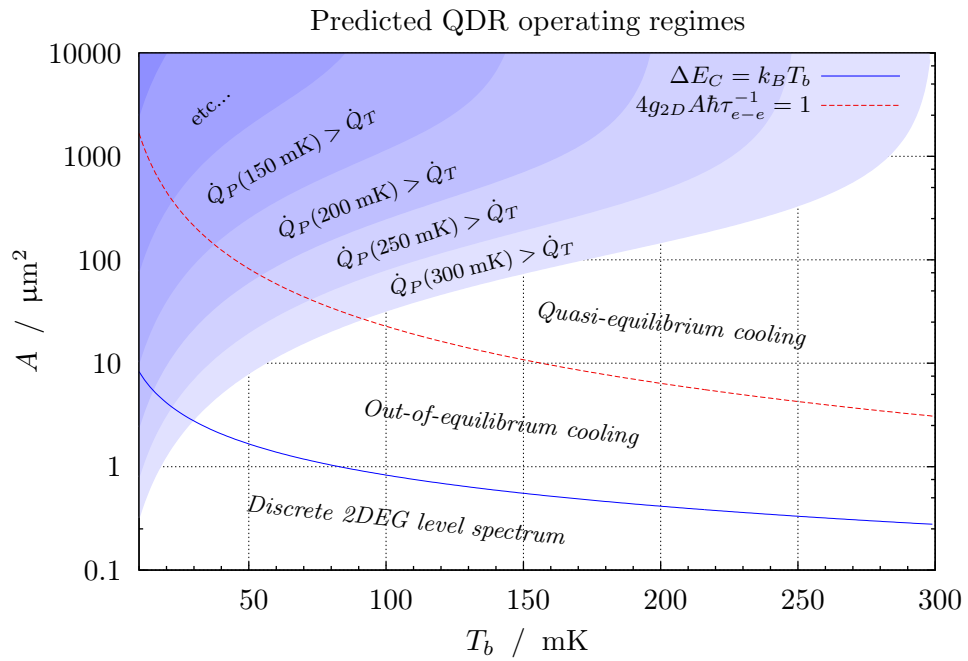


**Figure 3.2:** Expected regimes of QDR operation as a function of the isolated 2DEG temperature ( $T_b$ ) and area ( $A$ ). The functional forms of the curves are detailed in the text.

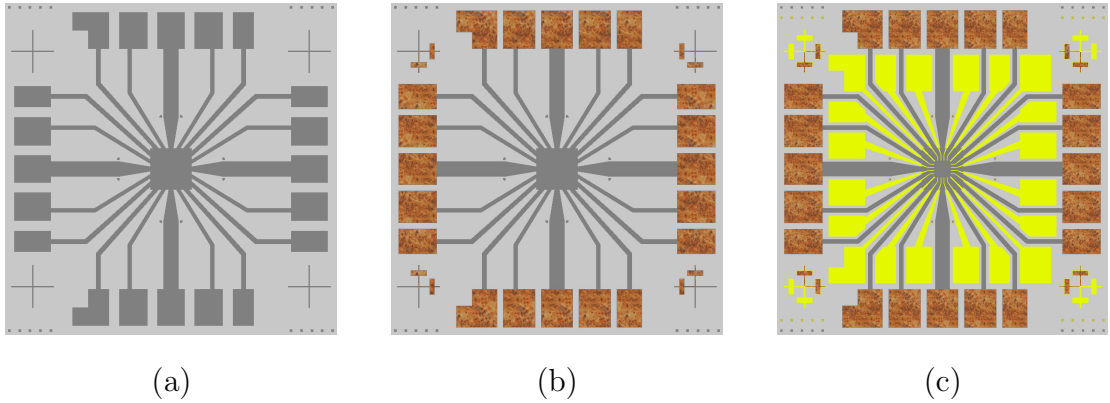


**Figure 3.3:** Optical lithography steps of the general purpose *JStar* pattern.

## 3.2 Fabrication

QDR devices were fabricated using standard semiconductor processing techniques, with a mixture of optical and electron-beam lithography. The surface gate pattern shown in Figure 3.1 necessarily required electron-beam lithography to realise due to its small feature size. However, larger scale features, such as bond pads and ohmic contacts, were also required. For these, a set of pre-existing optical masks, named *JStar*, was used. The basic processing steps for fabricating a *JStar* pattern are shown in Figure 3.3, and summarised below;

- (a) An etch removes the 2DEG from the majority of the chip, leaving a central  $200\ \mu\text{m} \times 200\ \mu\text{m}$  mesa in which to place a device, and 20 connecting legs. The etchant used is  $\text{H}_2\text{SO}_4 : \text{H}_2\text{O}_2 : \text{H}_2\text{O}$ , in the proportions 1:8:80.
- (b) Annealed ohmic contacts are defined on bond pads at the end of each of the legs. The contacts are patterned from evaporated AuGeNi, using a lift-off process. They are then annealed at  $430\ ^\circ\text{C}$  for 80 s to contact the 2DEG.
- (c) Metal gates with bond pads are evaporated. The gates rise up onto the central mesa where they can be extended by further lithography to form a device. The gates are patterned, again via lift-off, from evaporated Ti/Au or NiCr/Au of approximately 10 nm/300 nm thickness.

To define the fine-feature surface gates, an electron beam lithography stage was performed between steps (b) and (c) above. The resist used was a 100nm thick layer of PMMA, deposited as two 50nm thick layers, spun one on top of the other.

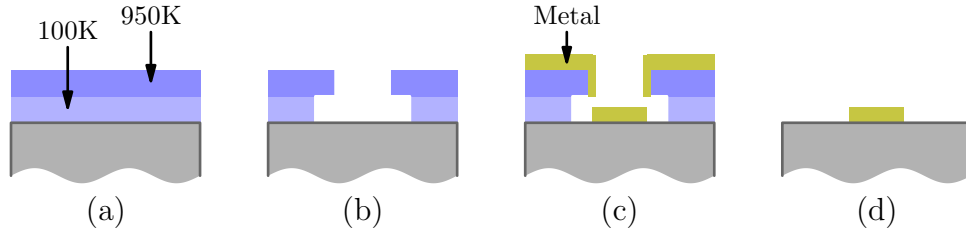


**Figure 3.4:** (a) Initial resist layers. (b) Resist profile after exposure and development. The undercut comes from the difference in development rates of the two PMMA layers. (c) Metal evaporation. The resist profile aids lift-off by preventing evaporated metal that may have coated the resist walls from joining onto the gate. (d) Gate metal after removal of resist.

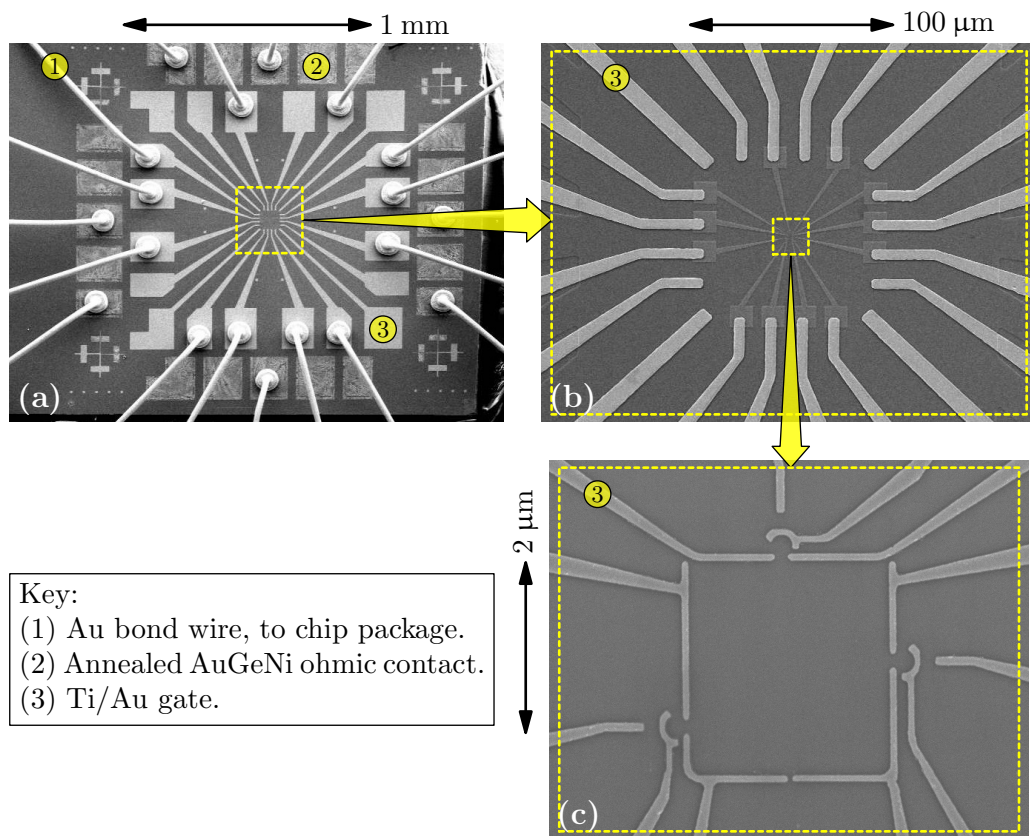
The two layers were of different molecular weight, the lower being 100K and the upper being 950K. Higher molecular weight PMMA produces a higher contrast ratio for a given exposure dose and dissolves slower in a solvent developer. It was hoped that this two-layer process would produce a resist profile to aid the lift-off of the evaporated metal, as shown in Figure 3.4. The evaporated metal for the fine-feature gates was typically a sticking layer of 5 – 10 nm of NiCr or Ti, followed by a 20 nm layer of Au.

Figure 3.5 shows SEM images of a typical completed device that has been packaged in a 20-pin LCC chip holder.

### 3.3 Measurement setup

All of the measurements presented in this chapter, were made on the device *dc5-4a* (see Appendix A.2). The device was cooled in a dilution refrigerator with a base temperature of approximately 40 mK. The fridge is located in a screened room to reduce the coupling of environmental RF radiation to the experiment and the measurement electronics. Standard high-frequency line filters are used on all electrical connections passing through the screened room walls.

Electrical connection to the device was made via twenty, low-frequency lines. These run from a break-out box at room temperature, into the vacuum space of the dilution fridge, and down to the sample holder. Before the sample holder, all twenty lines pass through low-pass, three-pole, RC filters, which are thermally anchored to the mixing chamber of the fridge. These reduce noise in the measurement wiring, and the related increase of electron temperature in the device. The filters were de-



**Figure 3.5:** (a)-(c) Sequentially smaller scale SEM images of a completed device.

signed to have a cut-off frequency of approximately 3 MHz. In addition, the device was enclosed in a metal can, also thermally anchored to the mixing chamber, to shield from radiation from nearby 4 K surfaces. These techniques of ‘cold shielding’ and ‘cold filtering’ are widely used for achieving low electron temperatures. For details of the filters and the shield, see Appendix B.2.

The voltages applied to the twelve surface gates were supplied by digital-to-analogue converters (DACs).<sup>2</sup> Every connection to a gate was made to pass through a room temperature RCR filter, consisting of two 1 M $\Omega$  resistors in series and a 0.1  $\mu$ F capacitor to ground. These provided protection to the fragile gates from sudden voltage spikes or large injections of charge. The filters were connected to every gate line on the break-out box before inserting the device into the sample holder, and remained connected throughout the experiment.

The transport properties of the device were studied by measuring two different quantities: differential conductance, measured with a lock-in amplifier, and direct current, measured with an electrometer. To measure non-linear transport, a constant bias voltage,  $V_{SD}$ , could also be applied across the device.<sup>3</sup> Details of the two different measurement setups are given in Figures 3.6 and 3.7.

## 3.4 Device characterisation

The first measurements performed on the device were to characterise separately its logical components, namely the three quantum dots and the isolated 2DEG. The aim of these measurements was to confirm that at least two quantum dots could be created on the perimeter of the isolated 2DEG; that these dots were small enough to have state spacings much larger than  $k_B T$ ; and that the isolated 2DEG was large enough for its own state spacings to be smaller than  $k_B T$ .

### 3.4.1 Quantum dots

Of the device’s twelve surface gates, nine were required to form the three quantum dots. These gates have names, as shown in Figure 3.1, which end with ‘PL’ (for ‘plunger’), ‘IN’ (for ‘inside barrier’), or ‘OUT’ (for ‘outside barrier’). The first

<sup>2</sup>The DACs used were Keithley *KUSB3116* modules (re-branded Data Translation *DT9834*). Each provides 4 output voltages with 16-bit resolution over a range of  $\pm 10$  V. These were scaled to a  $\pm 5$  V or  $\pm 1$  V range, as required, using simple resistor networks.

<sup>3</sup>The bias voltage was provided by one channel of a 12-bit, IOTECH *488* DAC, which, in both types of measurement, was divided by  $10^3$  using a resistor network.

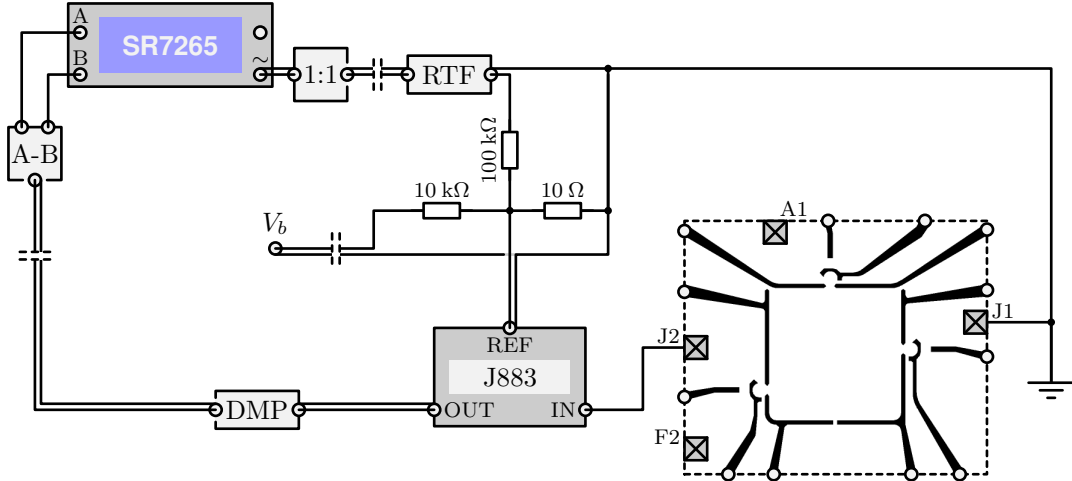


**Figure 3.6:** Schematic diagram of a typical differential conductance measurement using a Signal Recovery *SR7265* lock-in amplifier. The *J883* module is a current-to-voltage amplifier (see Appendix B.1). It equalises the voltage on its input (‘IN’) with the applied reference voltage (on ‘REF’). The voltage on ‘OUT’ is equal to the corresponding current through the device multiplied by a gain of  $10^7$  or  $10^8$  V/A. The resistor network divides a small ( $\sim 100$  mV), audio-frequency, AC signal from the lock-in by  $10^4$ , and a DC voltage ‘ $V_b$ ’ by  $10^3$ . Their sum is applied to the amplifier’s reference, and hence across the device. (Alternatively, it could also be connect to the ohmic contact ‘J1’ and the amplifier reference grounded.) The lock-in detects the component of the resulting signal on ‘OUT’ that is at the oscillator frequency; its in-phase component is proportional to the conductance of the device; its out-of-phase component is proportional to the susceptance. The readings from the lock-in are recorded by a PC, using a GPIB interface.

The lock-in amplifier is located outside the screened room. The dotted breaks in some lines indicate where they pass through the screened room walls, and the associated RF filters.

The ‘1:1’ module is an audio-frequency transformer, which is used to isolate the lock-in ground from the experimental ground. ‘RTF’ is a filter to remove kHz noise from the lock-in excitation signal. ‘DMP’ puts a resistive load between both the high and low of the preamp output, and the screened room filters. (The preamp is prone to oscillate if it tries to directly drive the capacitance of the filters.) ‘A-B’ serves to isolate the lock-in ground from the experimental ground. Details of all these modules can be found in Appendix B.3.

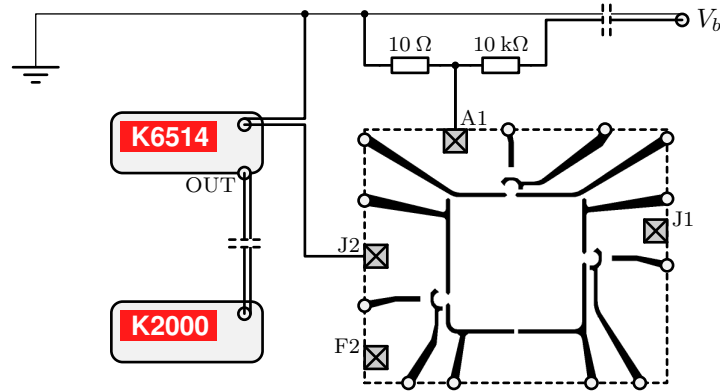


**Figure 3.7:** Schematic diagram of the direct current measurement setup. A Keithley 6514 electrometer is used to measure the current flowing between the ohmic contact ‘J2’ and ground, under the application of a bias voltage ( $V_{SD} = V_b/10^3$ ) to the ohmic contact ‘A1’. The electrometer is located inside the screened room. An analogue output, proportional to the electrometer’s reading, is sent outside the screened room, where it is measured by a Keithley 2000 multimeter. The multimeter is read by a PC, using a GPIB interface.

part of the gate name is either ‘T’, ‘L’ or ‘R’, indicating that it is associated with the top, left or right dot. To find the voltages required on these gates to form a particular dot, the differential conductance of the device was measured while sweeping the appropriate ‘-PL’ gate. (A measurement setup similar to that shown in Figure 3.6 was used, but connecting to different ohmic contacts depending on the dot being probed.) If the ‘IN’ and ‘OUT’ barrier gate voltages had been chosen correctly to form a dot, the measurement showed the expected signature of Coulomb blockade: periodic peaks in conductance, separated by regions of zero conductance. An example of such a result seen in the right dot is shown in Figure 3.8.

Having identified the barrier gate voltages that produced a Coulomb blockade-like signal, the presence of each dot was confirmed by measuring its conductance over a range of bias voltages ( $V_{SD}$ ). Such measurements are expected to show Coulomb diamonds (as discussed in Section 2.2.3). Figure 3.9 shows finite-bias measurements made on each of the three dots.<sup>4</sup> They all show the zero-bias conductance peaks evolving as expected for Coulomb blockade: the peaks split linearly with bias, revealing structure due to the dot’s spectrum of states within the result-

<sup>4</sup>For the measurement shown in Figure 3.9(a), the lock-in excitation was applied directly to the ohmic contact ‘A1’, while the DC bias was applied to the reference input of the preamplifier. The preamplifier was connected to the ohmic contact ‘J1’. For Figure 3.9(b), the setup was identical to that in Figure 3.6. For Figure 3.9(c), the sum of the excitation and the bias were applied to ‘A1’, and the preamplifier was grounded.

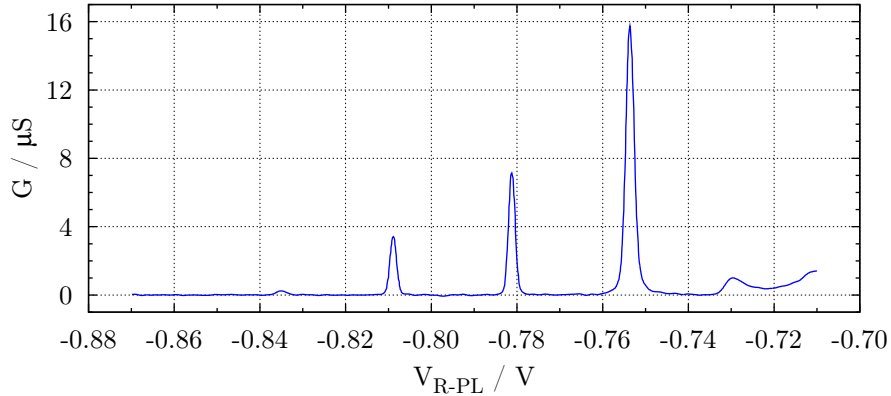


**Figure 3.8:** Typical signature of Coulomb blockade, measured in the right dot with the barrier gate voltages of  $V_{R-IN} = -0.670$  V, and  $V_{R-OUT} = -0.540$  V. The mixing chamber temperature was 43 mK.

ing triangles.

The charging energies of the dots can be found from the data in Figure 3.9. The dotted lines in the figure follow the edges of the Coulomb diamonds and their gradients can be used to find the conversion ratio between the plunger gate voltage, and dot energy. For the top, left, and right dots, these ‘lever-arms’ are found to be  $\alpha_G^T = 0.0811$  eV/V,  $\alpha_G^L = 0.0533$  eV/V and  $\alpha_G^R = 0.0336$  eV/V respectively. Using these values, the zero-bias peak spacings can be converted into energies. This gives charging energies for the top, left, and right dots of  $E_{CB}^T = 1.5$  meV,  $E_{CB}^L = 1.2$  meV, and  $E_{CB}^R = 0.9$  meV respectively.

One of the requirements for realising an efficient QDR is that the quantum dots have large energy separation between their single-particle states, compared to  $k_B T$ . As discussed in Section 2.2.2, the separation of excited states in a dot is expected to be dependent on the number of electrons it holds and the strength and particular shape of the confining potential. Given that neither of these can be determined or predicted easily, it is necessary to check the lowest excited state energies in each dot for every different tuning of the device.

Figure 3.10 shows a non-linear measurement of differential conductance of the top dot, focusing on a single Coulomb blockade peak. Structure due to the first electron excited state can clearly be seen, with the energy of this state being approximately 200  $\mu$ eV above the ground state. Such a separation should, in principle, be sufficient for the QDR to operate up to temperatures around 2 K. From this, and other similar measurements, it was clear that the dots were able to achieve the

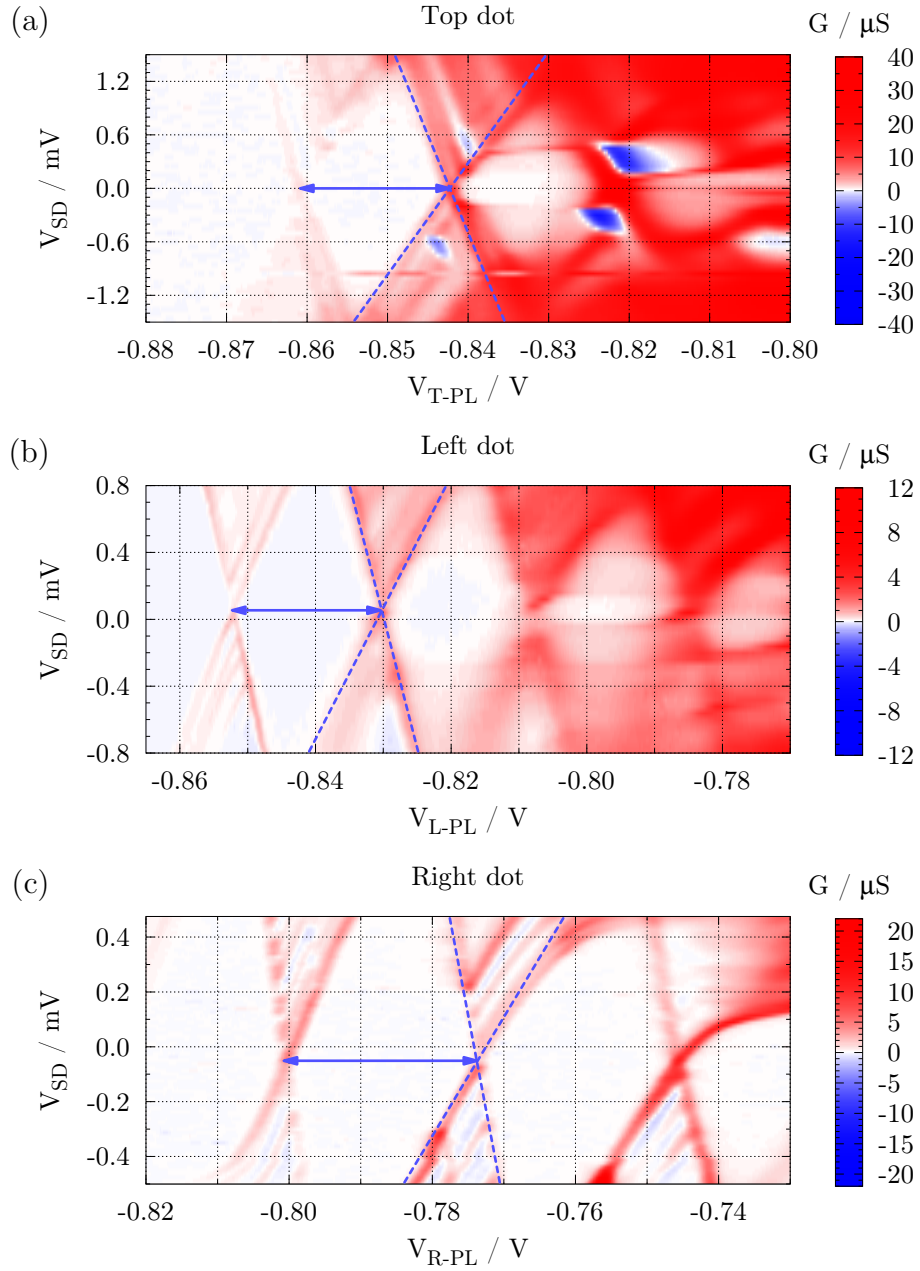


**Figure 3.9:** Finite bias conductance measurements of the three quantum dots. The dashed lines are linear fits (by eye) to the blockade diamond edges. The arrows indicate the blockade diamond widths. The lock-in excitation for (a) and (b) was  $100 \text{ mV}/10^4 = 10 \mu\text{V}$ , and for (c) was  $50 \text{ mV}/10^4 = 5 \mu\text{V}$ . (a)  $V_{T-IN} = -0.631 \text{ V}$ ,  $V_{T-OUT} = -0.460 \text{ V}$ . (b)  $V_{L-IN} = -0.8093 \text{ V}$ ,  $V_{L-OUT} = -0.380 \text{ V}$ . (c)  $V_{R-IN} = -0.678 \text{ V}$ ,  $V_{R-OUT} = -0.542 \text{ V}$ .

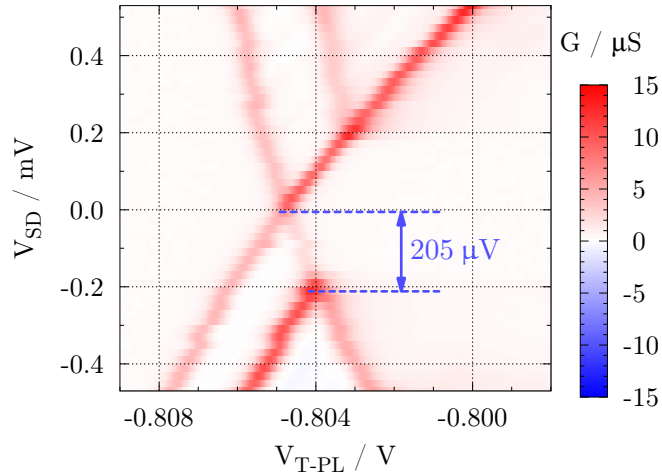


**Figure 3.10:** Differential conductance of the top dot under bias. (The bias is applied to the ohmic contact ‘J1’.) The first excited state is clearly visible, and has an energy approximately 200  $\mu\text{eV}$  higher than the ground state. The fridge mixing chamber temperature was 45 mK. The lock-in excitation was 10  $\mu\text{V}$ , and gate voltages were  $V_{\text{T-IN}} = -0.637$  V and  $V_{\text{T-OUT}} = -0.471$  V. A bias offset of 70  $\mu\text{V}$ , which is present the input of the preamplifier, has been subtracted for clarity.

large state separations required.

### 3.4.2 Central region spectroscopy

Some unexpected results were observed while taking non-linear transport measurements of the three dots: when unrelated gates were defined, many additional excited states seemed to appear in the dots. This is in fact the case in Figure 3.9(c), where many excited-state-like lines (running up and to the right) are seen inside all three unblockaded regions. However, it is impossible to identify the origin of these features from this measurement alone. In trying to identify the cause of this behaviour, and to confirm that the spacing of states in the dots was really as large as suggested above, a method for measuring the spectrum of states in the central region was unintentionally found.

After some investigation it was found that the additional excited-state-like features occurred when the side of the central region opposite the relevant dot was defined. For example, Figure 3.11(a) indicates the gates that were defined during the measurement in Figure 3.9(c). In this configuration the source electron gas is confined, in the vicinity of the right dot, by a potential well along the  $x$ -axis with

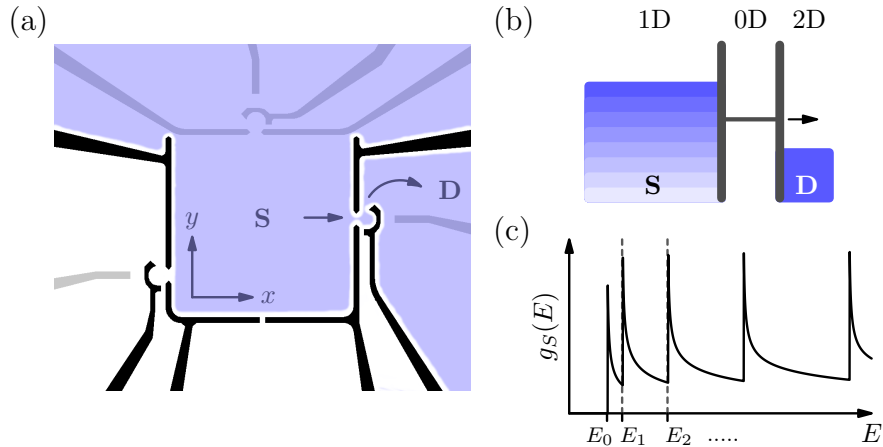


**Figure 3.11:** (a) Configuration of the device for central region spectroscopy measurements. Gates in black were defined during the measurement, while the others were held at 0 V. The light blue regions depict the extent of the source and drain electron gases in this configuration. The left hand dot was always completely pinched off. (b) Energy level diagram of 1D-0D-2D tunnelling. (c) Density of states in a quasi-1D system.  $E_n$  is the energy of the  $n^{\text{th}}$  sub-band.

a width of approximately  $2.4 \mu\text{m}$ .<sup>5</sup> This suggested that the extra features could be due to this confinement being strong enough to form a quasi-1D electron gas in the source. Transport through the system would then be determined not only by the spectrum of states in the quantum dot, but also by the non-constant (non-2D) density of states in the source.

The density of states of an ideal 1D electron gas is given by [121]:

$$g_{1D}(E) = \frac{1}{\pi} \left( \frac{2m^*}{\hbar^2} \right)^{1/2} \frac{1}{\sqrt{E}} \quad (3.5)$$

In a quasi-1D electron gas multiple 1D ‘sub-bands’ can exist. The  $n^{\text{th}}$  sub-band will be offset by an energy  $E_n$ . The values of  $E_n$  are found by solving for the quantised momenta allowed in the lateral confinement potential. For a harmonic potential well, the values of  $E_n$  are equally spaced in energy. For an infinite square well of width  $w$ , the sub-band energies are given by:

$$E_n = \frac{\hbar^2 \pi^2}{2m^*} \left( \frac{n}{w} \right)^2 \quad (3.6)$$

The density of states for a real quantum wire is the sum of the individual densities

<sup>5</sup>This well width assumes 100 nm of lateral depletion around the gates

for each sub-band. Figure 3.11(c) shows the density of states in a quasi-1D wire, laterally confined by a square-well potential.

To understand how transport through the dot is affected by the densities of states in the reservoirs, we consider first the general case of tunnelling through a dot with 2D reservoirs in the source and drain (2D-0D-2D tunnelling). By considering the balance of charge flows into and out of the dot, the current is found to be;

$$I \propto \int_{-\infty}^{\infty} G_{dot}(f_S - f_D)dE \quad (3.7)$$

In this expression,  $f_S$  and  $f_D$  are Fermi functions about the source and drain energies, which give the distribution of occupied states in the reservoirs.  $G_{dot}$  is a function describing the density of states in the dot. The tunnel couplings to the source and drain are assumed to be energy-independent.

When the dot is under a bias much larger than the thermal broadening of  $f_S$  and  $f_D$ , the result of the integral in Equation 3.7 will be dominated by an energy range over which  $f_S = 1$  and  $f_D = 0$ . The only energy-dependent term remaining in the expression is then  $G_{dot}$ . This is the why non-linear transport through a dot is a good probe of its energy level spectrum; by shifting  $G_{dot}$  in energy we can probe its structure without having to consider the leads too closely.

With a quasi-1D electron gas in the source (1D-0D-2D tunnelling), the situation becomes more complicated. The tunnel coupling of the dot to the source reservoir is now intrinsically energy-dependent due to the non-constant form of the quasi-1D density of states. This implies that the coupling will be larger at a sub-band edge than between sub-bands, even with completely uniform tunnel barriers. Including the tunnel couplings to the source and drain reservoirs ( $\gamma_S, \gamma_D$ ) modifies the expression for the current in the following way;

$$I \propto \int_{-\infty}^{\infty} \left[ \frac{1}{1 + \gamma_S/\gamma_D} \right] G_{dot}(f_S - f_D)dE \quad (3.8)$$

A qualitative understanding of 1D-0D-2D tunnelling can be gained from the simple case of a dot with a single, narrow energy level. If we make the approximation  $G_{dot}(E) = \delta(E - E_0)$  (where  $E_0$  is the energy of the dot state), and allow the tunnel coupling to the source to be energy dependent, then the integral in

Equation 3.8 reduces to;

$$I \propto \left[ \frac{1}{1 + \gamma_S(E_0)/\gamma_D} \right] (f_S(E_0) - f_D(E_0)) \quad (3.9)$$

In the situation where the dot is under a large bias and its energy is in the range where  $f_S = 1$  and  $f_D = 0$ , the only remaining energy dependent term in Equation 3.9 is  $\gamma_S$ . Therefore, in the case of a weakly-coupled dot with large energy spacings, transport through the system will be primarily determined by the tunnel coupling to the source, sampled at the energy of the dot's ground state. Assuming a uniform tunnel barrier to the source, this coupling will in turn be determined by the quasi-1D density of states. In a non-linear measurement of transport through the dot, we expect this to result in lines of non-zero differential conductance where the dot state aligns with each 1D sub-band. The lines should be parallel to the source-resonant edge of the blockade diamonds for both positive and negative biases. This is distinct from electron or hole excited states, which result in lines that follow one resonance for positive bias and the other for negative bias. The lines should also alternate between positive and negative differential conductance. (Due to the form of the 1D density of states, an *increase* in bias may pull the dot ground state below a 1D sub-band minimum, resulting in a *reduction* in current.)

With close inspection, all the features described above can be seen in Figure 3.9(c). Further evidence that most of the excited-state-like lines seen in this measurement are due to the confinement of the source reservoir can be found in the results shown in Figure 3.12. This shows similar measurements in which transport through the device is measured under a constant bias, as nearby gate voltages are changed. The excited-state-like features in the measurement are found to move in response to the gate 'L-PL', but not 'L-IN', while the dot energy is not affected appreciably by either. This indicates that the extra features are not due to the dot, and most likely originate from the region of the source adjacent to the dot.

Figure 3.12(d) shows that approximately six of the extra peaks fit within the bias-window. If these peaks are due to the dot ground state passing 1D sub-bands in the source, then the sub-bands would have an energy spacing of approximately  $0.7 \text{ meV}/6 = 117 \text{ } \mu\text{eV}$ .

To find if this is a plausible value for the 1D sub-band spacing, we return to Equation 3.6. Differentiating with respect to  $n$  gives an expression for the energy

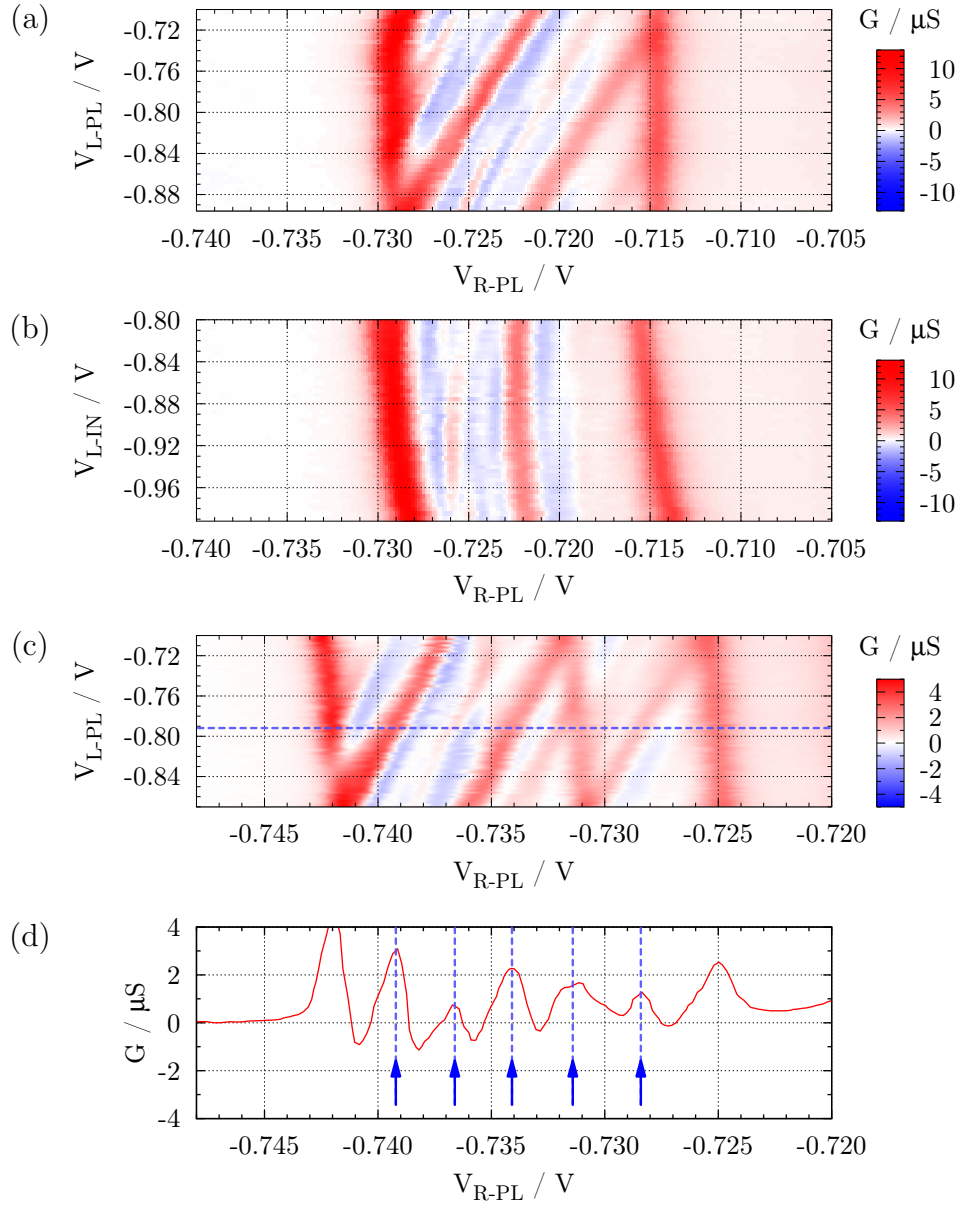


**Figure 3.12:** Differential conductance of the device with gates defined as per Figure 3.11(a). In (a) and (b) a bias of  $-0.5$  mV is applied to the source. In (c) and (d) the bias is  $-0.7$  mV. (a)-(d) show a bias-split region of transport through the right hand dot. (a) As  $V_{L-PL}$  is made more negative the fine structure shifts to higher energies. The region itself does not move. (b) Neither the fine structure or region moves appreciably with  $V_{L-IN}$ . (c) shows the same as (a), but at the higher bias. The extra line at  $V_{R-PL} \approx -0.731$  V, which does not move with  $V_{L-PL}$  in the same way as the fine structure, is an excited state of the dot that now lies within the bias window. (d) shows a single line-scan from (c) at a position of  $V_{L-PL} = -0.791$  V. The arrows indicate the approximate position of peaks in the fine structure.

level separation in a square well:

$$\Delta E(n) = \left( \frac{\hbar^2 \pi^2}{m^*} \right) \frac{n}{w^2} \quad (3.10)$$

For a well width of 2.4  $\mu\text{m}$ , and a sub-band spacing of 117  $\mu\text{eV}$ , this implies that approximately 60 1D sub-bands are populated in the source. Given a Fermi energy of 4.68 meV for this material, Equation 3.6 predicts that a 2.4  $\mu\text{m}$  well should be populated up to the 69<sup>th</sup> sub-band, and have a sub-band separation at the Fermi energy of 134  $\mu\text{eV}$ . Any discrepancy between the two values could come from an over-estimation of the well width, an under-estimation of the Fermi energy, or the fact that the lateral confining potential is not exactly square.

From this measurement we can estimate what the state separation in the central region will be once it is fully isolated. From the lithographic symmetry of the device we assume there will be 60 allowed values of  $k_y$  as well as 60 allowed values of  $k_x$ . The total number of trapped electrons will be  $60^2 \pi / 2 \approx 5655$ .<sup>6</sup> Accounting for spin degenerate states, this yields an average state separation of  $E_F / 2828 = 1.7 \mu\text{eV}$ .

In conclusion, the appearance of extra excited-state like structure in non-linear transport measurements of the dots is attributed to a formation of a quasi-1D electron gas in the partially formed central region. Using the right hand quantum dot to probe the source's density of states, a sub-band spacing of approximately 117  $\mu\text{eV}$  is found. This is similar to the predicted value for a square-well potential of width 2.4  $\mu\text{m}$ . From the device's symmetry an average energy state separation of 1.7  $\mu\text{eV}$  is predicted for the fully isolated central region. This corresponds to a temperature of 20 mK, and so we expect this region to behave as a 2D electron gas in the temperature range of the experiment, as required.

### 3.4.3 Fully isolated central region

The final stage of characterising the device was to study the fully defined central region. Both differential conductance and DC transport were measured while only defining the '-PL' and '-IN' gates. Of the three possible openings around the edge of the central region (between each pair of '-PL' and '-IN' gates) one was always kept completely pinched off, while two were left open as connecting leads to the

<sup>6</sup>The number of electrons is given by a quarter of the area of a circle in k-space (with a radius of 60), multiplied by a factor of 2 to account for spin degeneracy. The value found compares well with the prediction from the carrier density in the material;  $nA \approx 7500$ .

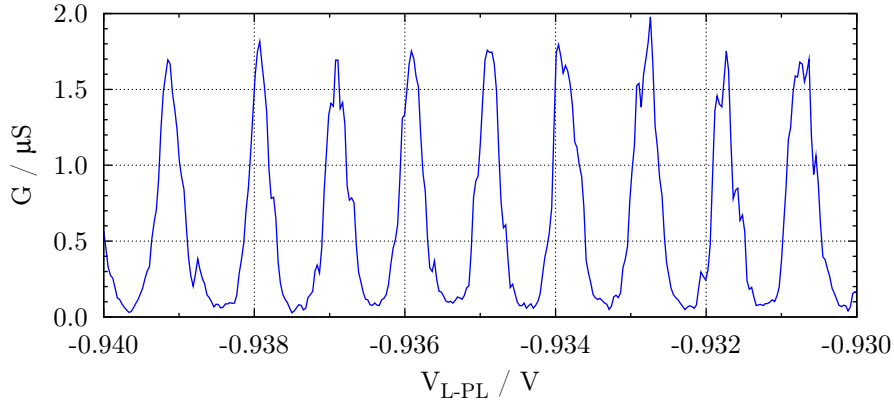


**Figure 3.13:** Differential conductance of the device, with no applied DC bias. The measurement setup is as per Figure 3.6, but with the lock-in excitation applied directly to the ohmic contact ‘A1’, and the preamplifier connected to ‘J1’. The lock-in excitation was  $5 \mu\text{V}$ . The period of the oscillations is approximately  $1.1 \text{ mV}$ .

source and drain reservoirs.

When the two leads were set to have one or more populated 1D sub-bands, the conductance showed reproducible fluctuations in response to sweeping various gates. This behaviour was most likely due to Universal Conductance Fluctuations (UCFs) in the central region. Such fluctuations are known to occur due to changes in the complex pattern of interfering wavefunctions, created when electrons are confined to a region smaller than their phase coherence length. [122]

When the leads were tuned to low conductances ( $\ll e^2/h$ ), the UCFs were suppressed and the conductance became dominated by regular peaks. (See Figure 3.13.) This was suggestive of Coulomb blockade, which would imply a central region capacitance small enough to produce a significant charging energy. To verify the presence of Coulomb blockade, a non-linear transport measurement was made (Figure 3.14), as well as a magnetic field sweep. The non-linear transport showed a weak signature of Coulomb blockade, with an estimated charging energy of  $100 \mu\text{eV}$ .<sup>7</sup> The magnetic field dependence showed the position and shape of the peaks to be largely insensitive to field up to  $2 \text{ T}$ , which is expected for Coulomb blockade given that it is an electrostatic effect.

With a small total capacitance for the central region it is likely that the capacitive coupling to the adjacent dots would be significant. To investigate this, the central region was set up in the Coulomb blockade regime with leads in the top and

<sup>7</sup>This value is found more rigorously in Section 4.3.4

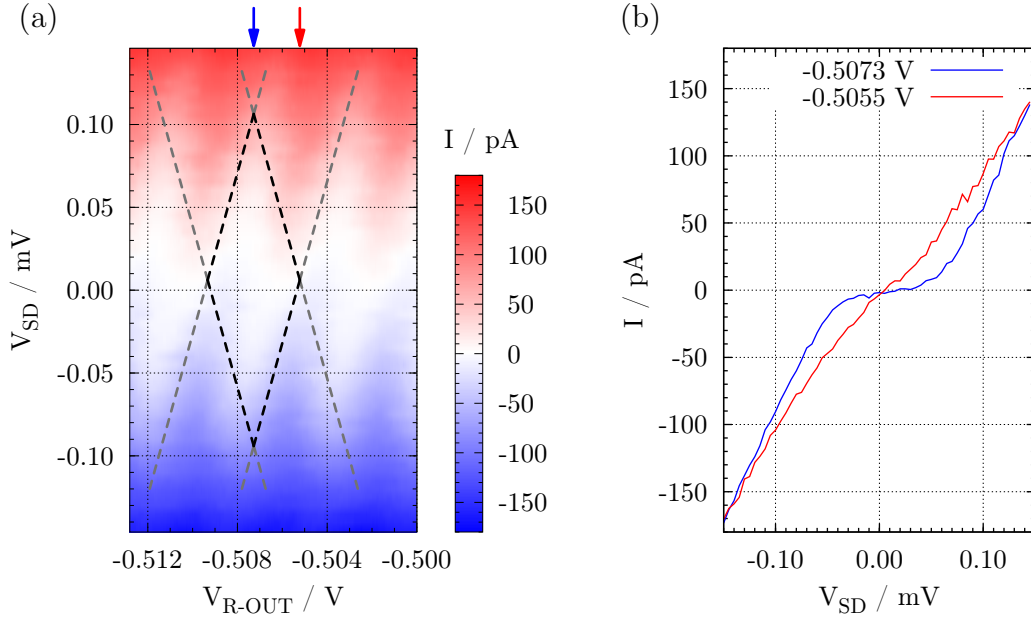


**Figure 3.14:** (a) Current through the device, measured using the setup shown in Figure 3.7. (An offset in bias, due to a small voltage on the electrometer input, has been subtracted for clarity.) Periodic peaks in current are seen at low bias. These widen with increasing bias until, when  $|V_{SD}| \gtrsim 130 \mu\text{V}$ , they completely overlap and merge together. This widening with bias is indicative of Coulomb blockade, although the signature is much weaker than in the results shown earlier for the smaller dots. The dotted lines highlight the widening of two adjacent peaks, and the diamond region between them within which conduction is suppressed. From the height of this diamond, the charging energy of the central region is estimated to be  $100 \mu\text{eV}$ .

(b) Two line-scans taken from (a) at the points indicated by the red and blue arrows (appropriate values of  $V_{R-OUT}$  are indicated in the key). The red trace shows nearly ohmic behaviour at the centre of a conductance peak. Taken from between two peaks, the blue trace shows a bias range within which transport is suppressed.

left sides, and additionally the right hand dot was formed in an extremely isolated regime. Coulomb blockade oscillations in the central region could then be measured while simultaneously altering the charge state of the adjacent dot. If a significant capacitive coupling existed between the two, then the ejection of a single electron from the dot should decrease the energy of the central region, resulting in a sudden shift in the phase of the observed Coulomb blockade peaks.

The current through the central region as a function of the gates  $V_{R-PL}$  and  $V_{R-OUT}$  is shown in Figure 3.15(a). It shows Coulomb blockade oscillations in the central region, which, as expected, are more sensitive to  $V_{R-PL}$  than  $V_{R-OUT}$ . (The former gate is closer to the central region.) It also shows a step in the otherwise regular CB oscillations at  $V_{R-OUT} \approx -0.550$  V. The position of the step evolves linearly with  $V_{R-PL}$  and is more sensitive to  $V_{R-OUT}$  than  $V_{R-PL}$ . This is consistent with it being due to a change in charge state of the right hand dot. Figure 3.15(b) shows that the step is approximately 24% of the distance between the Coulomb blockade peaks. Therefore, the ‘back-action’ energy between the dot and the central region is 24% of the central region’s charging energy.

Neither the presence of Coulomb blockade in the cooled electron gas of a QDR or strong capacitive coupling between its components were fully considered in the original proposal of Edwards et al. [1, 2]. Their primary consequence was that the planned method for measuring the central region temperature, which was to use a third, weakly coupled dot, was not feasible. The back-action would cause the energy of the central region to depend on the charge state of the thermometer dot. Therefore, the temperature measurement would no longer be non-invasive. Furthermore, the back-action also cast doubt on whether the device could function as a QDR at all. Both problems were finally solved by the development of a model that included electrostatic interactions, which is discussed in Chapter 4.

### 3.5 Thermometry measurements

Central to assessing the performance of the QDR is a measurement of the equilibrium temperature of a 2DEG in the device ( $T_e$ ). As discussed in Section 2.4, weak coupling between 2D carriers and lattice phonons will likely result in  $T_e$  being greater than the lattice temperature. Only if the QDR produces a temperature lower than  $T_e$  in the central region has it succeeded in cooling. It would also be interesting to know whether cooling below the lattice temperature ( $T_l$ ) occurs.

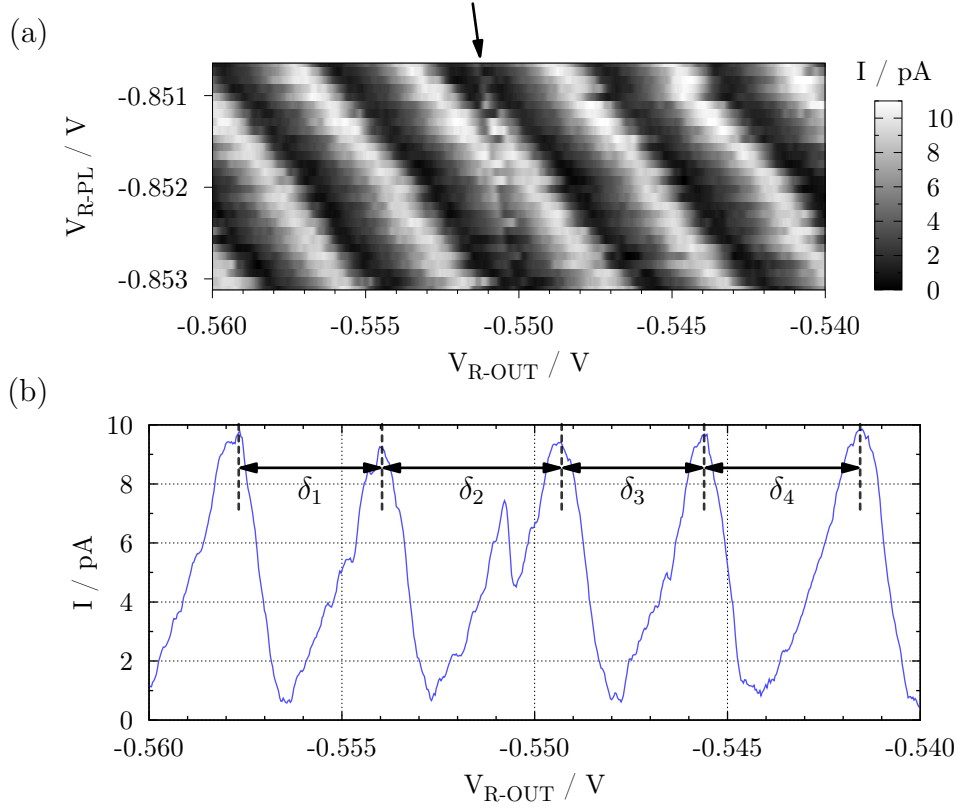


**Figure 3.15:** (a) Current through the central region under an applied bias of  $25 \mu\text{V}$  (accounting for the electrometer offset). An offset in the current of approximately  $-4 \text{ pA}$  has been subtracted for clarity. The arrow indicates a step-like feature in the Coulomb blockade peaks which is attributed to the change in charge state of an adjacent, isolated dot by one electron. (b) A single line-scan taken from (a) at a position  $V_{R-PL} = -0.8521 \text{ V}$ . The average normal peak spacing is  $\frac{1}{3}(\delta_1 + \delta_3 + \delta_4) = 3.8 \text{ mV}$ . The peak spacing including the step is  $\delta_2 = 4.7 \text{ mV}$ , which is 24% larger.

The lattice temperature of the device was not measured directly. Instead, the temperature of a Germanium thermometer on the cold finger is measured. (The fitting of this thermometer is shown in Appendix B.2.) A four-terminal, lock-in measurement was used to find the resistance of this thermometer and hence its temperature via a known calibration. It is assumed that the device lattice, the cold finger, and the mixing chamber of the fridge are all at the same temperature.

The equilibrium electron temperature was found at various mixing chamber temperatures from measurements of a single quantum dot. As discussed in Section 2.2.5, the widths of low-bias Coulomb-blockade peaks in a well-isolated dot are determined by the temperature of the 2D reservoirs. The line-shape of current through a biased dot is also determined by the temperature of the reservoirs, but here the source and drain temperatures can be determined independently.

Non-linear DC measurements of the left dot were used to measure  $T_e$ . The measurement setup shown in Figure 3.7 was chosen because, as will be discussed later, it was the same as used for measuring the QDR. This is significant because it is possible for the electron temperature, which is sensitive to electrical noise, to be dependent on the setup.

The dot was measured at several different mixing chamber temperatures. The temperature was elevated using a heater built into the mixing chamber. The heater was powered by a battery to avoid introducing additional electrical noise. An example result is shown in Figure 3.16. This was taken with the gates surrounding the central region defined, but with the opening between ‘T-PL’ and ‘T-IN’ set to a large conductance ( $\gg e^2/h$ ). (The opening between ‘R-PL’ and ‘R-IN’ was completely pinched off.) The gate ‘L-QPC’ has a small capacitance to the left dot, and so it was used to provide fine adjustments of its energy.

Given the previously determined spacing of dot states, it is clear that transport through the dot at low bias will be through the ground state alone. In this bias range ( $-0.15 \text{ mV} < V_{SD} < 0.15 \text{ mV}$ ), the maximum absolute current is roughly 80 pA. This corresponds to a tunnel rate for the dot barriers of  $\Gamma \approx 1 \text{ GHz}$ , and a lifetime broadening of the ground state of  $2\hbar\Gamma/k_B = 15 \text{ mK}$  [25, 123]. It is therefore likely that, at the base temperature of the fridge, the line-shape will be determined partially by lifetime broadening of the dot state as well as the thermal broadening of the reservoirs. However, since  $2\hbar\Gamma < k_B T_l$ , and  $T_l < T_e$ , the thermal broadening will dominate. At higher temperatures the lifetime broadening should be even less significant.

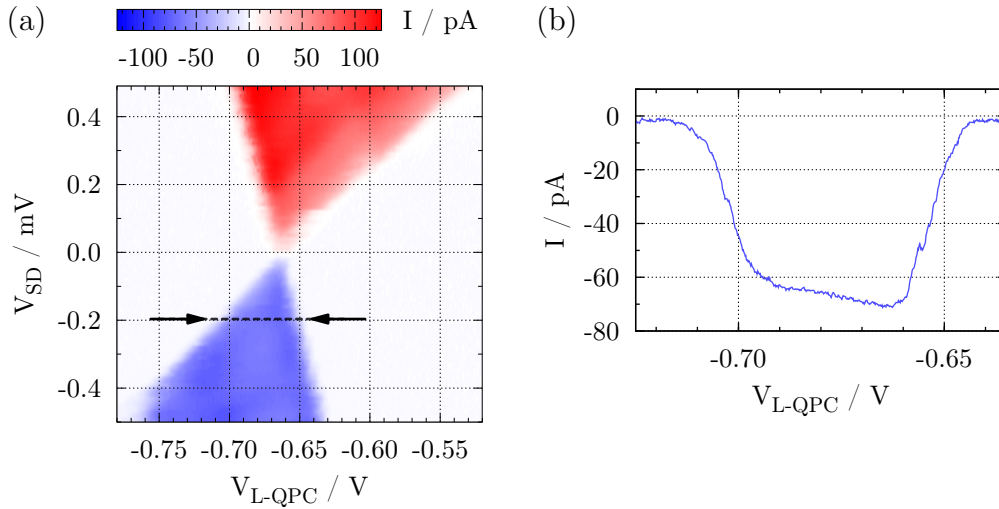


**Figure 3.16:** (a) Non-linear DC measurement of a single blockade peak in the left dot, at a mixing chamber temperature of 47 mK. (b) Line-shape of current vs.  $V_{L-QPC}$ , taken from (a) at the position indicated by the dashed line ( $V_{SD} = -0.2$  mV)

Two values are required to find  $T_e$  from the data in Figure 3.16. Firstly, the average width of Fermi functions that fit the line-shapes in current [e.g. Figure 3.16(b)] and secondly, the lever-arm for the dot. The temperature is given by the average width, converted from a voltage to an energy using the lever-arm. An analysis routine was written (in *GNU Octave*) to find both of these values from the raw data. The routine takes each sweep of gate voltage, such as in Figure 3.16(b), and fits one of two functions to the data. For low bias the fitted function is a top-hat, but with edges given by two Fermi functions of equal width, and the whole multiplied by a linear background. The linear background accounts for energy dependent tunnel rates, to first order. For higher biases, when the presence of excited states complicates the data, the fitted function allows for the Fermi functions to have different heights and different linear backgrounds. This is only fitted to data in a range of  $6k_B T_e$  about the centre of the two steps, as it will not describe the data well between them.

The analysis routine produces a graph of the fitted step positions and a mean value of the fitted step widths. A simple linear fit to the step positions is used to find the lever-arm ( $\alpha_G$ ), as explained in Section 2.2.3. Figure 3.17 shows the results of the analysis performed on the data shown in Figure 3.16. The mean of all the fitted Fermi function widths for this measurement is  $\bar{w} = (2.73 \pm 0.05)$  mV.

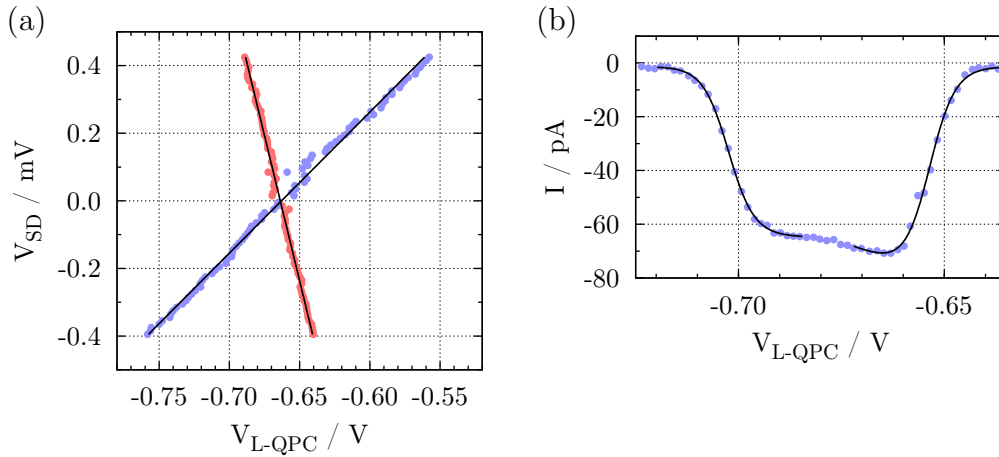


**Figure 3.17:** Analysis of the data shown in Figure 3.16. (a) The circles are fitted positions of the blocked region edges. The black lines are linear fits to these points. Their gradients are used to find the lever-arms;  $\alpha_G = (0.00336 \pm 0.00002)$  eV/V and  $\alpha_D = (0.195 \pm 0.002)$  eV/V. (b) The black lines are an example of a fit to a single line-scan, at a bias of  $V_{SD} = -0.2$  mV. The blue circles are the data; only every 10th point is plotted for clarity.

Converting this to a temperature gives  $T_e = \bar{w} \cdot (\alpha_G e / k_B) = (106 \pm 2)$  mK.

The analysis detailed above was repeated on several measurements taken at various temperatures. The results are shown in Figure 3.18.<sup>8</sup> The relation between electron and lattice temperatures is found to be approximately linear over this range. A weighted least-squares fit to the data gives the following relation and associated error:

$$T_e = (1.183 \cdot T_l) + 41 \text{ mK} \quad (3.11)$$

$$\sigma(T_e) = \sqrt{(0.094 \cdot T_l)^2 + (10.6 \text{ mK})^2} \quad (3.12)$$

That the relation between the two temperatures is approximately linear is not surprising given the small range in question. Additionally, the relatively small number of data points would make it difficult to resolve a more complicated trend.

<sup>8</sup>When converting fitted widths to temperatures, the lever-arm found from the data shown in Figure 3.16 was always used. Being the coldest measurement, it showed most clearly the blocked region edges and the fits to their position were therefore the most reliable. The lever-arm is not expected to change significantly with temperature.

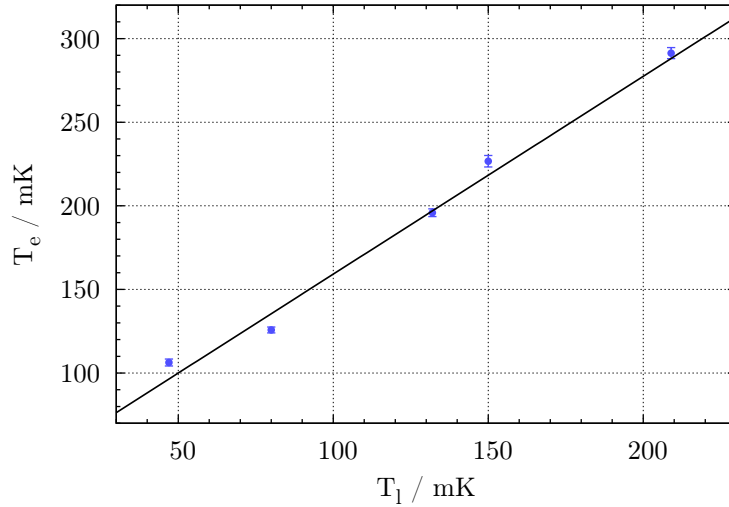


**Figure 3.18:** Electron temperature vs. lattice temperature. Circles are the electron temperatures extracted from several measurements. The black line is a weighted linear fit to these values (Equation 3.12).

### 3.6 Preliminary results

After characterising the individual components of the device, its behaviour as a full QDR-like system was investigated; the central region was defined and connected to the source (drain) reservoir via the left (top) quantum dot. The right dot was not formed, and ‘R-IN’ and ‘R-OUT’ were set to a voltage that depleted the channel between them. Current through the system, under the application of a constant bias voltage, was measured using the setup shown in Figure 3.7.

A DC measurement was chosen because of the complications of a lock-in measurement of such a device. In a lock-in measurement a small excitation is added to either the bias across a device ( $V_{SD}$ ) or a gate voltage ( $V_G$ ). In this way, either of the differential conductances  $G^{(b)} = \partial I / \partial V_{SD}$  or  $G^{(g)} = \partial I / \partial V_G$  can be measured. For a QDR,  $G^{(b)}$  is not expected to yield any useful information: in the cooling regime, as depicted in Figure 2.14,  $G^{(b)}$  should be zero as a small change in bias does not change the current. (In reality energy-dependent tunnel barriers and excited states in the two dots may cause the current to change, but neither of these effects are of immediate interest.)

Instead of measuring  $G^{(b)}$ , a gate excitation could be used to measure  $G^{(g)}$ . However, in this case it is unclear which gate should be used. Any gate which perturbs  $\mu_A$ ,  $\mu_B$  or  $\mu_C$  is expected to have a significant effect on the current in some,

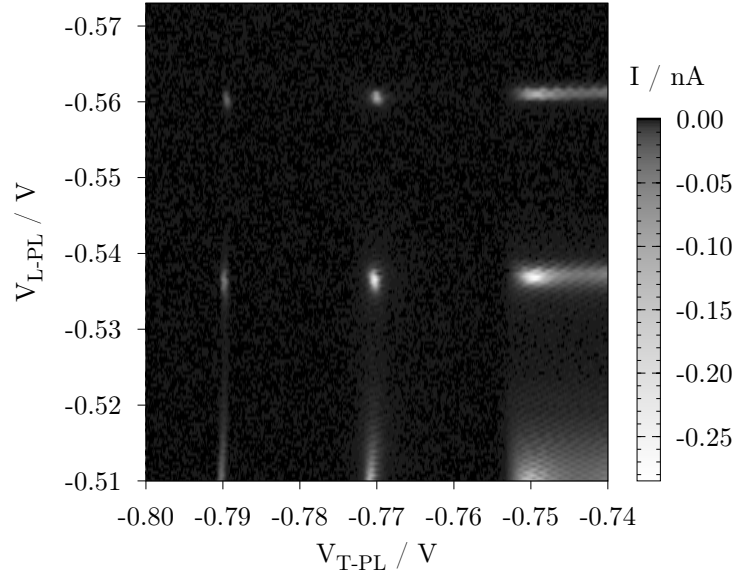


**Figure 3.19:** Transport through the QDR, under a bias of  $-75 \mu\text{V}$ , as a function of the top and left dot energies. Both dots are open in the bottom right of the plot, and more isolated in the top left.  $T_l = 49 \text{ mK}$ ,  $T_e = (99 \pm 12) \text{ mK}$ .

but not all, situations. The best choice would be to apply an excitation to two gates, such that  $\mu_A$  and  $\mu_B$  are modulated simultaneously but  $180^\circ$  out of phase. This would measure the response of the current to changes in  $(\mu_A - \mu_B)$ , which should show useful information in the cooling regime. However, this is difficult to realise in practice as it requires thorough characterisation of the lines connecting to the gates; their resistance and reactance when cold must be known and accounted for in order to produce a balanced excitation of the dots. Because of these difficulties, a DC measurement was chosen.

Figure 3.19 shows the measured current through the device as a function of the top and left dot plunger (‘-PL’) gates. The result is a set of points of conduction arranged on a roughly square grid. These points occur when both of the two dots are unblockaded; i.e. they have a state available for transport within the bias window. The spacings of the points are therefore determined by the charging energies of the dots. Along the bottom of the plot, where the left dot is open, and along the right side, where the top dot is open, the Coulomb blockade signatures for the individual dots are recovered. Overlaid on the entire plot, but most visible in the bottom right, are a series of faint, closely spaced lines. These are due to Coulomb blockade in the central region.

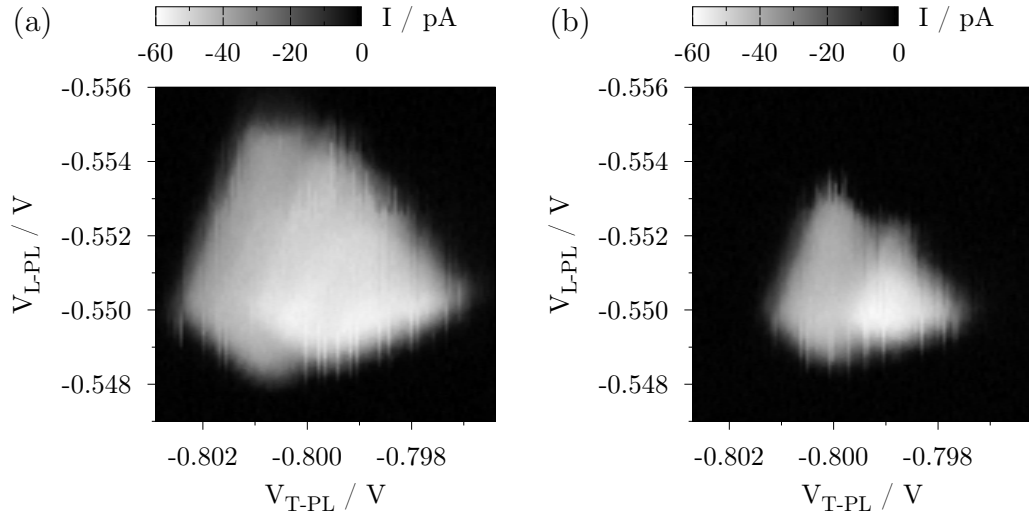


**Figure 3.20:** Detail of a conduction under two different biases. (a) Large bias point;  $V_{SD} = -500 \mu\text{V}$ ,  $T_l = 41 \text{ mK}$ ,  $T_e = (89 \pm 11) \text{ mK}$ . (b) Smaller bias point;  $V_{SD} = -300 \mu\text{V}$ ,  $T_l = 43 \text{ mK}$ ,  $T_e = (92 \pm 11) \text{ mK}$ .

Because current flows while states in both dots lie within the bias window, the size of the conduction points is proportional to the bias. Figure 3.20 shows a single conduction point under two different biases. Its exact shape is determined by electrostatic interactions in the system. (This is discussed in more detail in Section 4.3.1.) The fact that the points resemble two similar, overlapping shapes is attributed to the presence of an excited state in one of the small dots, with an energy smaller than the bias. In both these measurements, therefore, the bias is too large to achieve efficient cooling: the refrigeration scheme requires that transport through both of the dots can only occur through a single state.

To achieve optimum operation of the QDR, a bias voltage greater than  $k_B T_e / e$  is needed. This ensures that, when cooling, there is a high probability that states in the source are full and states in the drain are empty at the dot energies. A bias of  $75 \mu\text{V} \approx (870 \text{ mK}) k_B / e$  was chosen, being less than both the excited state energies in the dots, and the charging energy of the central region. With this bias, the energy levels of the device most closely resemble the ideal case of Fig. 2.14.

A further complication of measuring the device was the coupling between the central region and the gates used for probing dot energies. To remove this effect the couplings were calibrated so that, by changing pairs of gates simultaneously, the net change of the central region energy would be zero. Figure 3.21 shows the results of two calibration measurements, which allowed the effect of ‘T-QPC’ and

‘L-QPC’ on the central region to be compensated by using ‘R-OUT’.

When making measurements using the gates ‘T-QPC’ and ‘L-QPC’, the most commonly used procedure was to obtain data while sweeping the gates in opposite directions. A diamond shaped area of the ‘T-QPC’ vs. ‘L-QPC’ plane could then be mapped out from many such sweeps. Because the couplings of the two gates to the central region were found to be essentially the same, no compensation was necessary during each sweep. All that was required was an appropriate change in ‘R-OUT’ between each sweep, when both the two gates were stepped by a small amount in the same direction. Figure 3.22 shows the results of a calibration measurement which achieves this. Unless otherwise stated, all subsequent measurements include such compensation.

Figure 3.23 shows a conduction point with a bias of  $V_{SD} = 75 \mu\text{V}$ . For the particular point shown here both the dots were well isolated, but open just enough to give a measurable current. This was done to keep the lifetime broadening of the states in the dots below  $k_B T_e$ , which is a further requirement for efficient operation of a QDR. This measurement is, therefore, the first example of the device being configured as a QDR in a regime where cooling might be expected.

It is instructive to consider how the energies of the two dots change over a conduction point. In Figure 3.23, in the diagonal direction from top right to bottom left the two dot energies are changing in opposite directions at roughly equal rates. In the direction perpendicular to this, they are changing equally. Bearing in mind the energy level diagram in Figure 2.14, we can deduce that the bottom left edge of the conduction point corresponds to the condition that  $\mu_A \approx \mu_B$ . Below and to the left of this,  $\mu_A \ll \mu_B$  and so no current may flow. Above and to the right,  $\mu_A > \mu_B$  and so current may flow while both  $\mu_A$  and  $\mu_B$  remain within the bias window. It is therefore in the vicinity of this bottom left edge that the QDR should be tuned to the cooling regime.

After extensive characterisation of the device, it was now possible to obtain measurements, such as in Figure 3.23, in which the region of parameter space where the device should be acting as a QDR could be readily identified. However, without a way to measure the temperature of the isolated electron gas, it was not possible to ascertain directly whether or not any cooling was taking place. To solve this problem a more involved analysis was required, and this is discussed in the following chapter.

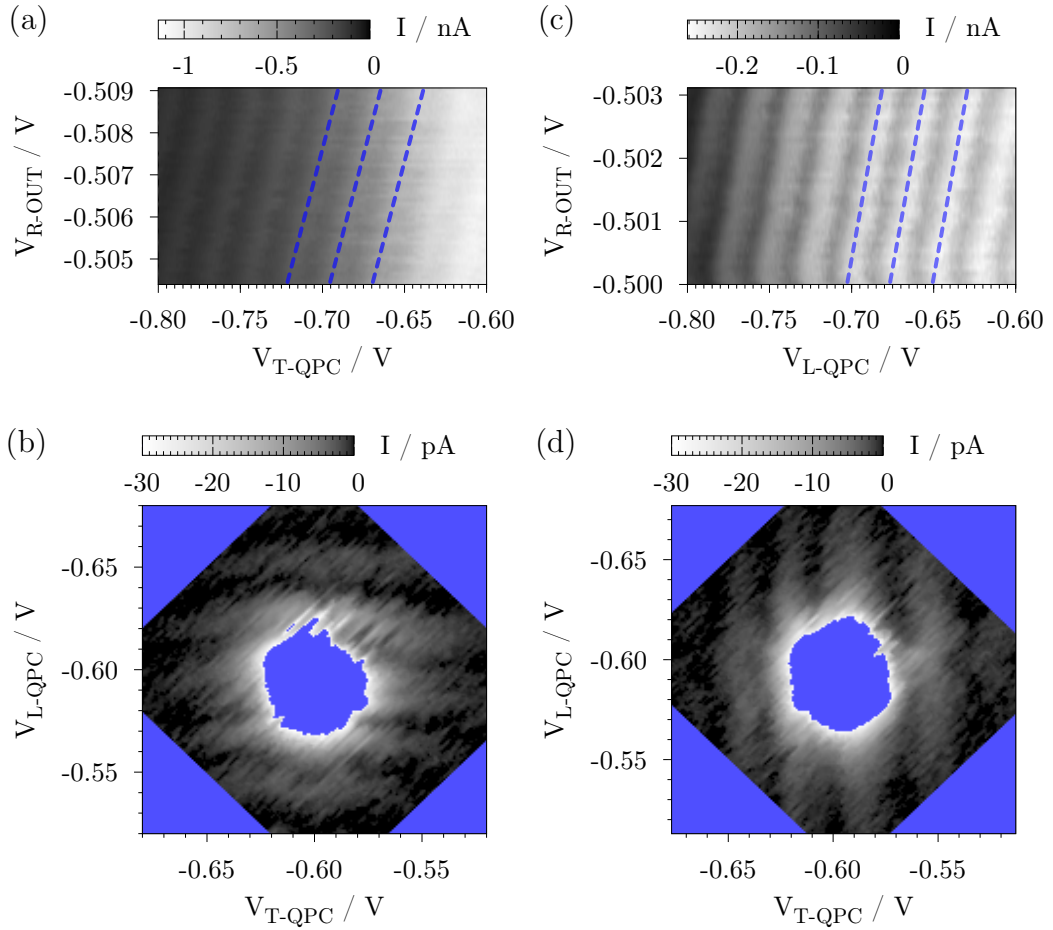


**Figure 3.21:** The plots (a) and (c) show current through the central region, measured with tunnel barriers defined at the top and left openings. The energy of the central region is probed by a pair of gates in each plot. Coulomb blockade peaks are observed and, as expected, their positions are linearly dependent on each gate voltage. From linear fits, by eye, to the peak positions (dotted lines), a ratio is found from each plot:  $(\Delta V_{R-OUT}/\Delta V_{T-QPC}) \approx 0.15$ , for plot (a), and  $(\Delta V_{R-OUT}/\Delta V_{L-QPC}) \approx 0.15$ , for plot (c).

The plots (b) and (d) show a single conduction point of the fully defined QDR, under a bias of  $-75 \mu\text{V}$ . Both the top and left dots are relatively open and so Coulomb blockade in the central region can be seen as faint lines. The current scale has been reduced to show them more clearly. Blue regions indicate no data (in the corners), or  $I < -30 \text{ pA}$  (in the centre). In (b) the effect of ‘T-QPC’ on the central region energy has been compensated for by simultaneously varying ‘R-OUT’ according to the ratio found from (a). In (d) the same has been done for ‘L-QPC’, using the ratio from (b).

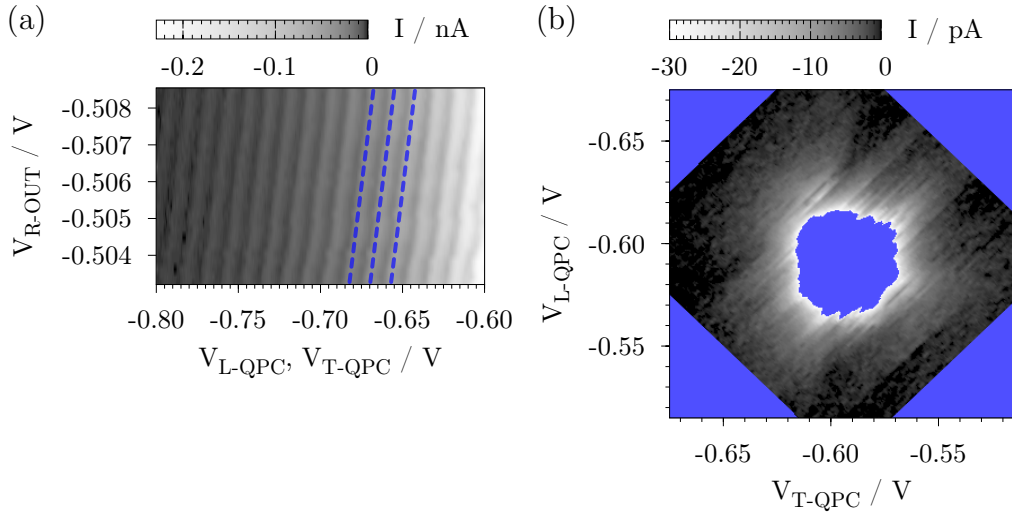


**Figure 3.22:** (a) Blockade peaks in the central region as ‘T-QPC’ and ‘L-QPC’ are swept together and ‘R-OUT’ is stepped. The dotted lines show  $(\Delta V_{R-OUT}/\Delta[V_{L-QPC}, V_{T-QPC}]) \approx 0.37$ . (b) The conduction point from Figure 3.21(b) and (d), with the effect of ‘T-QPC’ and ‘L-QPC’ on the central region cancelled by varying ‘R-OUT’ according to the ratio found in (a).

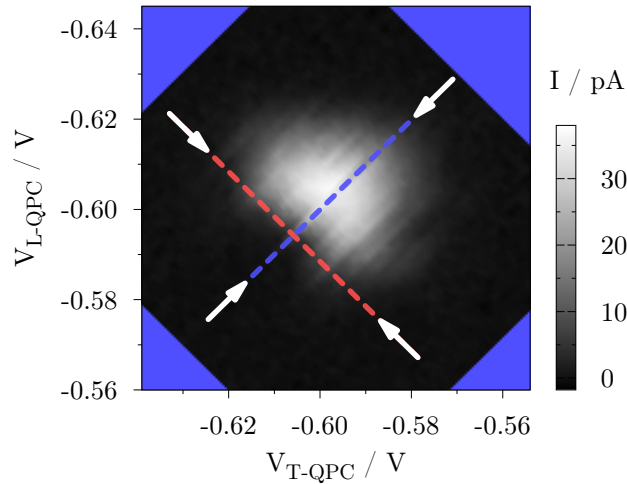


**Figure 3.23:** Measurement of a single conduction point, with  $V_{SD} = 75 \mu\text{V}$ . Along the red line  $\mu_A \approx \mu_B$ . Along the direction blue line the dot energies change in opposite directions and are equal at approximately  $\frac{1}{2}(\mu_S + \mu_D)$ .

# Chapter 4

## Quantum dot refrigerator: analysis

---

In the previous chapter, the design and characterisation of a Quantum Dot Refrigerator (QDR) device was discussed. The device was found to satisfy almost all known requirements for operating as a QDR, but the presence of significant electrostatic couplings between components of the system invalidated the planned scheme to use a third quantum dot to probe the temperature ( $T_C$ ) of the cooled 2DEG.

In the absence of an independent thermometer, the only alternative for finding  $T_C$  was to use the characteristics of the current through the QDR itself. The basic principle of how this is achieved is illustrated in Figure 4.1. In this simple situation, the QDR current is affected by the temperature of the reservoirs and the isolated 2DEG in a way that allows the two to be determined independently. The measurement is based on exactly the same physical principle as the independent thermometer (tunnelling through single-particle, quantum dot states), but applied in a more complex situation.

For the simplest case of a constant  $T_C$  it is relatively straightforward to calculate the exact form of the line-shape in Figure 4.1(b). However, we expect the central 2DEG to be heated and cooled by the current flowing through it. To predict the current in this situation, some a priori theory of how  $T_C$  changes with the electrochemical potentials of the dots is also required.

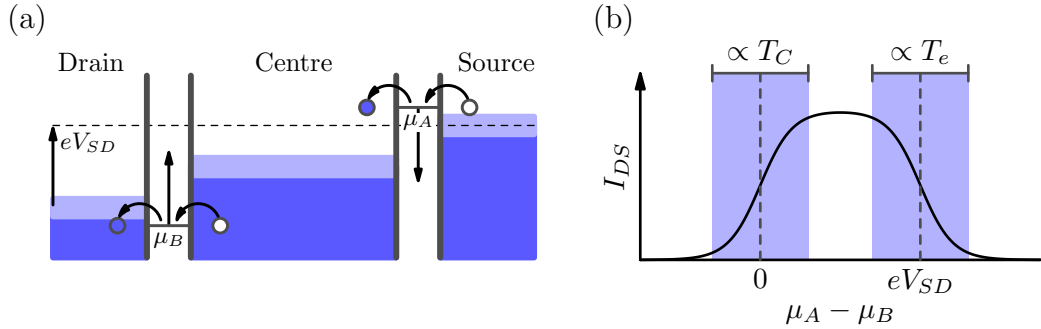


**Figure 4.1:** (a) QDR energy levels. Thermal broadening in the three 2D electron gases (source, drain and centre) is indicated by the light shaded regions. (b) Current from drain to source (electron flow from source to drain) as the electrochemical potentials of the two dots ( $\mu_A$  and  $\mu_B$ ) are moved simultaneously in opposite directions, as indicated by the arrows in (a). The onset of current at  $\mu_A - \mu_B = eV_{SD}$  is broadened by the temperature of the reservoirs ( $T_e$ ), while the switch-off of current at  $\mu_A - \mu_B = 0$  is broadened by the temperature of the centre ( $T_C$ ).

This chapter presents measurements of the QDR current made at various temperatures and their subsequent analysis. A simple model, which assumes constant  $T_C$  and neglects electrostatic effects, is initially fitted to the data. A reasonable agreement is found between the measured and predicted line-shapes of current, and this analysis strongly suggests that  $T_C$  is frequently lower than the equilibrium electron temperature ( $T_e$ ). A more complex model is then developed, which includes both electrostatic effects and changes in  $T_C$ , and this is also compared to measured line-shapes.

## 4.1 Temperature dependence results

A series of detailed measurements of the current through the device were made at different mixing chamber temperatures. Low-current conduction points were investigated because well-isolated dots are required for efficient cooling. Figure 4.2 shows three such points along with line-scans of current taken through the middle of each. In these line-scans, the right sides of the peaks correspond to the onset of transport as the dot levels pass the source and drain reservoirs. The left sides correspond to the switch-off of transport as the two dot levels pass each other. As the temperature increases, the right sides increase in width. This is expected because of the increasing thermal broadening of the reservoirs. The left sides, however, do not change as significantly.

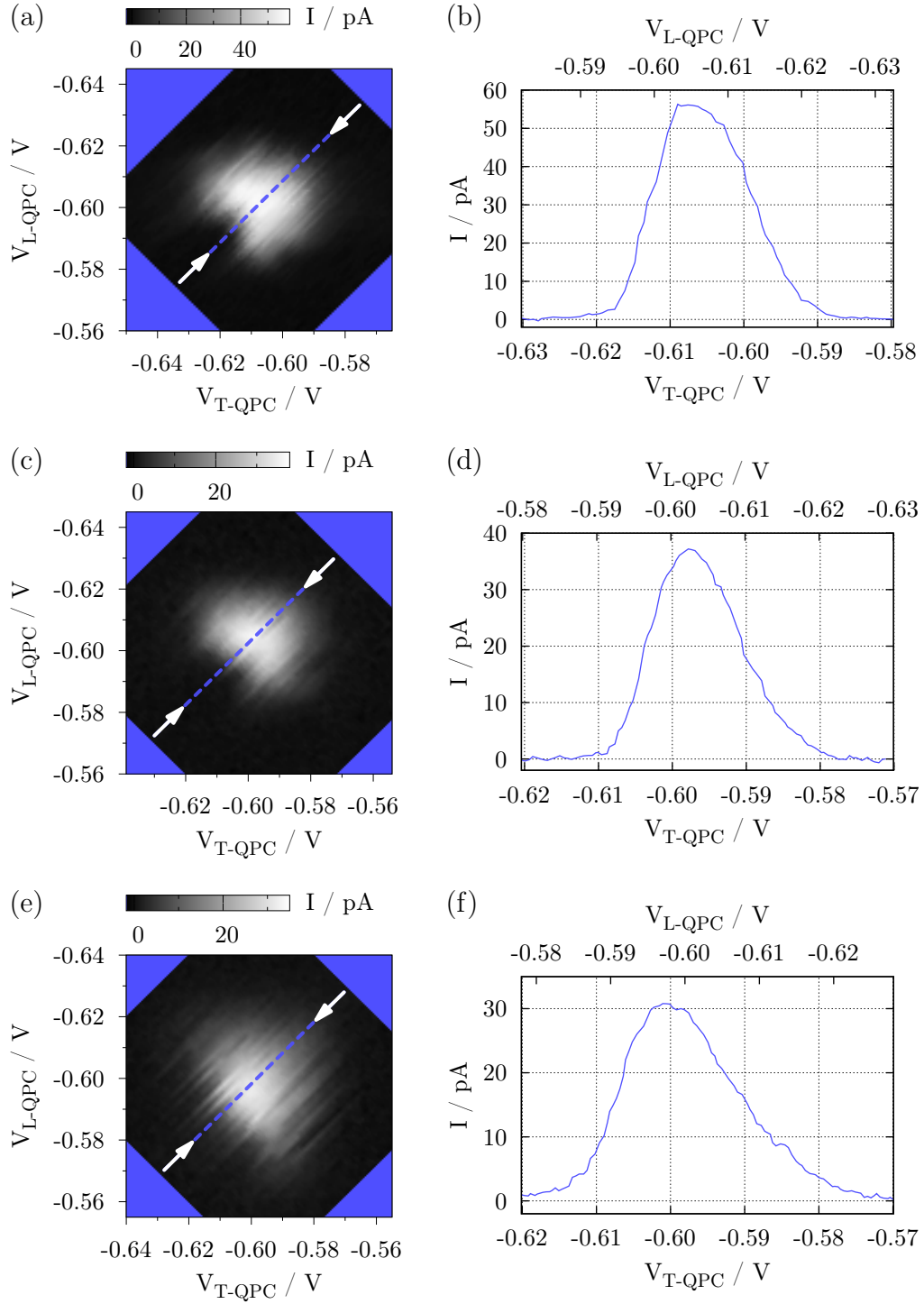


**Figure 4.2:** Conduction points with line-scans taken at the positions of the dotted lines. The three measurements were made at different lattice temperatures ( $T_l$ ). (a) and (b):  $T_l = 54$  mK,  $T_e = (105 \pm 12)$  mK. (c) and (d):  $T_l = 85$  mK,  $T_e = (141 \pm 13)$  mK. (e) and (f):  $T_l = 150$  mK,  $T_e = (218 \pm 18)$  mK.

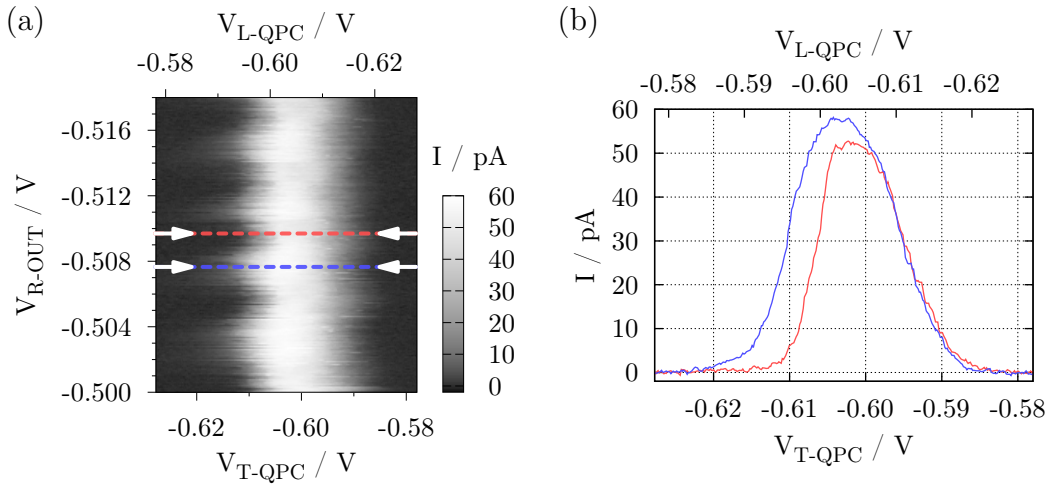


**Figure 4.3:** QDR current while probing the central region with the gate ‘R-OUT’. Along the  $x$ -axes the gates ‘L-QPC’ and ‘T-QPC’ are changed simultaneously so as to pass through the middle of a conduction point.  $T_l = 41$  mK,  $T_e = (89 \pm 11)$  mK. (b) Two example line-scans taken from the data in (a) at the positions indicated by the red and blue dotted lines.

The simple model for the QDR current shown in Figure 4.1 assumes that the electrochemical potential of the centre ( $\mu_C$ ) lies half way between the potentials of the source and drain. While there is no way to measure  $\mu_C$  directly, it can be probed using nearby gates. Figure 4.3 shows the effect of changing  $\mu_C$  on the line-shape of current through the centre of a conduction point. As expected, the right side of the peak changes little, but the width and position of the left side are seen to oscillate. The period of the oscillations matches the previously observed period of Coulomb blockade oscillations in the centre (see Figure 3.14), and they are therefore attributed to the movement of successive charge states through the bias window. Therefore, the energy levels of the device will resemble the simplified picture shown in Figure 4.1(a) once each period.

Measurements were made at several different mixing chamber temperatures in the range of 50 mK – 200 mK. The tuning of the gate voltages and the general stability of the device were often found to change significantly with temperature. Having chosen a conduction point to investigate at each temperature, non-linear measurements of the corresponding Coulomb blockade peaks in both dots were made. These measurements were used to determine the equilibrium electron temperature, as described in Section 3.5, and also to verify that the energies of the excited states in both dots were greater than  $eV_{SD}$ . Measurements similar to those

shown in Figures 4.2 and 4.3 were then made to record the current across the conduction point and many diagonal scans through its centre.

## 4.2 Simple QDR model

The measurements described in the previous section were first compared to a prediction of the QDR current in the limit of a constant temperature of the central region. Electrostatic coupling between the dots and the central 2DEG was also initially neglected. The derivation of this model and the comparison with the data are detailed in this section.

### 4.2.1 Master equation

We use the orthodox theory of single-electron tunnelling [36, 37, 123] to calculate the current through the device. The fundamental assumptions are that the system is Markovian and that the time between tunnelling events is much longer than their duration.<sup>1</sup> Second order processes such as co-tunnelling are neglected. The behaviour of the system is therefore reduced to transitions between well defined states via single stochastic tunnelling events. This approach can be used to find either typical time-dependent results or long-time-average results. As the measurements of our system are made on much longer time scales than the tunnelling events, we choose the latter.

A master equation describes the time evolution of the occupation probabilities of the different states of a system. The QDR is modelled as three charge islands (the two dots and the central region) in series, and the states of the system correspond to the combinations of charge occupancies on these islands. For an individual state  $i$ , the time evolution of its occupation probability ( $p_i$ ) is given by:

$$\dot{p}_i = \sum_{j \neq i} p_j \Gamma_{ji} - p_i \sum_{j \neq i} \Gamma_{ij} \quad (4.1)$$

where  $\Gamma_{ij}$  is the transition rate from the state  $i$  to the state  $j$ . The first term is the total inward flow of probability density to the state  $i$ , and the second term is the total outward flow. A master equation is formed by combining similar expressions

---

<sup>1</sup>The duration of tunnelling events in is expected to be  $\sim$  ps [124].

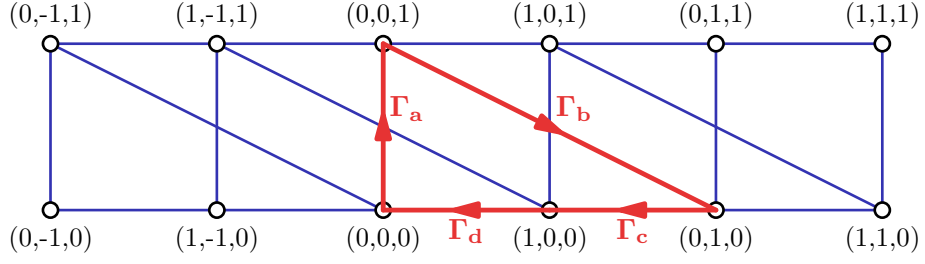


**Figure 4.4:** Allowed transitions between QDR charge states. For a state  $(l, m, n)$ , the charge in dot B is  $el$ , the charge in the central region is  $em$ , and the charge in dot A is  $en$ .

for all  $N$  possible states:

$$\begin{pmatrix} \dot{p}_1 \\ \dot{p}_2 \\ \vdots \\ \dot{p}_N \end{pmatrix} = \begin{pmatrix} -\Gamma_1 & \Gamma_{21} & \cdots & \Gamma_{N1} \\ \Gamma_{12} & -\Gamma_2 & \cdots & \Gamma_{N2} \\ \vdots & \vdots & \ddots & \vdots \\ \Gamma_{1N} & \Gamma_{2N} & \cdots & -\Gamma_N \end{pmatrix} \begin{pmatrix} p_1 \\ p_2 \\ \vdots \\ p_N \end{pmatrix} \Rightarrow \frac{d}{dt}(\underline{p}) = \underline{\Gamma} \underline{p} \quad (4.2)$$

where  $\Gamma_i = \sum_{j \neq i} \Gamma_{ij}$ . The steady-state solution for  $\underline{p}$  can then be found by solving the equation  $\underline{\Gamma} \underline{p} = \underline{0}$ , subject to the condition  $\sum_i p_i = 1$ . Given the matrix  $\underline{\Gamma}$ , this can be solved either numerically [125] or, in simple cases, analytically.

Once the steady-state value of  $\underline{p}$  is known, the long-time-average of the current through the system can be found. For each transition there is an associated movement of charge: if  $q_{ij}^D$  ( $q_{ij}^S$ ) is the charge moved to the drain (source) during the transition from state  $i$  to  $j$ , the average current from source to drain is given by:

$$I = \sum_i \sum_{j \neq i} p_i \Gamma_{ij} q_{ij}^D = - \sum_i \sum_{j \neq i} p_i \Gamma_{ij} q_{ij}^S \quad (4.3)$$

To calculate the current we must fully define the matrix  $\underline{\Gamma}$  by identifying all the allowed transitions in the system and calculating their rates. Figure 4.4 shows the possible system states when dots A and B can hold either 0 or 1 excess electrons and the central region can hold -1, 0 or 1. The blue lines show the allowed transitions between states, which correspond to the movement of a single electron between adjacent charge islands or to one of the reservoirs. The four transitions highlighted in red in Figure 4.4 indicate an example of a cyclic path, moving around which results in the net transfer of a single charge from the source to the drain.

Individual transition rates are calculated assuming that dots A and B both

have symmetric tunnel barriers with energy-independent tunnel rates of  $\Gamma_0$ . The spectra of states for the dots are modelled as just a single infinitely narrow state. This assumes that the lifetime broadening of dot states ( $\hbar\Gamma_{total}$ ) is less than  $k_B T_e$ .

The system must be Markovian, which means that the distribution of occupied states in the central region must be independent of the history of the system. We assume that it is always given by a Fermi distribution, implying that the scattering of carriers, and hence the re-equilibration of the central 2DEG, is fast compared to the frequency of tunnelling events.

From these simplifications, the tunnel rates highlighted in Figure 4.4 (and, similarly, all other transition rates) can be found by considering the probability of finding empty (full) states at the appropriate energies for an electron to enter (leave) one of the three 2DEGs:

$$\Gamma_a = \Gamma_0 \left[ f_S \left( \mu_A^f - \mu_S \right) \right] \quad (4.4)$$

$$\Gamma_b = \Gamma_0 \left[ 1 - f_C \left( \mu_A^i - \mu_C^f \right) \right] \quad (4.5)$$

$$\Gamma_c = \Gamma_0 \left[ f_C \left( \mu_B^f - \mu_C^i \right) \right] \quad (4.6)$$

$$\Gamma_d = \Gamma_0 \left[ 1 - f_D \left( \mu_B^i - \mu_D \right) \right] \quad (4.7)$$

where  $f_S$ ,  $f_C$  and  $f_D$  are Fermi functions ( $f(x) = [1 + \exp(x/w)]^{-1}$ ) with widths ( $w$ ) given by the thermal broadening of the source, center and drain 2DEGs respectively. The electrochemical potentials of the dots A and B ( $\mu_A$  and  $\mu_B$ ) and of the central region ( $\mu_C$ ) depend on the charge state of the system. The superscript ‘ $i$ ’ or ‘ $f$ ’ indicates whether these values apply to the initial or final state. Here we limit the charge occupancy of the dots to either 0 or 1 excess electrons, and use the following simple forms for  $\mu_A$  and  $\mu_B$ :

$$\mu_A(n) = \left[ (n-1)e^2 - eC_G V_A \right] / C_\Sigma \quad (4.8)$$

$$\mu_B(l) = \left[ (l-1)e^2 - eC_G V_B \right] / C_\Sigma \quad (4.9)$$

Both dots are assumed to have the same total capacitance ( $C_\Sigma$ ), and the same capacitance to their respective gate electrodes ( $C_G$ ). These expressions imply that the electrochemical potentials increase by one charging energy ( $e^2/C_\Sigma$ ) per electron added to the dot, and scale linearly with gate voltage according to the correct lever-

arm ( $C_G/C_\Sigma$ ). A similar expression is used for  $\mu_C$ :

$$\mu_C(m) = [(m-1)e^2 - eC_{CG}V_C] / C_{C\Sigma} \quad (4.10)$$

The expressions 4.8—4.10 are correct only to within a constant offset, but this is acceptable, provided that only differences in gate voltages are considered.

### 4.2.2 Predictions

Figure 4.5 shows the current through the system calculated using the method detailed in the previous section. The master equation is solved numerically [125] with 10 allowed charge states in the center region. Both plots show the line-shape of the current as the two dots energies are moved simultaneously in opposite directions by changing the gate voltages  $V_A$  and  $V_B$ . The results confirm the prediction from Figure 4.1: that the width of the left hand side of the peak is determined by  $T_C$ , and the right hand side by  $T_e$ .

There are two obvious reasons why the model might fail to describe the data well. Firstly, it assumes a constant  $T_C$ . If  $T_C$  actually varies significantly, then the shape of the left side of peaks in current will not fit the model well for any  $T_C$ . Secondly, by neglecting capacitive coupling between the charge islands we have greatly limited the number and complexity of charge-transporting processes in the system. For example, moving around the red loop in Figure 4.4 is essentially identical to moving around the same loop shifted one place to the right. In both cases electrons move between the islands at the same energies (because  $\mu_B$  does not depend on  $m$  and  $n$ , etc.), the only difference is that the tunnelling events happen in a different order. However, if coupling between the islands is included then the degeneracy of the various energies is lifted and the two loops become distinct. They will switch on and off at different gate voltages and conduct over different gate voltage ranges. This will result in transport occurring over a larger range of gate voltages than expected.

When fitting the model to the data, the presence of numerous charge transporting processes can be accounted for in a simplistic fashion by allowing the peaks in current to have arbitrary widths. The line-shapes of both sides of a peak are still found from the model described above, but the two sides are calculated independently and can be centred on different voltages. A constant current is assumed between the sides. The justification for this approach is that while many compet-

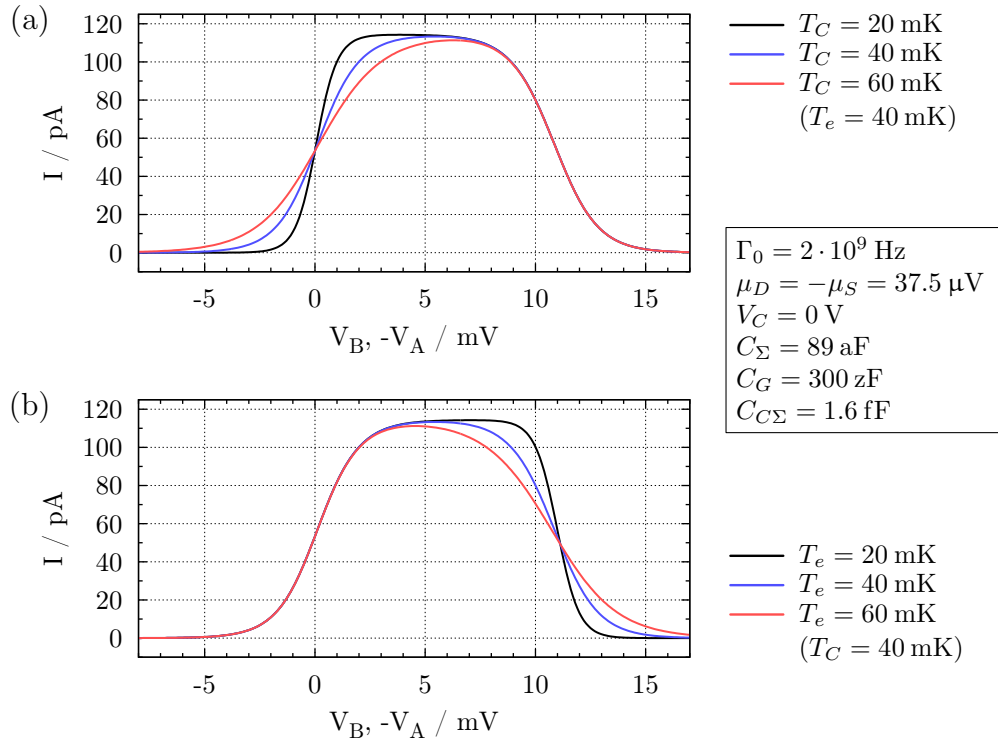


**Figure 4.5:** Predicted drain to source current (electron flow from source to drain) as the two dot energies are simultaneously moved in opposite directions. In (a), the sharpness of the left side of the peak is shown to be determined by the temperature in the centre ( $T_C$ ). In (b), the sharpness of the right side is shown to be determined by the temperature of the reservoirs ( $T_e$ ).

ing transport processes may exist, the switch-on and off of current at the sides will likely be dominated by single processes only — there will always be one process which is the first to switch on, and one which is the last to switch off.

To increase the speed of calculating the current, analytic solutions to the QDR master equation were found in two limiting cases. In the first case,  $\mu_A(1) \approx \mu_S$ ,  $\mu_B(1) \approx \mu_D$ , and both are far (several  $k_B T_C$ ) from  $\mu_C(1)$ . This is the situation at the switch-on of current when the dot energies pass the source and drain reservoirs. In the second case,  $\mu_A(1) \approx \mu_B(1) \approx \mu_C(1)$ , and all three energies are far (several  $k_B T_e$ ) from  $\mu_S$  and  $\mu_D$ . This is the situation at the switch-off of current when the dot energies pass each other. In both situations the bias is symmetric ( $\mu_S = -\mu_D$ ), and the central region energy is assumed to lie mid-way between the reservoirs ( $\mu_C(1) = 0$ ). As usual, it is also assumed that the two dots are being probed simultaneously in opposite directions ( $V_B = -V_A$ ).

The two analytic solutions of the master equation, with three allowed central region charge states, lead to two expressions for the line-shapes of the left and right sides of a peak in current. An approximation to the total current over the whole peak ( $I$ ) is found by combining them:

$$I_{RHS} = e\Gamma_0 \left[ \frac{2f_R^2 + 3f_R}{2f_R + 12} \right] \quad (4.11)$$

$$I_{LHS} = e\Gamma_0 \left[ \frac{2f_C^2 - 7f_C + 5}{4f_C^2 - 6f_C + 14} \right] \quad (4.12)$$

$$I = I_{LHS} + I_{RHS} - \frac{5}{14}e\Gamma_0 \quad (4.13)$$

In these expressions ‘ $f_R$ ’ and ‘ $f_C$ ’ are Fermi functions of  $V_B (= -V_A)$ :  $f_{R,C}(V_B) = [1 + \exp((V_B - V_{R,C}^0)/w_{R,C})]^{-1}$ . The width ( $w_R$ ) of ‘ $f_R$ ’ is proportional to the thermal broadening of the reservoirs, and the width ( $w_C$ ) of ‘ $f_C$ ’ is proportional to the thermal broadening of the centre. The constants of proportionality are the lever-arms that convert changes in each dot’s energy to changes in gate voltage. Both  $I_{LHS}$  and  $I_{RHS}$  are broadened step functions with a step height of  $(5/14)e\Gamma_0$ . To make  $I$  be a top-hat-like function, with  $I = 0$  at  $V_B \rightarrow \pm\infty$ , a constant term equal to the step height must be subtracted from the sum of  $I_{LHS}$  and  $I_{RHS}$ . The position and width of the peak in  $I$  is set by shifting  $I_{LHS}$  (via  $V_C^0$ ) and  $I_{RHS}$  (via  $V_R^0$ ). The analytic and numerical solutions are found to be in good agreement for  $k_B T_{e,C} \ll |\mu_S - \mu_D|$ , with the analytic solution being far more efficient to calculate.

The analytic form for the current is also found to be a satisfactory approximation

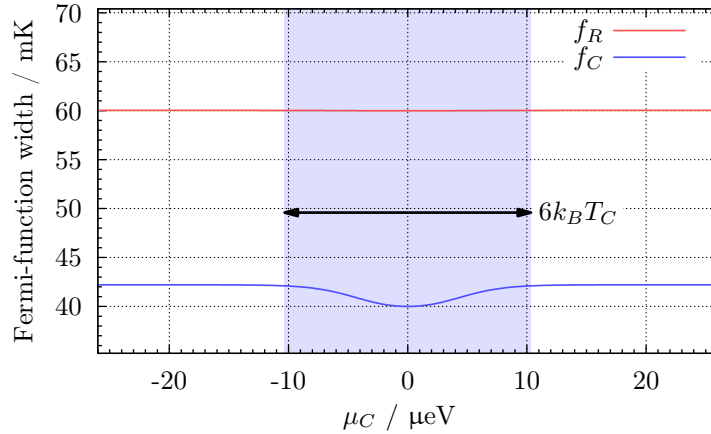


**Figure 4.6:** Widths of  $f_R$  and  $f_C$  found by fitting Equation 4.13 to the current given by the full master equation. The fits are good over the whole range of  $\mu_C$ , and the widths found at  $\mu_C = 0$  are exactly correct. ( $T_C = 40$  mK and  $T_e = 60$  mK.) However, once  $\mu_C$  has moved significantly away from zero, fitting to the left side of the peak over-estimates the central region temperature by approximately 5%.

when  $\mu_C \neq 0$ . Given that the range of dot energies over which conduction can occur is largest when  $\mu_C(1)$  lies mid-way between the source and drain, the primary effect of changing  $\mu_C$  (via the voltage  $V_C$ ) is to reduce the width of the peak in current. This is already taken into account by allowing  $f_R$  and  $f_C$  to be centred at different points. A secondary effect is that the line-shape of the left side of the peak deviates slightly from Equation 4.12. Figure 4.6 shows that this difference results only in a marginal *over*-estimation of the central region temperature.

### 4.2.3 Analysis

The analytic expression for the QDR current (Equation 4.13) was fitted to various measurements of current through the middle of conduction points. The fitting parameters were  $\Gamma_0$  (which determines the peak height), and the widths and positions of  $f_R$  and  $f_C$ . Figure 4.7 shows six example fits for data taken at various temperatures.

The results in Figure 4.7(b) and (e) are examples of where many repeated measurements have been averaged to reduce the noise in the current. For the highest temperature data [Figure 4.7(f)] the data was averaged as  $\mu_C$  was changed over a range approximately equal to one charging energy of the central region. This was done because at this temperature the Coulomb blockade of the centre

was not visible (in contrast to e.g. Figure 4.3). It would therefore be impossible to determine  $\mu_C$  from the data, and averaging over a single charging period was the only way to eliminate it as an unknown parameter. (This is discussed in more detail in Section 4.3.5.)

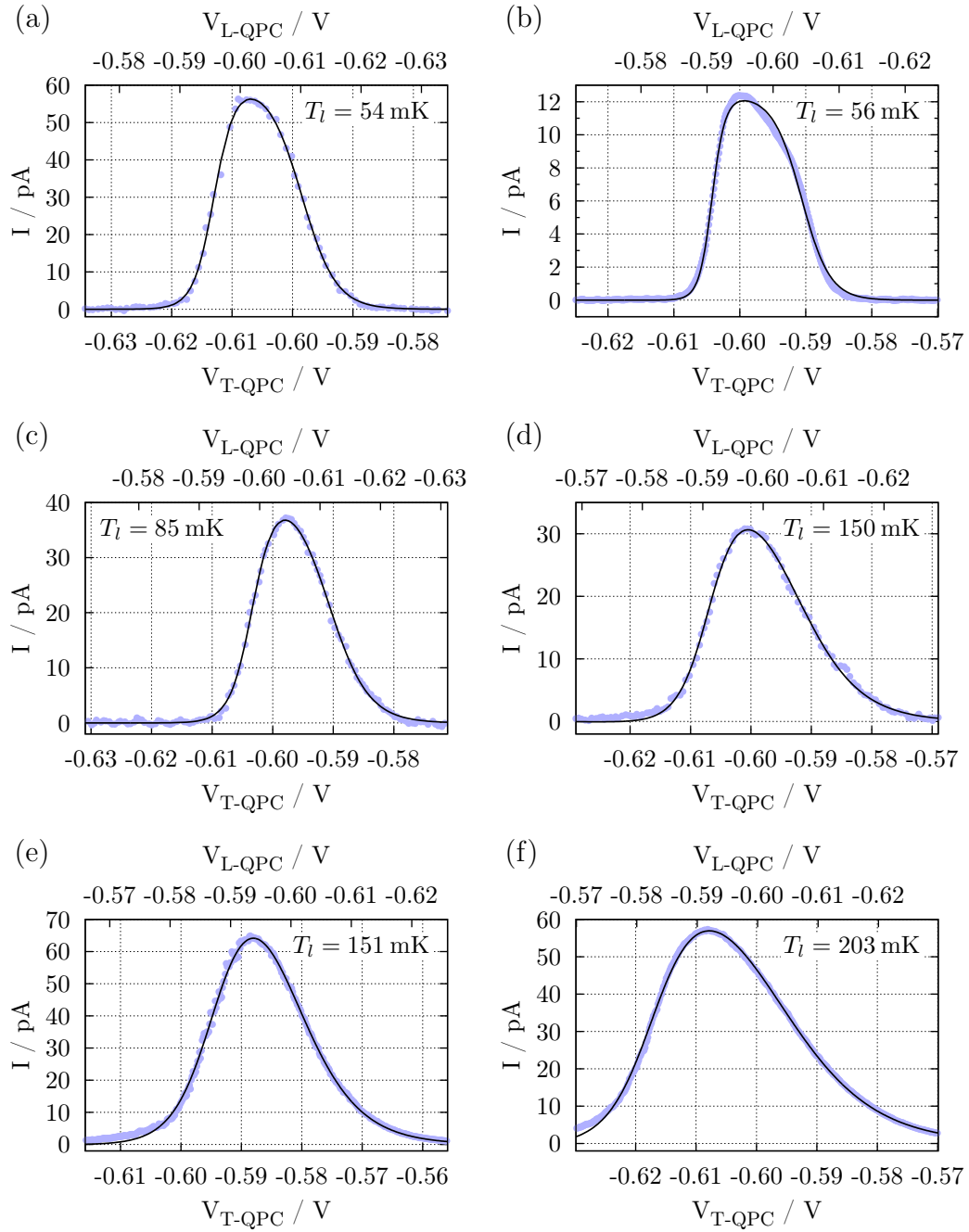
Of the six measurements in Figure 4.7, the worst fit is found in plot (b). Here the prediction clearly deviates systematically from the data. (A possible explanation for this is given in Section 4.3.5.) There is some suggestion of a similar deviation in the centre of the peak in Figure 4.7(a), but the data is too noisy to be conclusive. At higher temperatures [Figure 4.7(c)–(f)] the predicted current is found to fit the data very well on the right hand side of the peak. In Figure 4.7(d)–(f) there are small systematic deviations on the left hand side of the peaks.

Most measurements were actually made in sets that consisted of repeated scans through the centre of a conduction point while stepping  $V_C$  to probe the Coulomb blockade of the central region. An example of fitting to such a data set is given in Figure 4.8. From Figure 4.8(b) average widths, in gate voltage, for  $f_C$  and  $f_R$  and standard deviations for each can be found.

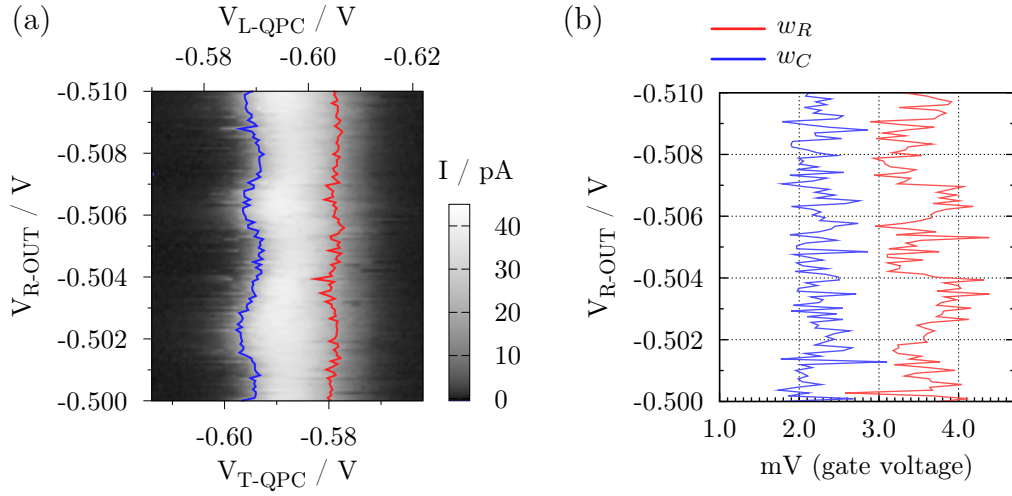
The most striking feature of the measurements is that line-scans were often observed to have a significant asymmetry, with the left side always being sharper than the right. Within the model developed in the preceding section, this implies that the central region must be at a lower temperature than the external reservoirs. This would be expected for a successfully working QDR. To gain an overview of how frequently asymmetric peaks were seen, the analytic expression for the QDR current was fitted to all available data sets.<sup>2</sup>

Figure 4.9 shows the average fitted widths, in gate voltage, of  $f_R$  and  $f_C$  found from all available data sets in the manner shown in Figure 4.8. In general,  $w_R$  follows fairly closely the widths observed in measurements of the equilibrium electron temperature. This is expected since both should be equal to the thermal broadening in the source and drain reservoirs, multiplied by similar lever-arms. Figure 4.9 shows the approximate thermal broadening (in mK) corresponding to different widths in gate voltage, using the lever-arm found for the left dot as a conversion factor (see Section 3.5). The validity of relating these temperatures to the fitted values of  $w_R$  and  $w_C$  would be limited if the gate capacitances for the two dots are unequal, or if capacitances between dot B(A) and the gate for dot A(B) are non-zero. Both would modify the lever-arm for measurements of the full

<sup>2</sup>Measurements were only discarded due to poor device stability.



**Figure 4.7:** (a)-(f) Fits of the analytic form for the QDR current (black lines) to measurements (blue circles) at various mixing chamber temperatures. Each line-scan is taken through the centre of a conduction point. (a), (c) and (d) are the same data as shown in Figure 4.2. (b) and (e) are averages of many identical sweeps, to reduce noise. (f) is the average of many sweeps as only  $V_C$  is varied.



**Figure 4.8:** (a) Measured current through the centre of a conduction point ( $x$ -axis) as  $V_C$  is stepped. Overlaid is the fitted position of  $f_R$  (red line) and  $f_C$  (blue line). The fluctuations in the position of  $f_C$  are due to Coulomb blockade in the central region. (b) Fitted widths of  $f_R$  and  $f_C$ . [ $T_l = 84$  mK,  $T_e = (140 \pm 13)$  mK]

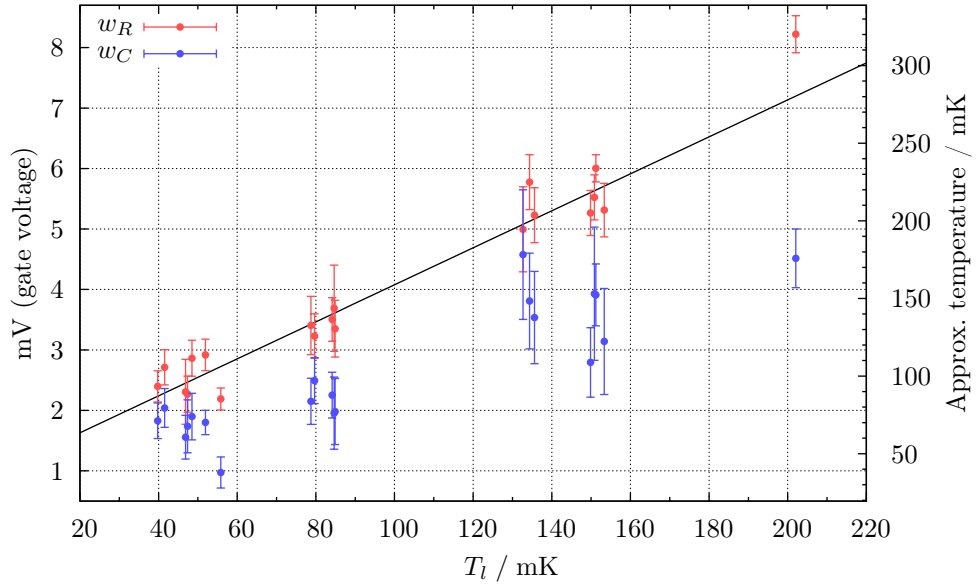


**Figure 4.9:** Average fitted widths of  $f_R$  and  $f_C$  for various data sets. (The bars show the standard deviation.) The black line is a best fit to the Fermi-function widths from separate measurements of the equilibrium electron temperature. To approximately relate widths in gate voltage to temperatures, the lever-arm found for the left dot is used (see Section 3.5).

device, compared to just a single dot, but neither are expected to be large.

The average widths of  $f_C$  vary more widely than those of  $f_R$ . This would be expected for a working QDR since the amount of cooling the device achieves depends on its detailed setup, which was not well controlled during the experiment. However, the average width of  $f_C$  was found to always be less than that of  $f_R$ .

All of the trends observed in Figure 4.9 are consistent with a working QDR. An alternative explanation could be that the central region, once isolated, becomes fixed to the lattice temperature of the device. This seems unlikely given the large spread in the widths of  $f_C$ . (We might expect a trend at least as clear as that in the widths of  $f_R$ .) Furthermore, the most obvious explanation for the systematic deviations between data and predictions observed on the left hand sides of the peaks in Figure 4.7 is that the temperature of the central region is not actually constant over the whole peak.

Another possible reason for this analysis to be invalid is that the density of occupied states in the central region may be being driven away from equilibrium. In this situation the model no longer provides a good description of the system. Following the argument in Section 3.1.1, we calculate the maximum rate of injection into one central region state as the total rate of injection ( $\approx I/e$ ), divided by the number of central region states in the energy range of the lifetime-broadened state of the injecting dot. However, whereas we previously assumed that  $\Gamma_0 \approx 2I/e$ , Equations 4.11 and 4.12 now show that  $\Gamma_0 = (14/5e)I$  (assuming symmetric and identical dots). The injection rate ( $1/\tau_{in}$ ) is therefore given by:

$$\frac{1}{\tau_{in}} = \frac{5}{14} \left( \frac{\pi \hbar}{2m^*} \right) \frac{1}{A} \Rightarrow \tau_{in} \approx 6 \text{ ns} \quad (4.14)$$

From Equation 2.14, we find that this rate is exceeded by the rate of large-energy-transfer electron-electron scattering only for  $T_e > 175$  mK. This suggests that we may be close to the cross-over into the out-of-equilibrium regime. However, in calculating  $\tau_{in}$  we have assumed that the current is at its maximum value, while in comparing it to Equation 2.14 we have assumed that the carriers are being injected close to the Fermi energy of the central region. This is never the case and Figure 4.5 shows that, when injecting close to the Fermi energy, the current will roughly be halved ( $\tau_{in}$  will double). Asymmetric tunnel barriers in the dots can increase lifetime broadening without increasing the current, also pushing the crossover to lower temperatures. It therefore seems very unlikely that the central

region is in quasi-equilibrium above 120 mK (the cross-over for  $\tau_{in} = 12$  ns).

In conclusion, this preliminary analysis found the line-shapes of current through the device to be quite well described by a simple prediction based on the theory of single-electron tunnelling and assuming constant temperatures in all three 2DEGs. The observation of significantly asymmetric peaks in current implies that, if this theory is valid, the central region of the device must routinely be at a lower temperature than the reservoirs. However, this treatment offers no physical mechanism for the temperature difference and, since complications due to electrostatic coupling are neglected, it certainly does not provide a complete model for current flow through the device. To address these issues and gain a better understanding, a more complete model was developed. This is detailed in the following section.

### 4.3 Full QDR model

Developing a more realistic model to describe the measured device requires the inclusion of two important effects: electrostatic interactions between the charge islands and a changing  $T_C$  caused by the net heating or cooling effect of current through the device. Once these are taken into account it should be possible to answer the questions of whether a QDR can still cool a 2DEG with a small capacitance, and whether the behaviour of our device is consistent with such cooling being achieved.

#### 4.3.1 Electrostatics

The standard technique for modelling electrostatic interactions in coupled quantum dot systems is to use an equivalent capacitor network. This has proved successful in predicting charge-stability diagrams for double-dots [126, 127, 29], triple dots [128, 129, 130], and can in principle be generalised to any number of dots [123]. Following the work on triple dots, we define an equivalent capacitor network for a QDR-like device, which is shown in Figure 4.10.

We define the following quantities: The components of the vector  $\underline{q}$  are the charges on each node in the capacitor network and the components of the vector  $\underline{v}$  are the voltages of each node.  $\mathbf{C}$  is the matrix of capacitances, where off-diagonal elements  $-\mathbf{C}_{ij}$  are the capacitance between the nodes  $i$  and  $j$ , and diagonal elements  $\mathbf{C}_{ii}$  are the total capacitance of the node  $i$ . Given these definitions, it can be shown that  $\underline{q} = \mathbf{C}\underline{v}$ .

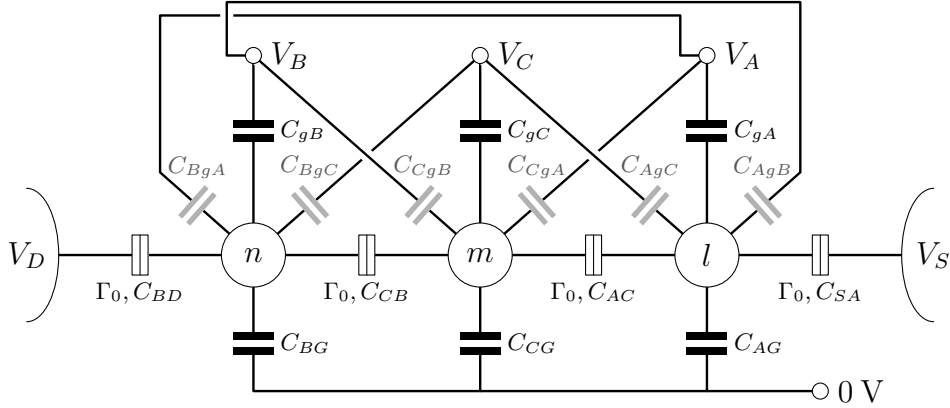


**Figure 4.10:** Capacitor network for three gated charge islands in series. The charges on the three islands are  $-el$ ,  $-em$  and  $-en$ . The tunnel junctions (denoted by a rectangle with a line through the centre) each have an associated capacitance and tunnel rate. Capacitors shown in grey account for cross-coupling effects and are, in general, relatively small.

Two types of nodes form the network in Figure 4.10: those for which the voltage is known (“voltage nodes”) and those for which the charge is known (“charge nodes”). We subdivide  $\underline{q}$ ,  $\underline{v}$  and  $\mathbf{C}$  to allow the two to be considered separately:

$$\begin{pmatrix} \underline{q}^c \\ \underline{q}^v \end{pmatrix} = \begin{pmatrix} \mathbf{C}^{cc} & \mathbf{C}^{cv} \\ \mathbf{C}^{vc} & \mathbf{C}^{vv} \end{pmatrix} \begin{pmatrix} \underline{v}^c \\ \underline{v}^v \end{pmatrix} \quad (4.15)$$

where  $\underline{q}^c$  ( $\underline{v}^c$ ) is the charge (voltage) on the charge nodes and  $\underline{q}^v$  ( $\underline{v}^v$ ) is the charge (voltage) on the voltage nodes. From the above expression we can define the voltage on the charge nodes in terms of known properties of the capacitor network:

$$\underline{v}^c = (\mathbf{C}^{cc})^{-1}(\underline{q}^c - \mathbf{C}^{cv}\underline{v}^v) \quad (4.16)$$

When producing charge stability diagrams from a capacitor network it is usual to consider the free energy. However, Wasshuber [123] points out that this is not necessary for modelling single-electron tunnelling events. The probability of a given transition depends only on the voltage difference across the tunnel barrier in question, plus a charge-state independent term. Therefore, simply using the difference in voltages between the nodes of the capacitor network is acceptable, and Equation 4.16 provides all the necessary information about the electrostatic interactions in the system.

Following the argument of Wasshuber [123], we define the changes in electrostatic energy due to a single electron tunnelling from a voltage node to a charge node ( $\Delta U_{V \rightarrow C}$ ), from a charge node to a voltage node ( $\Delta U_{C \rightarrow V}$ ), and from a charge node to a charge node ( $\Delta U_{C \rightarrow C}$ ):

$$\Delta U_{V \rightarrow C} = -e(\underline{v}_j^c - \underline{v}_i^v) + [(\mathbf{C}^{cc})_{jj}^{-1}] e^2/2 \quad (4.17)$$

$$\Delta U_{C \rightarrow V} = -e(\underline{v}_j^v - \underline{v}_i^c) + [(\mathbf{C}^{cc})_{ii}^{-1}] e^2/2 \quad (4.18)$$

$$\Delta U_{C \rightarrow C} = -e(\underline{v}_j^c - \underline{v}_i^c) + [(\mathbf{C}^{cc})_{ii}^{-1} + (\mathbf{C}^{cc})_{jj}^{-1} - 2(\mathbf{C}^{cc})_{ij}^{-1}] e^2/2 \quad (4.19)$$

where  $i$  and  $j$  are the indices of the initial and final nodes.  $[(\mathbf{C}^{cc})_{ij}^{-1}]$  is the  $ij^{\text{th}}$  element of the inverse of the matrix  $\mathbf{C}^{cc}$ .] The voltages are calculated *before* the tunnelling event for both nodes.

To incorporate the predictions of the capacitor network into the master equation, the expressions for the tunnel rates between the charge states of the system (e.g. Equations 4.4–4.7) are modified by replacing the arguments of the Fermi functions with the appropriate changes in electrostatic energy. Essentially, we require that any excess (deficit) of energy associated with a tunnelling event must be absorbed (provided) by one of the three electron gases. For example, the rates  $\Gamma_a$  (for tunnelling from the source to dot A), and  $\Gamma_b$  (for tunnelling from dot A to the central region), previously defined by Equations 4.4 and 4.5, are now given by:

$$\Gamma_a = \Gamma_0 f_S(\Delta U_a) \quad (4.20)$$

$$\Gamma_b = \Gamma_0 [1 - f_C(-\Delta U_b)] = \Gamma_0 f_C(\Delta U_b) \quad (4.21)$$

where  $\Delta U_a$  is calculated using Equation 4.17, and  $\Delta U_b$  is calculated using Equation 4.19. With  $\mathbf{\Gamma}$  fully defined using the capacitor network, we have confirmed that the predicted current is equivalent to that found using the simpler model detailed in Section 4.2, if neither back-action or cross-coupling of gates are included.

The success of the capacitor network in describing the measurements can most readily be seen in the large bias regime. In Figure 4.11, the current through the device under biases of 0.5 mV and 0.3 mV is shown to be reproduced accurately by the model, including the unexpected trapezoidal shape of the conduction points. Figures 4.12 and 4.13 illustrate that the origin of this shape is the capacitive coupling between the dots and the central region, and therefore cannot be predicted by the simpler model.

For the simulations shown in Figures 4.11–4.13, the capacitances used to fill the

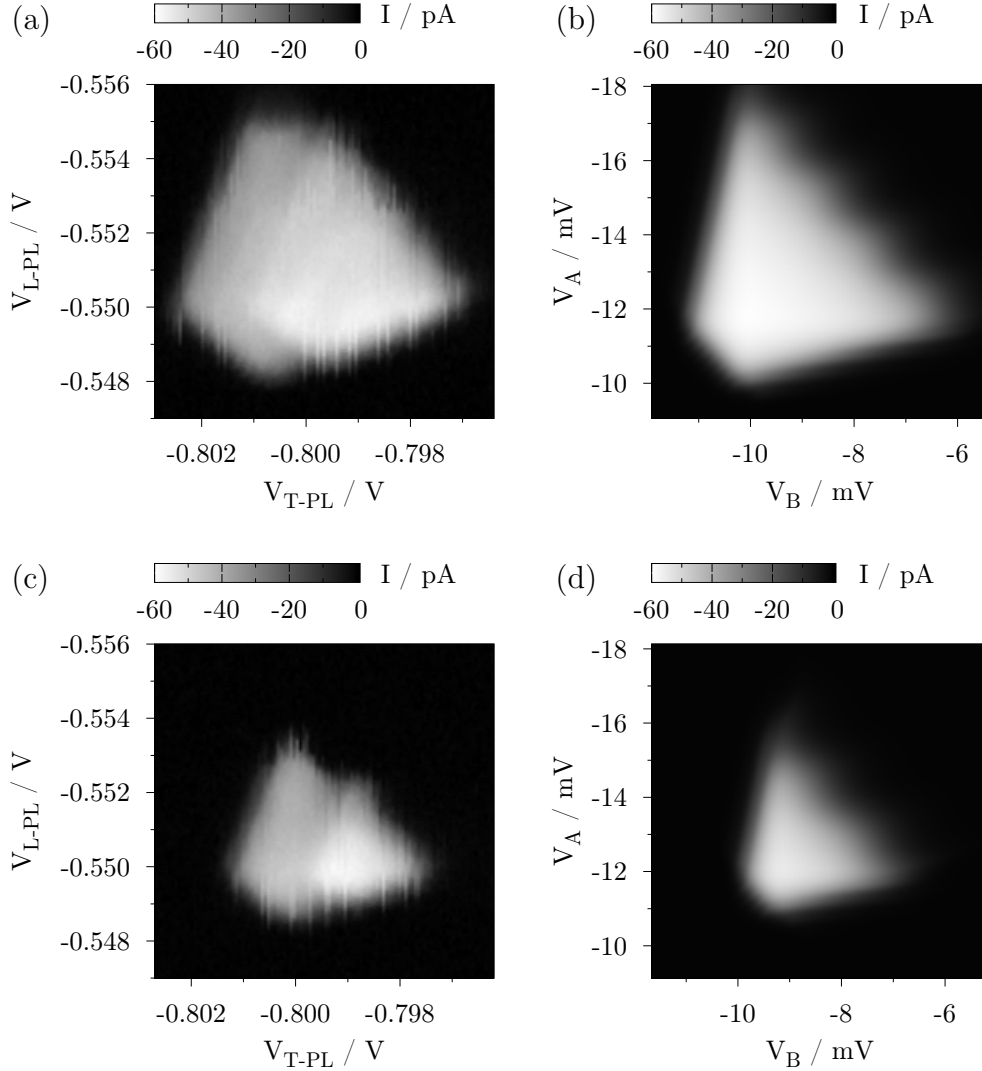


**Figure 4.11:** (a) and (c) are the measured QDR current under biases of  $-500 \mu\text{V}$  and  $-300 \mu\text{V}$  respectively at  $T_e \approx 90 \text{ mK}$ . (b) and (d) are the predicted current under the same biases. The extra structure seen in the measured data is due to an excited state in the top dot with an energy less than  $300 \mu\text{eV}$ . In these simulations the source and drain temperature ( $T_e$ ) is set to  $90 \text{ mK}$ , but the central region temperature ( $T_C$ ) is elevated to  $275 \text{ mK}$ . This is reasonable as significant heating of the centre is expected under large biases. If this effect is not included, the upper right side of the calculated conduction points show periodic modulations due to the Coulomb blockade of the central region.

matrix  $\mathbf{C}$  were determined by separate measurements of the two dots and the central region. Lever-arms (conversion factors between voltages and dot energies) are found from non-linear measurements of the two dots: for the gate electrode voltages we find  $\alpha_G^T = 0.081$  eV/V and  $\alpha_G^L = 0.053$  eV/V (the superscripts indicate the top (T) or left (L) dot of the device), which determine  $C_{gA}$  and  $C_{gB}$ ; for the drain's bias voltage we find  $\alpha_D^T = 0.29$  eV/V and  $\alpha_D^L = 0.20$  eV/V, which determine  $C_{BD}$  and  $C_{AC}$ . The source was not biased, and so we must deduce  $C_{CB}$  and  $C_{SA}$  by assuming that  $\alpha_S^T = \alpha_D^L$  and  $\alpha_S^L = \alpha_D^T$  (from the lithographic symmetry of the device). Non-linear measurements of the central region show its charging energy to be 100  $\mu$ eV, giving  $C_{CT}$ . (The determination of the central region charging energy is discussed in more detail in Section 4.3.4.) The lever-arm for probing the central region with 'L-PL' is found to be 0.091 eV/V, and we assume the same lever-arm for 'T-PL'. These determine  $C_{CgA}$  and  $C_{CgB}$ . The voltage  $V_C$  remains constant throughout the simulations, and so the capacitances  $C_{gC}$ ,  $C_{AgC}$  and  $C_{BgC}$  are unimportant. The cross-couplings due to  $C_{AgB}$  and  $C_{BgA}$  were neglected because of lack of a suitable calibration measurement. However, these capacitances are expected to be the smallest in the system and to have little effect.

Using the values above, the capacitance model reproduces the measured shapes of both conduction points in Figure 4.11; however, the calculated points are slightly too small in both the  $V_B$  and  $V_A$  dimensions. Closer agreement is found if both  $C_{gA}$  and  $C_{gB}$  are increased by 25%. This discrepancy probably arises from the fact that no data was available to determine the lever-arms  $\alpha_G^R$  and  $\alpha_G^L$  for the specific tunings used in the measurements. It is therefore not surprising that some adjustment is necessary. The overall good agreement between the shape of the measured and predicted conduction points is a strong indication that the capacitor network is accurately modelling the behaviour of the device.

Further evidence of the validity of the capacitor network is that it predicts the back-action of the dot charges on the central region energy to be approximately 20% of the central region charging energy. This compares well with the measured value of 24%. The predicted value is determined only by the capacitances  $C_{AC}$ ,  $C_{CB}$  and  $C_{CT}$  which were found or inferred from independent measurements.

### 4.3.2 Thermal equilibrium

The final component of the full QDR model is a mechanism for predicting variation of the central region temperature ( $T_C$ ). Only by considering this can we answer the

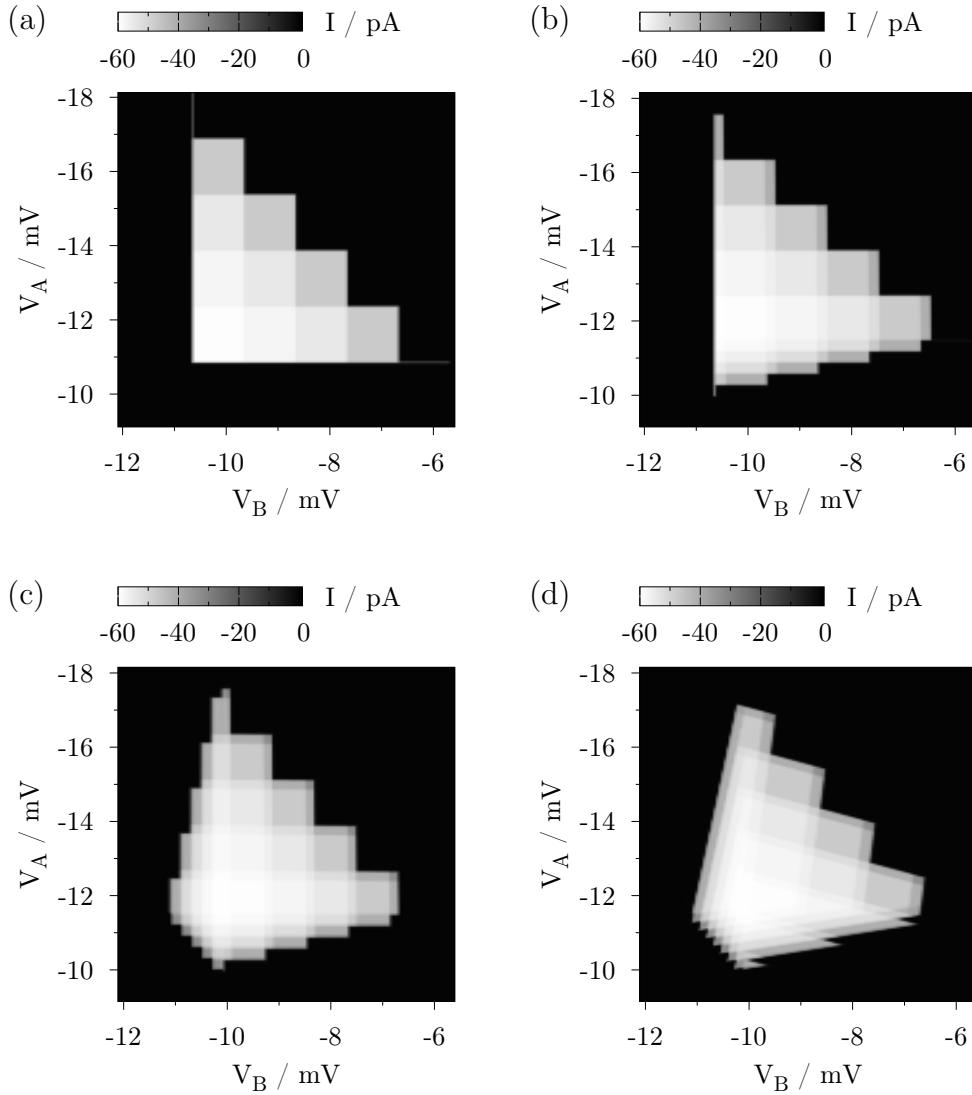


**Figure 4.12:** Calculated current with  $V_{SD} = -500 \mu\text{V}$  and  $T_e = T_C = 10 \text{ mK}$ . The low temperatures reveal the internal structure of this high-bias conduction point. In (a) no back-action or cross-coupling is included ( $C_{AC} = C_{CB} = C_{CgA} = C_{CgB} = 0$ ). The pattern of squares is due to multiple charge states of the central region lying within the bias window. (b) includes the back-action between dot A and the centre ( $C_{AC} \neq 0$ ). The charge on the centre now alters the energy of dot A. This can be seen along the bottom of the conduction point where the value of  $V_A$  at which transport stops depends on how far the centre can be charged. (c) also includes the back-action for dot B ( $C_{CB} \neq 0$ ), producing the same effect on the left side. Finally, (d) includes cross couplings ( $C_{CgA} = C_{CgB} \neq 0$ ). This skews the internal structure of the conduction point as the potential of the centre becomes coupled to  $V_A$  and  $V_B$ .

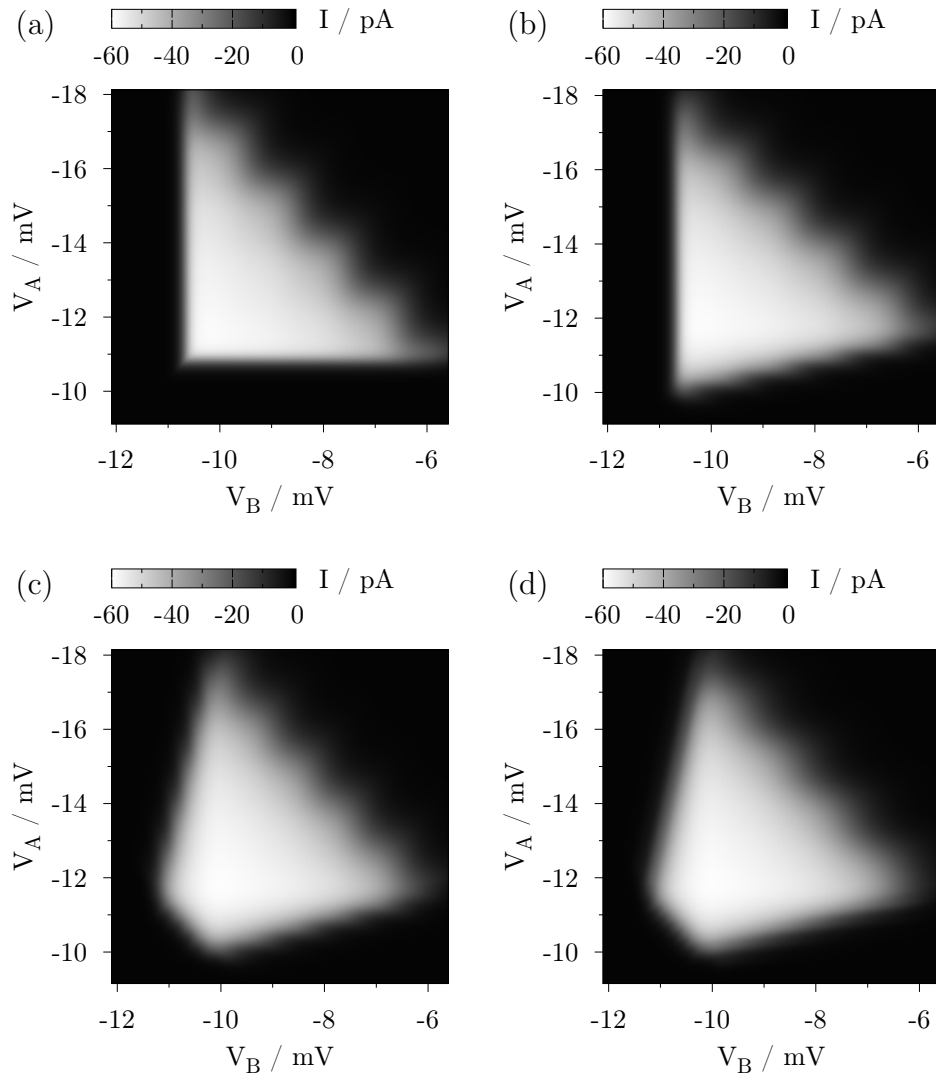


**Figure 4.13:** (a)—(d) are identical to the calculations in Figure 4.12(a)—(d), except with  $T_e = 90$  mK and  $T_C = 275$  mK. The internal structure of the conduction point now obscured by the thermal broadening of the three 2DEGs.

question of whether it is plausible for a QDR to function in the regime of strong electrostatic interactions and, if so, whether this provides an explanation for the observed results.

To find  $T_C$  for a particular configuration of the device we must take account of all the thermal processes which are expected to heat or cool the central 2DEG. The steady-state solution for  $T_C$  is the temperature for which the total heat flow into the centre is zero. In practice, the solution for  $T_C$  is found by simulating its time-dependent behaviour in response to the calculated heat flow. The solution is then said to be found once  $dT_C/dt < \gamma$ , where  $\gamma$  is some small threshold rate (typically 1 mK/s).

The method of heat-flow balancing has previously been used to successfully predict self-heating in metal SETs [131, 132, 133] and large semiconductor quantum dots [134, 135, 136], and cooling in superconducting refrigerators (see Section 2.5.1). Indeed, encouraging recent work on SINIS refrigerators has demonstrated successful cooling of a mesoscopic, Coulomb-blockaded metal island [137, 138]. In this work only one charge island is present and so electrostatic coupling in the system will not introduce multiple transport processes and unwanted heat leaks. Therefore, the question of whether a QDR like ours can cool a mesoscopic, Coulomb blockaded island is not resolved by this work.

Two processes are expected to dominate the flow of heat into and out of the central region: the current from the dots and the coupling of the 2DEG to the lattice via electron-phonon scattering. The latter was discussed previously in Section 2.3.2. Given the carrier density in the material, and the fact that the central 2DEG is approximately a 2.4  $\mu\text{m}$  wide square,<sup>3</sup> the heat flow due to electron-phonon coupling will be given by:

$$\dot{Q}_P \approx (230 \text{ fW K}^{-5})(T_e^5 - T_l^5) \quad (4.22)$$

The heat flow due to the current through the device ( $\dot{Q}_T$ ) depends on the energies and rates at which electrons are injected into and removed from the central region. Fortunately, in formulating the master equation we have already found everything needed to quantify this contribution. For 0D to 2D tunnelling, the heating or cooling of the 2D region associated with an individual tunnelling event is simply given by the change in electrostatic energy, as calculated by Equations 4.17–4.19. By analogy with Equation 4.3,  $dQ_{ij}^C$  is defined to be the energy imparted to the central 2DEG in tunnelling from charge state  $i$  to  $j$ . The total heat flow into

<sup>3</sup>This size assumes 100 nm of lateral depletion around the enclosing gates.

the centre due to charge transport can then be found from the transition rates ( $\Gamma$ ) and the steady-state solution for the occupation probabilities ( $p$ ):

$$\dot{Q}_T = \sum_i \sum_{j \neq i} p_i \Gamma_{ij} dQ_{ij}^C \quad (4.23)$$

In calculating  $\dot{Q}_T$  in this way we are approximating the states of the dots as delta functions with perfect energy selectivity. If the lifetime broadening of the dot states is less than  $k_B T_e$ , this approximation will be acceptable for determining the current. However, the contribution from infrequent off-resonance tunnelling can still be significant as these events can carry vastly different energies to on-resonance tunnelling. As discussed in Section 2.5.2, Edwards' original proposal found that tunnelling through the tails of the many lifetime-broadened states of the dots was a fundamental limitation of QDR performance.

It is not clear whether the inclusion of energy flow through lifetime-broadened dot states is fully compatible with the orthodox theory of single-electron tunnelling. While it is relatively simple to calculate the current in the presence of lifetime broadened dot states [123], allowing tunnelling away from resonance appears to necessarily violate either energy conservation or the Markovian nature of the system: the excess or deficit of energy must either be ignored or remembered. In the simple case of a single quantum dot, there is no need to remember the energy difference as its average does not depend on the history of the system. Thus Edwards was able to account for off-resonance tunnelling in a model where the two dots are essentially independent. However, it does not seem that generalising this to a system of three coupled charge islands is possible.

To include the effect of off-resonance tunnelling in the model, the following simplification is made: the net effect of the overlapping tails of multiple lifetime broadened dot states is approximated as an energy-independent background tunnelling probability. The electrical conductance of the tails is not expected to contribute significantly to the current and is disregarded. However, the thermal conductance is included as a third term in the heat balance by modelling it as being due to a pair of energy-independent tunnel barriers connecting the central region to the source and drain.

The thermal conductance of an energy-independent tunnel barrier should obey the Wiedemann-Franz law;  $\dot{Q} = -[L_0 \bar{T} G] \Delta T$ , where  $L_0 = (k_B^2 \pi^2 / 3e^2)$  is the Lorenz number,  $G$  is the electrical conductance of the barrier, and  $\bar{T}$  and  $\Delta T$  are the mean

and difference of the temperatures of the electron gases on either side. This has been confirmed in experiments on 1D wires [74, 79]. Alternatively, if the temperature difference across the barrier is zero but a bias voltage ( $V$ ) is applied, then the heat dissipated in each of the reservoirs is equal to half the Joule heating;  $\dot{Q} = GV^2/2$ .

To calculate the heat flow into a thermally isolated region connected to two reservoirs, we must consider barriers having both unequal temperatures and voltages on either side. In this situation, both the processes described above contribute to give a total heat flow of:

$$\dot{Q}_B = 2G_B \left[ \frac{V_{SD}^2}{2} - \left( \frac{k_B^2 \pi^2}{3e^2} \right) \bar{T} \Delta T \right] \quad (4.24)$$

where  $G_B$  is the conductance of the tunnel barriers,  $V_{SD}$  is the voltage difference between the reservoirs,  $\Delta T$  is the difference in temperature between the isolated region and the reservoirs, and  $\bar{T}$  is the mean of the temperatures of the isolated region and the reservoirs. For  $\dot{Q}_B = 0$ , this expression is equivalent to that used to successfully model self-heating in large quantum dots [134, 135].

By including Equation 4.24 in the balance of heat flow into the central region, the contribution of off-resonance tunnelling can be approximated in a way that is compatible with the orthodox theory of single-electron tunnelling. As far as such processes can be reasonably well described by a uniform background conductance, it should give a value of  $\dot{Q}_B$  with roughly the correct dependence on temperature and bias, and with a realistic magnitude, given an appropriate  $G_B$ .

The main weakness of this approach is that it is extremely difficult to predict a value for  $G_B$ . It will be determined by the strength of all four tunnel barriers forming the two dots, as well as the separation of excited states in the dots. This parameter must therefore be found by comparison with the data, and then afterwards checked to see if it is reasonable.

### 4.3.3 Predictions

By considering the three heat flows detailed in the previous section, the temperature of the central region can now be found for a given configuration of the QDR by converging to a value of  $T_C$  for which  $\dot{Q}_P + \dot{Q}_T + \dot{Q}_B = 0$ . This section presents some important predictions of this model.

Initially, only the heat flows due to the ‘ideal’ QDR current ( $\dot{Q}_T$ ) and the electron-phonon coupling ( $\dot{Q}_P$ ) are considered. In assuming that  $\dot{Q}_B = 0$ , the

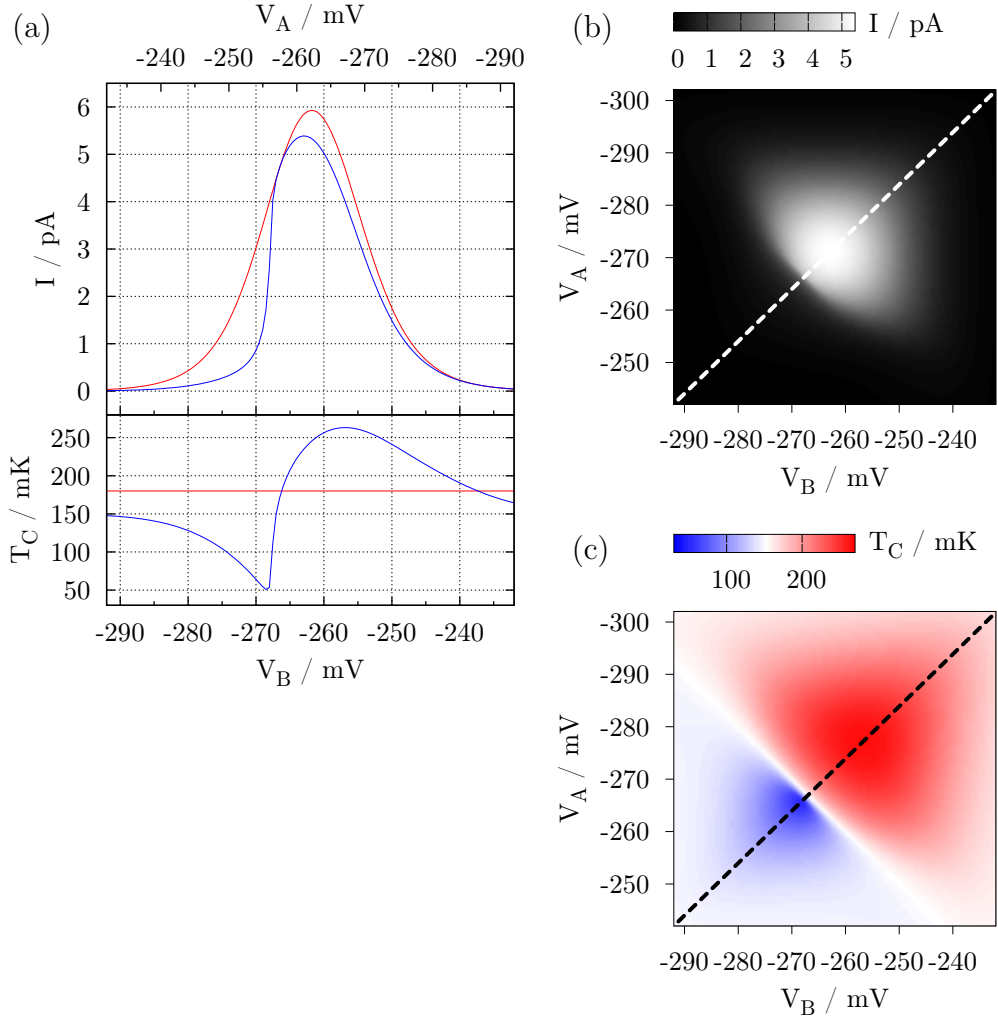
validity of the results are limited to the regime where the lifetime broadening of the ground states of both dots are much less than the thermal broadening, and where all excited states are far away in energy. A finite charging energy for the central region is included, but the capacitive coupling between the dots and the central region is initially neglected. Figure 4.14 shows a typical QDR current and the corresponding profile of  $T_C$ , given these assumptions.

Moving from right to left in Figure 4.14(a), we see that the central region is initially heated, because the gate voltages imply that  $\mu_A > \mu_B$ . Then around  $V_B = -265$  mV, the behaviour switches to cooling once  $\mu_A < \mu_B$ . In the situation considered here, where  $\mu_A$  and  $\mu_B$  do not depend on the central charge state, and the small bias ensures that only one central region charge state is available for transport, the behaviour of the system is similar to the ‘ideal’ QDR described by Edwards [2].

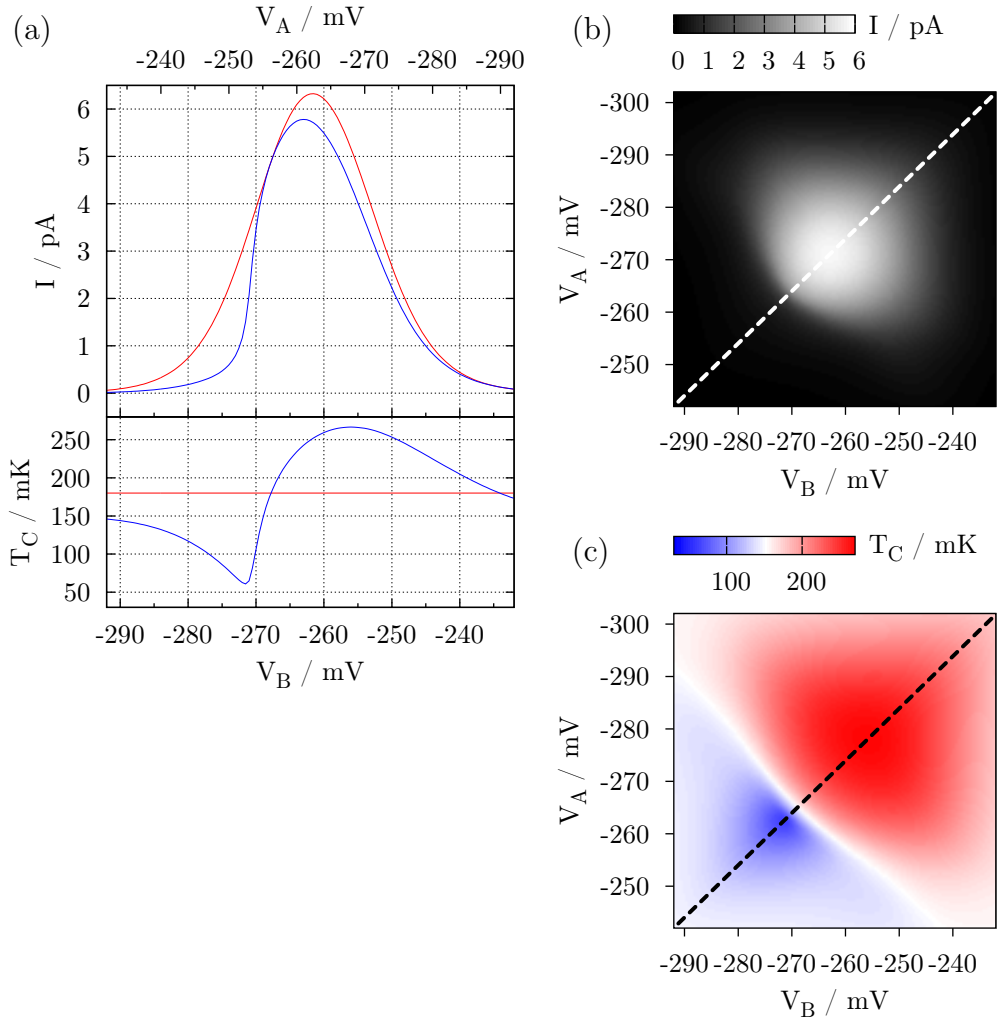
Next we consider the effect of introducing electrostatic coupling between the QDR components. The capacitances  $C_{AC}$  and  $C_{CB}$  are set such that the the energy of the central region shifts by approximately the measured value (24% of the central region charging energy) on the addition of a single extra electron to either dot A or B. Figure 4.15 shows the predicted current and  $T_C$  profile in this situation, with all other parameters the same as for Figure 4.14. The most obvious effect of including this ‘back-action’ is an increase in the size of the conduction point. However, most importantly, the model predicts that the QDR is still able to cool the central region. The base temperature [ $T_b = \min(T_C)$ ] is slightly reduced as compared to the uncoupled case, but it is still below both  $T_e$  and  $T_l$ . This shows that a QDR can, in principle, still function in the regime of strong electrostatic coupling between its components.

Figure 4.16(a) shows the change in base temperature for small back-action energies (less than half the central region charging energy). There is no noticeable change below approximately 1  $\mu$ eV, presumably because this is much less than  $k_B T_C$ . Above this value, a moderate increase in back-action reduces the QDR performance slightly. However this trend soon saturates, and the overall effect is quite small. (The  $\sim 10$  mK rise in base temperature is caused by a reduction in the total cooling effect from the QDR current ( $\dot{Q}_T$ ) of less than 1%.)

For larger coupling, the lost performance is actually recovered as the back-action energy approaches the central region charging energy. Figure 4.16(b) illustrates this for three different charging energies. This is probably because, as the back-



**Figure 4.14:** QDR model assuming no electrostatic coupling between its components and no off-resonance tunnelling. Notable parameters are  $T_l = 150$  mK,  $T_e = 180$  mK,  $V_{SD} = 75$   $\mu$ V, and the central region charging energy is 100  $\mu$ eV. (b) shows the QDR current and (c) the central region temperature, both as a function of the two dot gate voltages. In (a), the blue lines show the predicted current and  $T_C$  profile taken along the dotted lines in (b) and (c). The base temperature achieved [ $T_b = \min(T_C)$ ] is approximately 50 mK. For comparison, the red lines show the situation when the thermal model is not used and  $T_C$  is fixed at 180 mK.



**Figure 4.15:** QDR model including a back-action of approximately  $25 \mu\text{eV}$  between the dots and the central region. Notable parameters are  $C_{AC} = C_{CB} = 22 \text{ aF}$ ,  $T_l = 150 \text{ mK}$ ,  $T_e = 180 \text{ mK}$ , and  $V_{SD} = 75 \mu\text{V}$ . (b) shows the QDR current and (c) the central region temperature, both as a function of the two dot gate voltages. In (a), the blue lines show the predicted current and  $T_C$  profile taken along the dotted lines in (b) and (c). The red lines show the situation when the thermal model is not used and  $T_C$  is fixed at  $180 \text{ mK}$ .

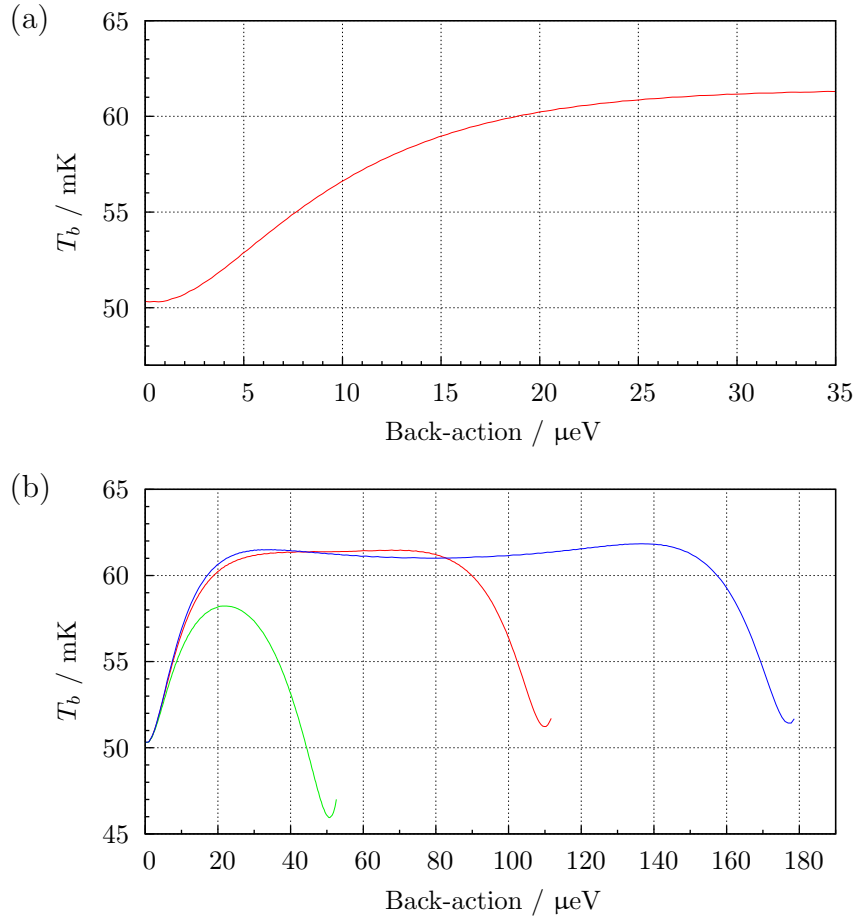


**Figure 4.16:** Base temperature ( $T_b$ ) as a function of dot-to-centre electrostatic coupling. (a) Detail of low-coupling behaviour for the same simulation parameters as Figure 4.15. (b)  $T_b$  over the full range of possible couplings for central region charging energies of roughly 50  $\mu\text{eV}$  (green line), 100  $\mu\text{eV}$  (red line), and 150  $\mu\text{eV}$  (blue line).

action energy approaches the central region charging energy, transport processes that are affected by the back-action would start to populate the next central region charge state. Once the back-action equalled the charging energy, they would match up perfectly and become equivalent to normal transport processes, but operating through the higher charge state. Significantly, the results in Figure 4.16 imply that electrostatic coupling can never have more than a small effect on the performance of a QDR.

Finally, we investigate the effect of including the approximation for off-resonance tunnelling through the dots. Figure 4.17 gives the predicted QDR current and temperature profiles for several values of  $\dot{Q}_B$ . It shows that as the conductance of the hypothetical tunnel barriers ( $G_B$ ) is increased, the base temperature rises. The

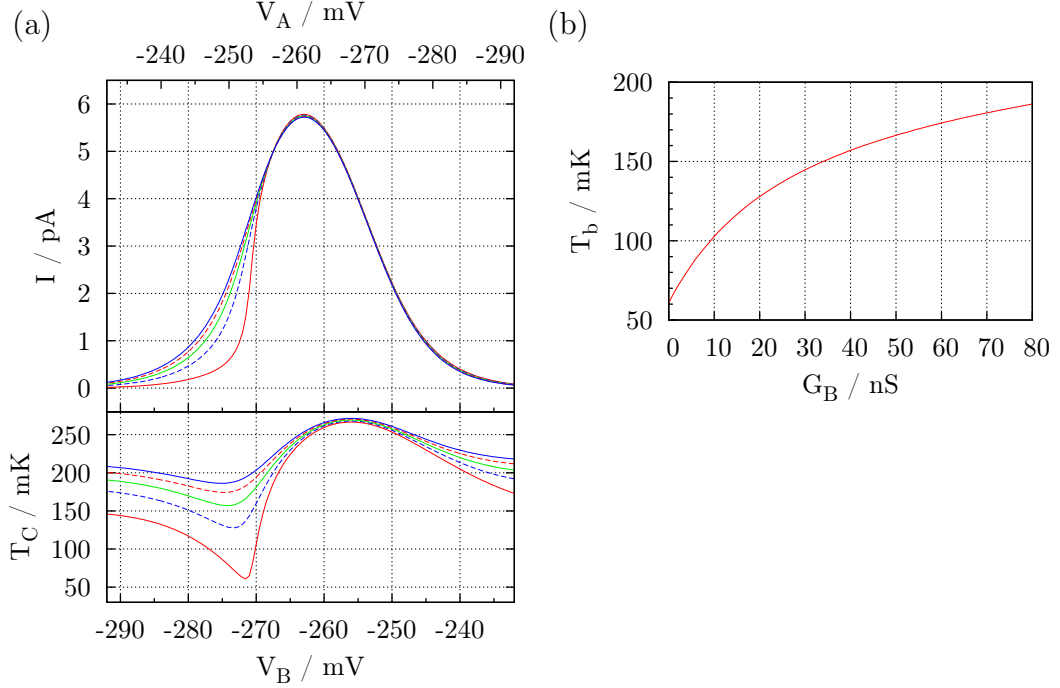


**Figure 4.17:** (a) QDR current and central region temperature profile for different values of  $\dot{Q}_B$ . The barrier conductances ( $G_B$ ) increase regularly from 0 nS (solid red line) to 80 nS (solid blue line), producing an increase in base temperature. For the warmest trace (solid blue line), the lowest  $T_C$  is greater than the equilibrium electron temperature (180 mK), and all cooling has been lost. (b) Base temperature as a function of barrier conductance.

values of  $T_C$  at the extremes of the peak also rise since  $\dot{Q}_B$  is heating the central region due to the applied bias, even when the resonant transport is suppressed. Once  $G_B$  has reached a value of 80 nS, the QDR is no longer acting to cool the central region at all ( $T_b > T_e$ ), and the line-shape of the current becomes symmetric. A conductance of 80 nS implies that the transport due to off-resonance tunnelling should be of comparable size to the resonant current ( $\approx 6$  pA). This is clearly outside the valid regime for the model, as the contribution to the current from off-resonance tunnelling is assumed to be small. However, even comparably small values of  $G_B$  produce significant increases in the base temperature and changes to the line-shape of the current peak.

Another observation from Figure 4.17 is that the value of  $G_B$  has little effect on the shape of the right side of the current peak. This is because on the right the electrochemical potentials of the dots are close to the electrochemical potentials of the source and drain, and the line-shape is mostly determined by the thermal

broadening in the reservoirs, provided that  $k_B T_C \ll eV_{SD}$ . On the far right of the peak, where changes in  $\dot{Q}_B$  strongly affect  $T_C$ , this condition is easily satisfied and the current is unaltered. Towards the centre of the peak  $\dot{Q}_B$  has less effect since it is exceeded by the heating from resonant transport. So even though here  $T_C$  may be elevated sufficiently to alter the current, the shape of the right side is insensitive to changes in  $G_B$ .

To summarise the results of this section; by including thermal balancing into the QDR model it has been shown that such a device can still function with strong electrostatic coupling between its components, and that the cooling of a mesoscopic charge island should therefore be possible. Furthermore, the postulated variations in  $T_C$  result in asymmetric peaks in the current through the device, with one side of the peak being far less sensitive to variations in the isolated 2DEG than the other. This behaviour agrees qualitatively with the measurements, and in the final two sections of this chapter we try to establish a quantitative agreement.

#### 4.3.4 Determining capacitances

To make a quantitative comparison between the model and the measured data, several device parameters must be determined. Most important was that the capacitor network in the model be fully populated with accurate values. To do this, independent measurements of the components of the device (the dots and the central region) were used wherever possible. Using these simpler measurements allowed the capacitances to be determined with the least ambiguity.

The total capacitances of the two dots were assumed to be the same;  $C_{AT} = C_{BT} = 89$  aF. This implies a charging energy for both dots of 1.8 meV, which differs from the measured values (see Section 3.4.1). However, their value does not affect the results of the model. This is because only a single charge state transition in each of the two dots is ever considered (their occupations in the model are limited to 0 or 1) and so the spacing between transitions, which is set by the charging energy, is unimportant. By choosing  $C_{AT} = C_{BT}$ , it was simpler to make later comparisons between other capacitances affecting the two dots.

From non-linear measurements of the two dots, the capacitances of their drain barriers were found to be characterised by the factors  $\alpha_D^T = 0.29$  eV/V and  $\alpha_D^L = 0.20$  eV/V. Given the chosen values of  $C_{AT}$  and  $C_{BT}$ , this implies that  $C_{DB} = 26$  aF and  $C_{AC} = 18$  aF. From the lithographic symmetry of the device, it was assumed that  $C_{SA} = C_{DB}$  and  $C_{CB} = C_{AC}$ .

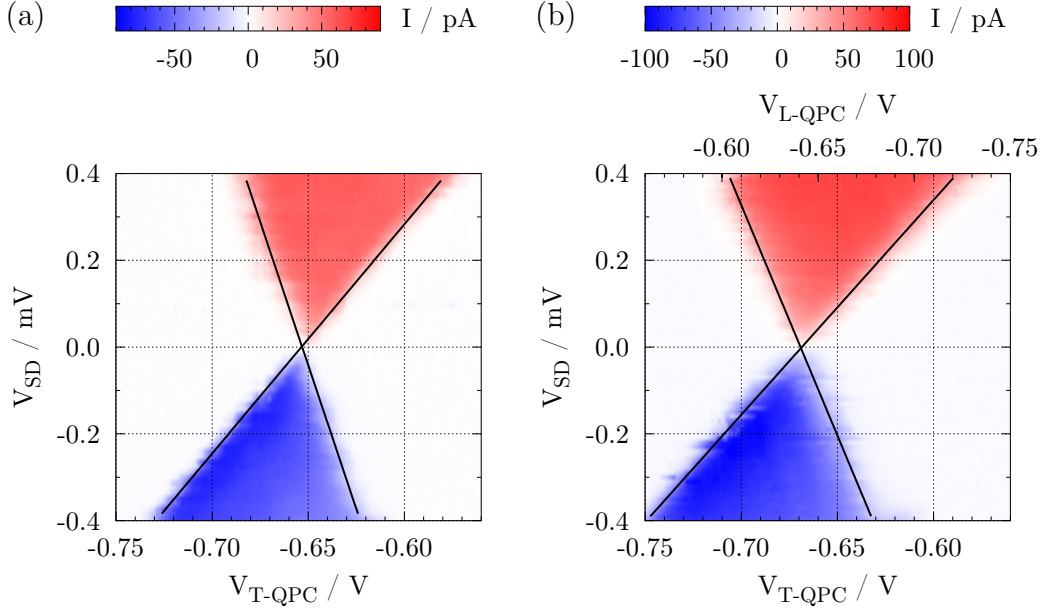


**Figure 4.18:** Non-linear DC measurements of a single blockade peak of the top dot. A small offset in bias has been subtracted for clarity. The black lines show the edges of the unblocked regions, as determined by the method detailed in Section 3.5. In (a), the lever-arm for probing the dot energy with the gate ‘T-QPC’ alone is found to be  $\alpha_{G2} = 0.00379$  eV/V. In (b), both the gates ‘T-QPC’ and ‘L-QPC’ are varied to calibrate the cross coupling between ‘L-QPC’ and the top dot, resulting in a lever-arm of  $\alpha'_{G2} = 0.00338$  eV/V. The coupling between ‘L-QPC’ and the top dot is then given by  $(\alpha_{G2} - \alpha'_{G2})$ .

When probing the dot energies with the gates ‘T-QPC’ and ‘L-QPC’, non-linear measurements of the dots show the gate lever-arms to be  $\alpha_{G2}^T = 0.00379$  eV/V and  $\alpha_{G2}^L = 0.00336$  eV/V. These define the capacitances  $C_{gA} = 299$  zF and  $C_{gB} = 338$  zF. By repeating these measurements while additionally sweeping the opposing dot’s gate in the opposite direction, the bare cross-coupling capacitances were found to be  $C_{BgA} \approx C_{AgB} \approx 35$  zF. Figure 4.18 shows how this value was determined for the top dot.

During the measurements of conduction points, the change in central region energy due to changes in  $V_{T-QPC}$  and  $V_{L-QPC}$  was compensated for by varying  $V_{R-OUT}$  appropriately (see Figure 3.22). In the model we therefore assume that  $C_{CgA} = C_{CgB} = 0$  and that  $V_C$  (the analogue to  $V_{R-OUT}$ ) is always constant. However, this makes the determination of  $C_{AgB}$  and  $C_{BgA}$  more complex than described above: ‘R-OUT’ also coupled to the two dots, but in assuming that  $V_C$  is constant we are neglecting this effect. Remembering that during the experiment the compen-

sation was governed by  $\Delta V_{R-OUT} = -(0.1835\Delta V_{L-QPC}) - (0.1835\Delta V_{T-QPC})$ , and assuming that  $C_{BgC} \approx C_{AgC} \approx C_{AgB} \approx C_{BgA}$  (from the physical arrangement of the gates), the effect of changing  $V_{R-OUT}$  can be accounted for by reducing  $C_{BgA}$  and  $C_{AgB}$  by a factor of 0.1835. In the model we therefore use  $C_{AgB} = C_{BgA} = 28$  zF.

To find accurate values for the capacitances characterising the central region, a different analysis was required. Because the centre formed a large dot with a continuum of states, non-linear measurements of current showed a series of peaks which widened with increasing bias. In contrast, the small dots with well defined single-particle states show sharply bounded triangular regions of conduction. To extract values for the charging energy and the gate lever-arm, the central region measurements were fitted to a calculation of current through a large dot. Furthermore, to model this current accurately, it was essential to include the effect of self-heating of the central region due to Joule heating at the biased tunnel barriers [134, 135]. Balancing Joule heating with cooling from the thermal conductance of the tunnel barriers and electron-phonon coupling, the equilibrium temperature in the centre was predicted.

Following the method of Kautz et al. [131], a numerical simulation of the current through a self-heated dot was implemented and fitted simultaneously to several line-scans from a non-linear measurement of current through the central region. The fitting parameters were the resistances of the two tunnel barriers, the total capacitance of the centre, the capacitances of the biased barrier and the gate electrode, and an offset in the gate voltage. The result is shown in Figure 4.19, and predicts a charging energy of 101  $\mu$ eV.

### 4.3.5 Analysis

The preliminary analysis of measurements of the fully defined QDR presented in Section 4.2 showed that, as long as the behaviour of the device is consistent with the model described therein, the data could only be explained by a reduction in the temperature of the central region. Using the full model for the QDR, detailed in the preceding parts of Section 4.3, we now address the question of whether such an explanation is consistent with the known parameters of the device and a physically reasonable mechanism for temperature variation in the centre.

To simulate the device, the parameters of the model determined by independent measurements were: the external electron temperature, and all capacitances in the capacitor network except for the gate capacitances for the two dots ( $C_{gA}$  and  $C_{gB}$ ).

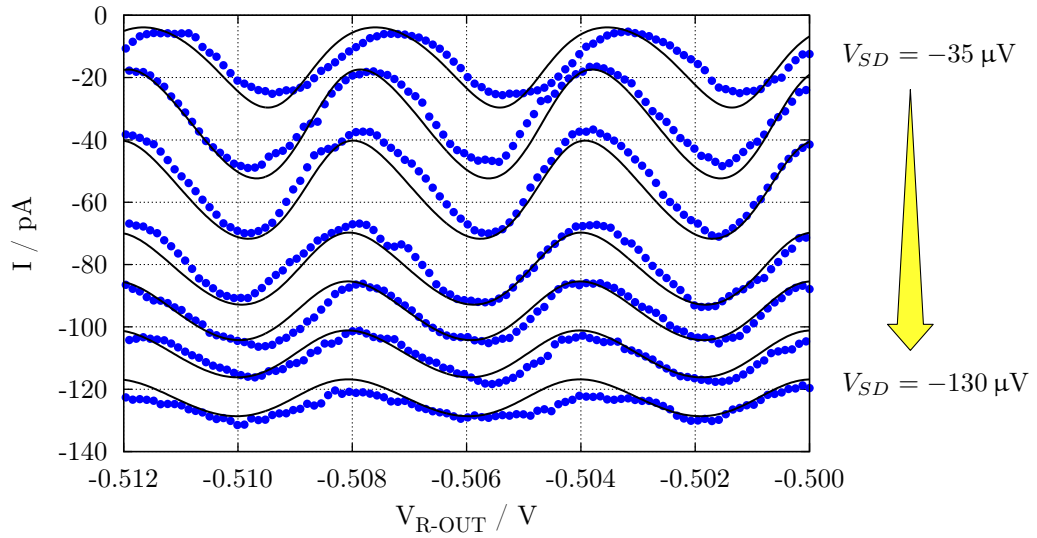


**Figure 4.19:** The result of fitting a model of current through a large quantum dot to 7 line-scans from the non-linear measurement of current through the central region [shown in Figure 3.14(a)]. The line-scans were taken at roughly equal spacings in the bias range indicated. The fitted parameters are: a total central region capacitance of 1602 aF ( $= C_{CT}$ ) and a gate voltage capacitance of 39 aF ( $= C_{gC}$ ). The total capacitance implies a charging energy of 101  $\mu$ eV. The fitted resistances of the source and drain tunnel barriers were 505 k $\Omega$  and 104 k $\Omega$  respectively, and the capacitance of the source barrier was 195 aF.

While values for  $C_{gA}$  and  $C_{gB}$  could be determined from independent measurements, they were found to be very sensitive to the tuning of the device. The value of the top dot gate capacitance ( $C_{gB}$ ) extracted from measurements of conduction points differed by up to 32% from the value found from measuring the top dot alone. For the left dot the biggest difference was only 12%, but this was still sufficient to jeopardise any comparison between the model and the measured data.

The model was fitted to measurements of conduction points at low bias using the following parameters:  $C_{gA}$  and  $C_{gB}$  determine the size of a conduction point; the position of the point gives offsets in the two dots' gate voltages; the height of the point gives the tunnel rate of the dots' barriers ( $\Gamma_0$ );<sup>4</sup> the shape of a conduction point is determined by the offset of  $V_C$  and the value of  $G_B$  (this is illustrated in Figure 4.20).

The fitting was performed using Levenberg-Marquardt nonlinear regression, as implemented in the function 'leasqr' in *GNU Octave*. The predicted current was fitted simultaneously to several (typically 20) line-scans from the data. Figure 4.21 shows an example fit of the full QDR model to the measurement of a low-bias conduction point. The result is that the measured conduction point implies a minimum temperature in the central region of approximately 110 mK. Given that the equilibrium electron temperature during this measurement was 140 mK, this means that the data are consistent with a cooling of the central region of approximately 30 mK.

The analysis shown in Figure 4.21 was repeated on three other measurements taken at two different temperatures of the dilution fridge. The results are summarised in Figure 4.22. In all three cases the predictions are found to fit well with the measured current, and show the data to be consistent with cooling of the central region. In the best case, the temperature reduction is over 100 mK. This shows that, with realistic parameters and a physically reasonable mechanism for cooling, the model predicts variations in  $T_C$  that result in line-shapes of current that are consistent with those observed. Specifically, it is the left side of the line-shapes that are affected by the profile of  $T_C$ . The extent of this correlation and an estimate for the sensitivity of the fit to  $T_b$  are illustrated in Figure 4.23.

In an attempt to make measurements of line-shapes with a lower noise in the current, measurements were made where the signal was averaged over a long time. A single line-scan through a conduction point was repeatedly measured, and the

---

<sup>4</sup>All four barriers are assumed to be equal. In tuning the device the dots were kept as similar and as symmetric as possible.

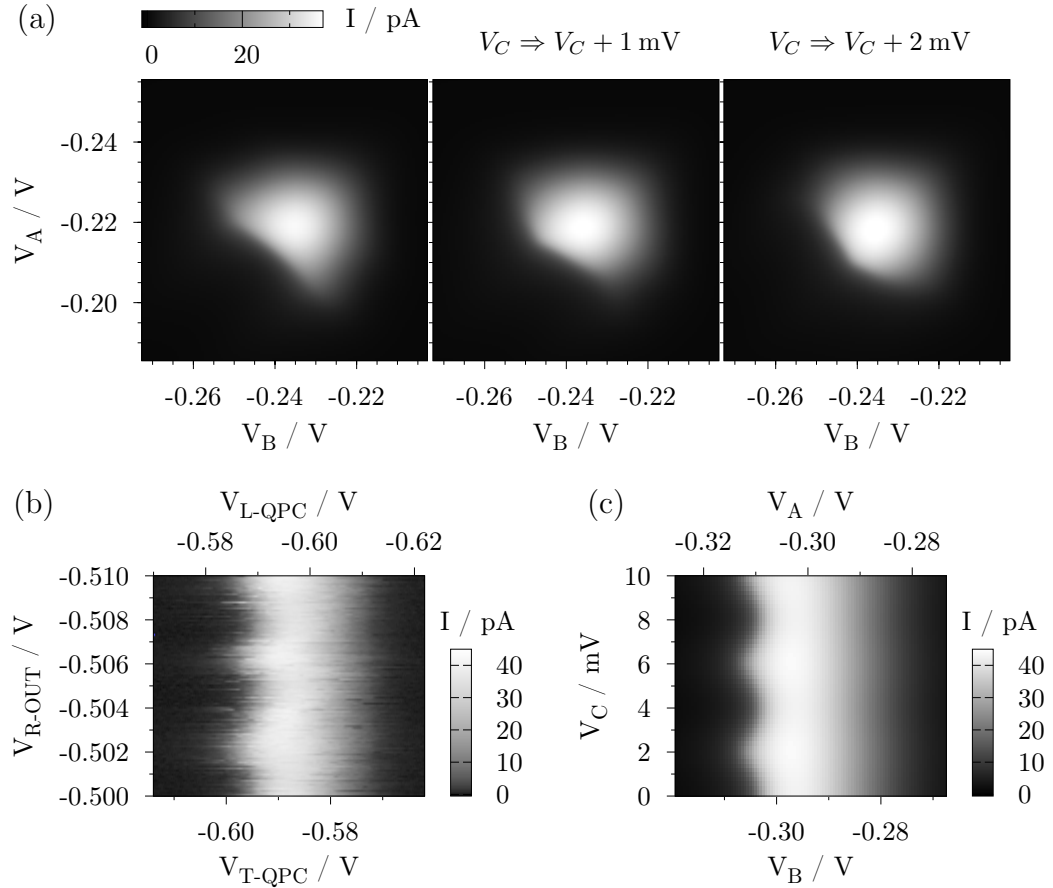


**Figure 4.20:** The shape of a conduction point changes with the gate voltage  $V_C$ , as shown by the series of simulations in (a). The shape of the bottom left edge of a point varies as successive charge states of the central region are moved through the bias window. (b) shows data from repeated measurements of a line-scan through the middle of a conduction point as  $V_{R-OUT}$  (equivalent to  $V_C$  in the model) is varied. The changing shape of the point appears as the periodic modulation of the left side of the peak. This behaviour is reproduced by the QDR model, as shown in (c).

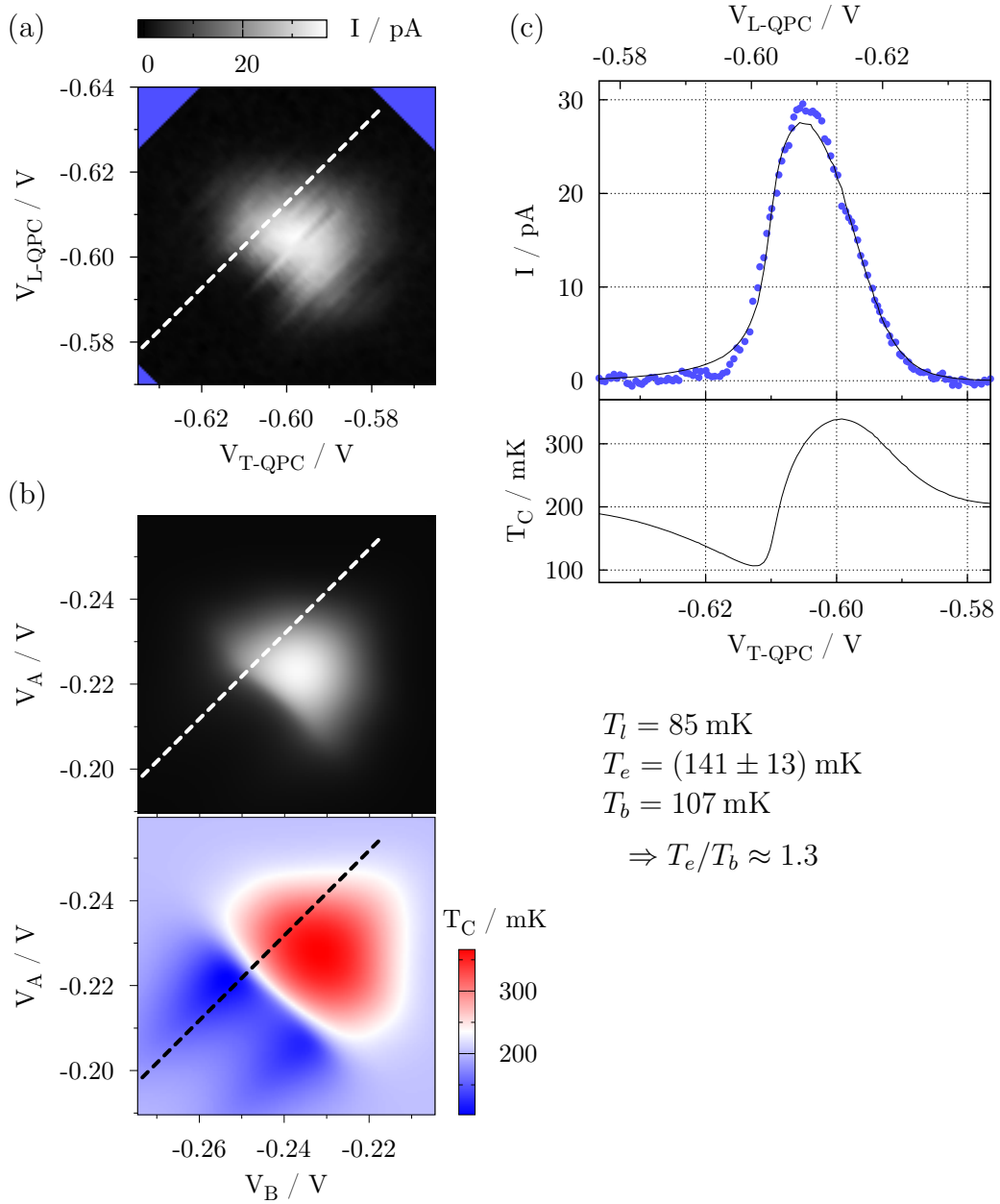


**Figure 4.21:** (a) shows the measured current through the device with a bias of  $V_{SD} = 75$   $\mu$ V. The current from the model is fitted simultaneously to several line-scans from the data in (a). This gives the parameters used to calculate the predicted QDR current and  $T_C$  profile shown in (b). (c) shows a single line-scan from the data (blue circles) compared to the calculated current (black line). The corresponding calculated profile of  $T_C$  is also shown. The line-scan was chosen to pass through a region of the conduction point where low values of  $T_C$  are found.

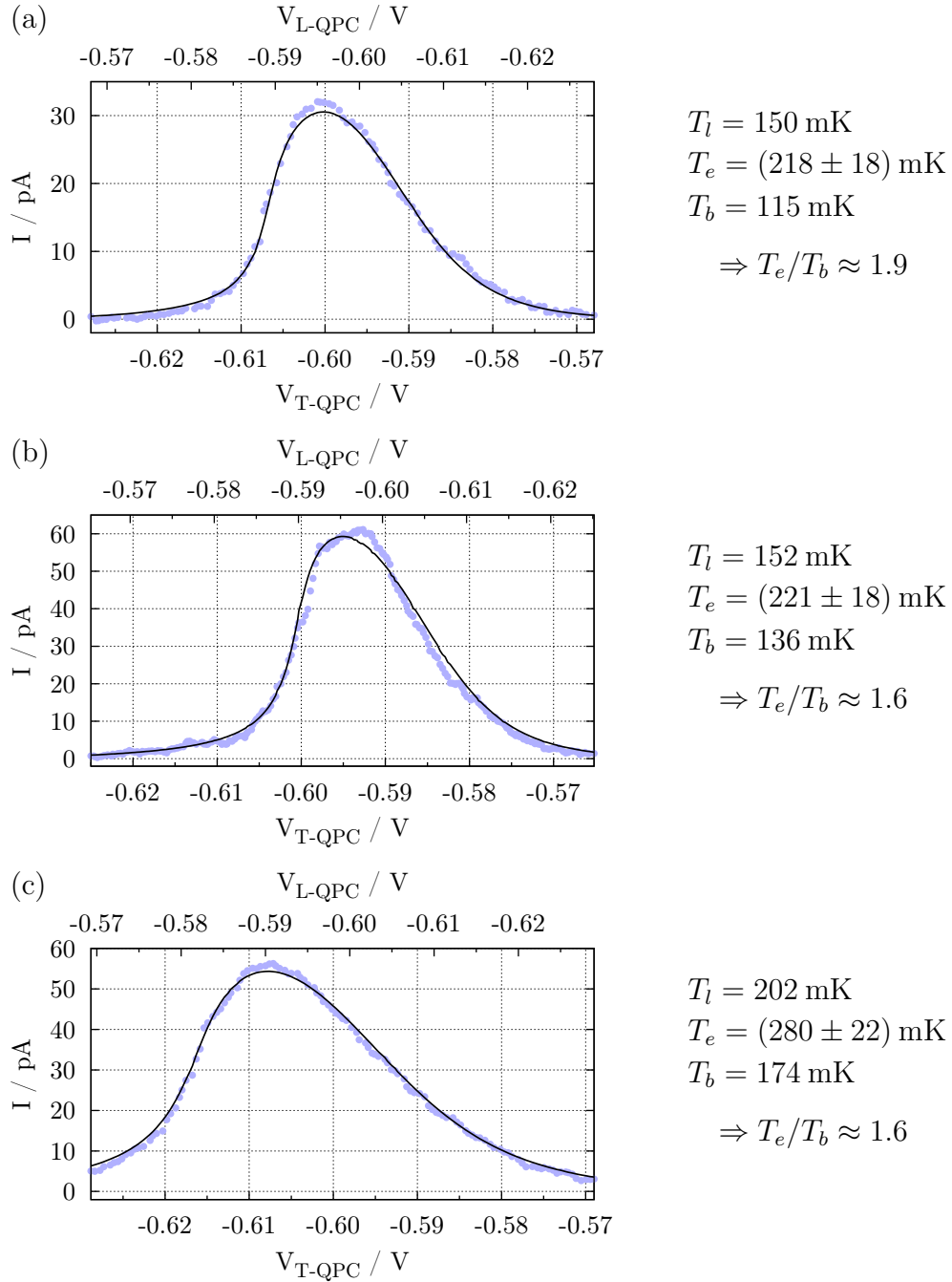


**Figure 4.22:** (a)—(c) are line-scans from fits of the full QDR model to measured conduction points. The particular sweeps were selected to include the lowest predicted values of  $T_C$ . (In (b), the coldest sweep fitted the data poorly due to a charge switching event during the measurement. A nearby sweep is shown instead.) Although the data in (a) and (b) were taken at the same temperature, they correspond to different tunings of the device.

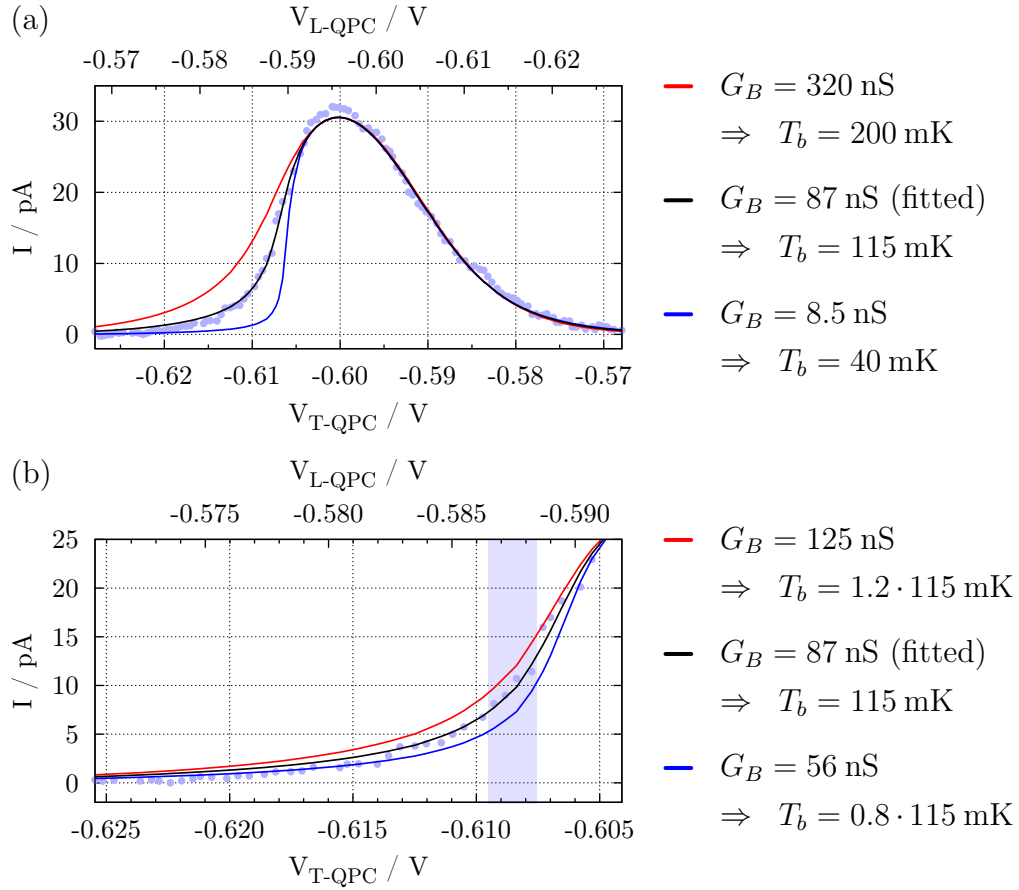


**Figure 4.23:** The data shown in both plots (blue circles) is the same as in Figure 4.22(a). The predicted current is recalculated with different values of  $G_B$ . (a) The larger value gives almost no cooling at all ( $T_e/T_b \approx 1$ ), while the smaller value gives more cooling than observed in any data set ( $T_e/T_b > 5$ ). The resulting change in the profile of  $T_C$  produces line-shapes that vary significantly from the measurement. (b) The values of  $G_B$  are chosen to illustrate the effect that a 20% increase or decrease in  $T_b$  has on the shape of the left side of the peak. The blue shaded region indicates where the lowest temperatures are expected ( $T_C$  is within 3 mK of  $T_b$ ). In this region, the difference between the calculated curves is largest, and the fitted (black) curve is clearly seen to be the best description of the data. For differences in  $T_b$  smaller than 20% the separation between the calculated curves is usually smaller than the noise in the current. We therefore assign a rough estimate for the error on  $T_b$  of  $\pm 20\%$ .

many resulting line-scans then averaged together. Figure 4.24(a) shows the result of fitting the full model to the average of several line-scans taken over a 5 hour period. In fitting to the data, all parameters except for  $\Gamma_0$  and  $G_B$  were found from a preceding measurement of the full conduction point. The fit was then performed by varying only these values, which were found to change slightly between the two measurements and during the measurement period. That these parameters were the most unstable is not surprising as they both related to tunnelling rates, which depend exponentially on tunnel barrier widths.

The resulting fit provides a good description of the averaged data. The base temperature is higher than that found from the associated measurement of the whole conduction point [Figure 4.22(b)]. This is due to the fact that the averaged line-scan did not pass through the lowest temperature region of the conduction point. However, in averaging the data over such a long time it is also likely that the line-shape was broadened by the effect of small charge-switching events. These primarily move the conduction point by small, random distances in the  $V_A$ - $V_B$  space. The main results here are that the asymmetric line-shapes persist over long times, and that only small systematic deviations from the model arise once the noise in the current measurement is reduced.

Figure 4.24(b) shows the results of fitting to another averaged data set, but in this case the averaged line-scans were not identical. The high  $T_e$  during this measurement meant that the dependence of the conduction point shape on the value of  $V_C$  was hard to discern. Therefore, to exclude the possibility that a poorly fitted value of  $V_C$  could produced an erroneous result, the effect of  $V_C$  was averaged out. To do this, line-scans were repeatedly measured, but with a different value of  $V_{R-OUT}$  (equivalent to  $V_C$  in the model) for each. The line-scans were then averaged over a range of  $V_{R-OUT}$  corresponding to a change in the central region charge of one electron. The result was fitted to a similarly averaged prediction from the model. Both this prediction and the data are independent of the initial potential of the central region.

The prediction in Figure 4.24(b) fits well to the averaged data. The resulting calculated base temperature ( $\bar{T}_b$ ) is now averaged over all the possible values for the central region potential. It is therefore an upper limit for the base temperature, but one that is independent of the particular value of  $V_C$  that was found from the shape of the conduction point.

Table 4.1 shows the temperatures, important fitted parameters, and predicted

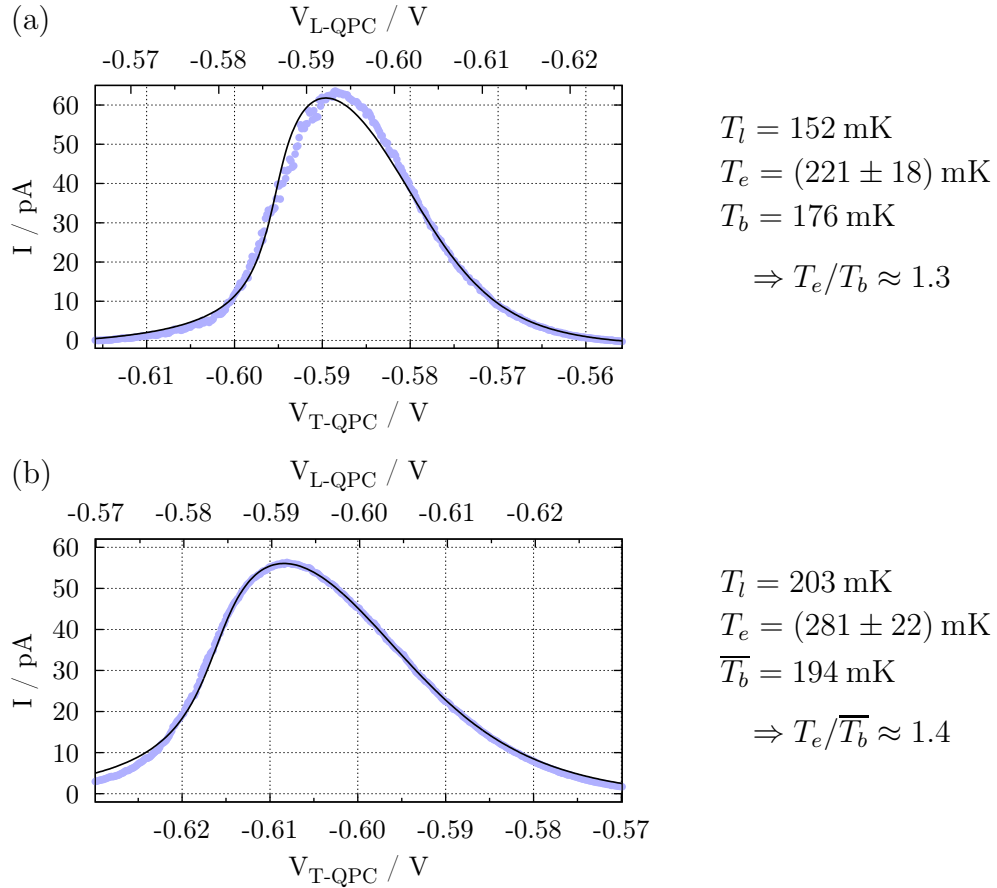


**Figure 4.24:** Fits of the full QDR model (black lines) to averaged measurements taken over several hours (blue circles). In fitting the model, only the parameters  $G_B$  and  $\Gamma_0$  were allowed to vary. All other parameters were determined from complementary measurements of the appropriate conduction points.

Data set			Full model						Simp. model	
Figure	$T_l$ /mK	$T_e$ /mK	$C_{gA}$ /zF	$C_{gB}$ /zF	$\Gamma_0$ /GHz	$G_B$ /nS	$T_b$ /mK	$T_e/T_b$	$T_b$ /mK	$T_e/T_b$
4.21	85	140	331	311	1.27	86.1	107	1.3	90	1.6
4.22(a)	150	218	299	372	1.24	87.3	115	1.9	113	1.9
4.22(b)	152	220	335	275	2.70	161	136	1.6	136	1.6
4.24(a)					2.68	234	176	1.3	153	1.4
4.22(c)	202	279	299	231	2.56	207	174	1.6	186	1.5
4.24(b)					2.75	229	176	1.4	170	1.6

**Table 4.1:** Results of fitting the full QDR model to all measurements shown in Section 4.3.5. For averaged data (rows 4 and 6) most parameters for fitting are taken from the preceding conduction point measurement (rows 3 and 5). For comparison, values for  $T_b$  found using the simple model (see Section 4.2) are also shown.

base temperatures for all the measurements shown in this section. In all cases the fitted tunnel rates give reasonable values, and the fitted values of  $C_{gA}$  ( $C_{gB}$ ) are within 12% (32%) of the independently measured value. The fitted values of  $G_B$ , however, are larger than expected: the largest value (234 nS) implies a current due to off-resonance tunnelling of almost 18 pA. Such a current should be clearly visible, and is not consistent with the lifetime broadening given by the fitted value of  $\Gamma_0$ . The most likely reason for this discrepancy is that the over-large value of  $G_B$  is accounting for other thermal processes in addition to the heat leak from off-resonance tunnelling.

For the small temperature differences that occur on the left side of the line-shapes,  $\dot{Q}_B$  is approximately linear in  $G_B$ . It could therefore account for any temperature-independent (or weakly dependent) thermal processes, for example irradiation by comparatively hot 4 K surfaces, or capacitive coupling to voltage noise in the gate electrodes. If true, this would imply that the highly elevated values of  $T_C$  predicted on the right sides of the line-shapes may not be accurate. Since the current is not sensitive to the temperature here, this is entirely possible.

The performance of the device is characterised by the ratio  $T_e/T_b$ , which is found to be always less than 2. This is consistent with the work of Edwards et al. [2], who calculated optimum values for  $T_e/T_b$  for different device configurations. Because the fundamental performance of a QDR is theoretically limited by off-resonance tunnelling, the most important device parameter is the separation of excited states in the entrance and exit dots. For  $T_e/T_b > 1.22$ , they found that the excited state

spacing must be greater than  $13.9k_B T_b$ . For our highest temperature results this gives an energy of 210  $\mu\text{eV}$ , which is largely consistent with observed excited state spacings in the two dots.<sup>5</sup>

For three of the measurements the analysis predicts that the central region electron gas has been cooled below the lattice temperature of the sample. Given the number of steps required to reach this conclusion, it should be treated with some degree of caution. In particular, the parameters  $C_{gA}$  and  $C_{gB}$  are found by fitting the full QDR model to the data and cannot be independently verified. These values determine the conversion factor between dot gate voltage and energy (i.e. temperature). Therefore, while the relation between  $T_e$  and  $T_b$  is sound, the absolute values of both may be subject to a largely invisible systematic error. This could be produced by, for example, a change in  $T_e$  between an electron-temperature measurement and a following conduction point measurement.

It should also be noted, however, that the heat-leak due to electron-phonon coupling is expected to be a relatively small contribution (typically being an order of magnitude smaller than the two other thermal processes in the model) and so there is little reason to expect that cooling below the lattice temperature should not be possible. Furthermore, there is also little evidence of serious instability in  $T_e$  that could produce such a result erroneously. It is therefore likely that cooling below the lattice temperature was achieved, but without a measurement of  $T_C$  that can be well calibrated, it is hard to rigorously support such a claim.

In the preliminary analysis presented in Section 4.2, the data were compared to a model for QDR transport that assumed a constant but reduced  $T_C$ . Given that this resulted in good fits to the measured line-shapes (some better than the full QDR model provides), it is obvious to ask whether this is not a better explanation of the observed results. A simple modification of the full QDR model shows that this is not the case. Figure 4.25, gives the result of fitting a measured conduction point to both the full QDR model, and a modification of the model which disregards the thermal balancing and instead uses a constant, fitted value of  $T_C$ . The result for the constant temperature model is clearly far worse, despite both fits having the same number of fitting parameters. This is the case for all the data presented in this section. The good fits seen previously were likely due to a large number of

---

<sup>5</sup>While excited state energies around 210  $\mu\text{eV}$  were often seen in the left dot, the value for the top dot was almost always around 400  $\mu\text{eV}$ . Such an asymmetric situation was not considered by Edwards, but we expect that the larger spacing in one dot will compensate for the smaller spacing in the other.

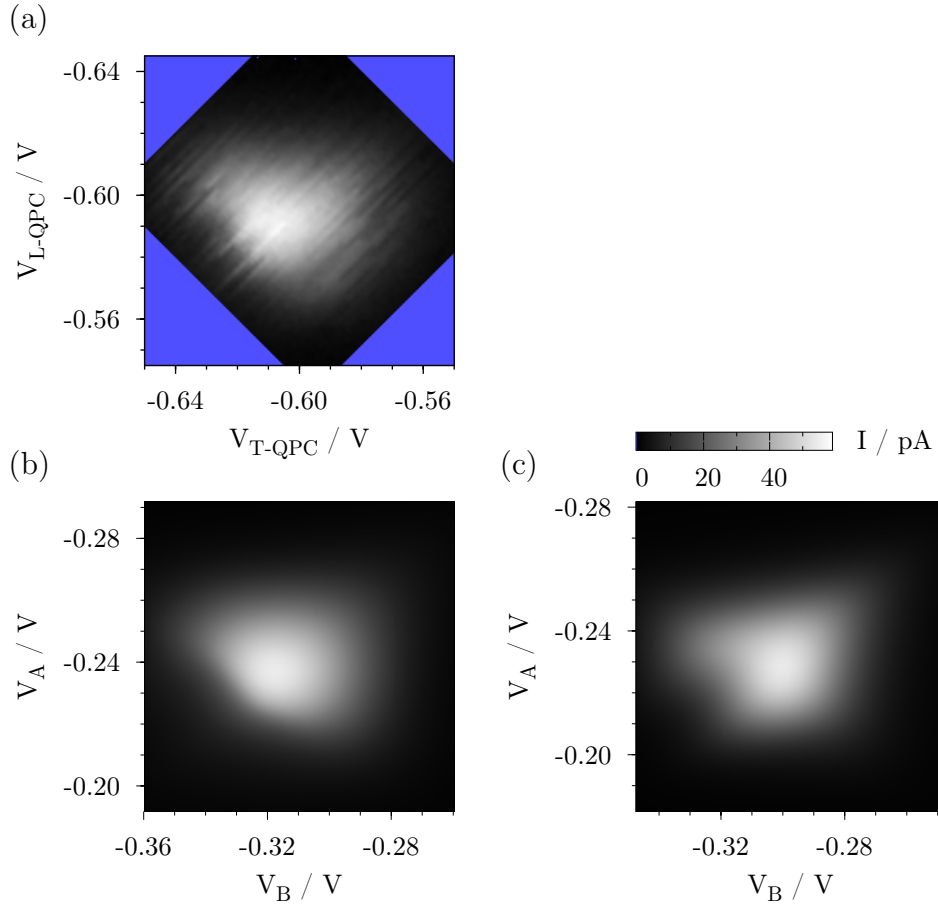


**Figure 4.25:** (a) Measured conduction point with  $T_l = 202$  mK,  $T_e = (280 \pm 22)$  mK and  $V_{SD} = 75$   $\mu$ V. (b) Best fit of the full QDR model to 20 line-scans from the data in (a). (c) Best fit of the constant  $T_C$  model to 20 line-scans from the data in (a).

parameters (5) being used to fit to a single line-scan. Once the whole conduction point is considered, the constant-temperature model is insufficient.

The full QDR model was not entirely successful in explaining the behaviour of the device. At equilibrium electron temperatures of 120 mK and below, the model did not provide good fits to the measurements. Figure 4.26 shows two examples of poor fits of the model to low temperature data. In general, the low-temperature data shows mostly symmetric line-shapes, which are found to be well described by the sum of two Gaussian peaks. This fitting involves 6 parameter for each single line-scan and should therefore be treated with caution. However, there is a plausible physical justification for fitting a set of peaks to the low temperature data. The most likely cause of deviation from the full QDR model is that the

electron-electron scattering rate in the central region has decreased enough to move the system into the out-of-equilibrium regime. This was discussed previously in Section 4.2.3, and was predicted to occur around 120 mK in this device. In this situation, current through the device would be suppressed except at gate voltages where electrons are injected and removed from the central region at the same energy. Trivially, this should occur at a unique value of  $V_A$  and  $V_B$ ; however, with the inclusion of electrostatic coupling between the device components, the condition may be satisfied at several pairs of voltages. We might therefore expect to observe a collection of peaks in current.

In conclusion, we find that the full QDR model describes the observed behaviour of the device well for  $T_e > 120$  mK. The model's physically motivated mechanism for predicting variations of the central region temperature results in calculated line-shapes that agree with those measured. Given the quality of the fits, the reasonable values of the fitting parameters, and the well-known applicability of the orthodox theory of single electron tunnelling, we assert that the model is highly likely to be an accurate description of the system. Given this assumption, the data are shown to imply successful cooling of the central region by amounts that are consistent with predictions for an ideal QDR. In the best cases, we observe temperature reductions of over 100 mK at ambient electron temperatures around 250 mK.

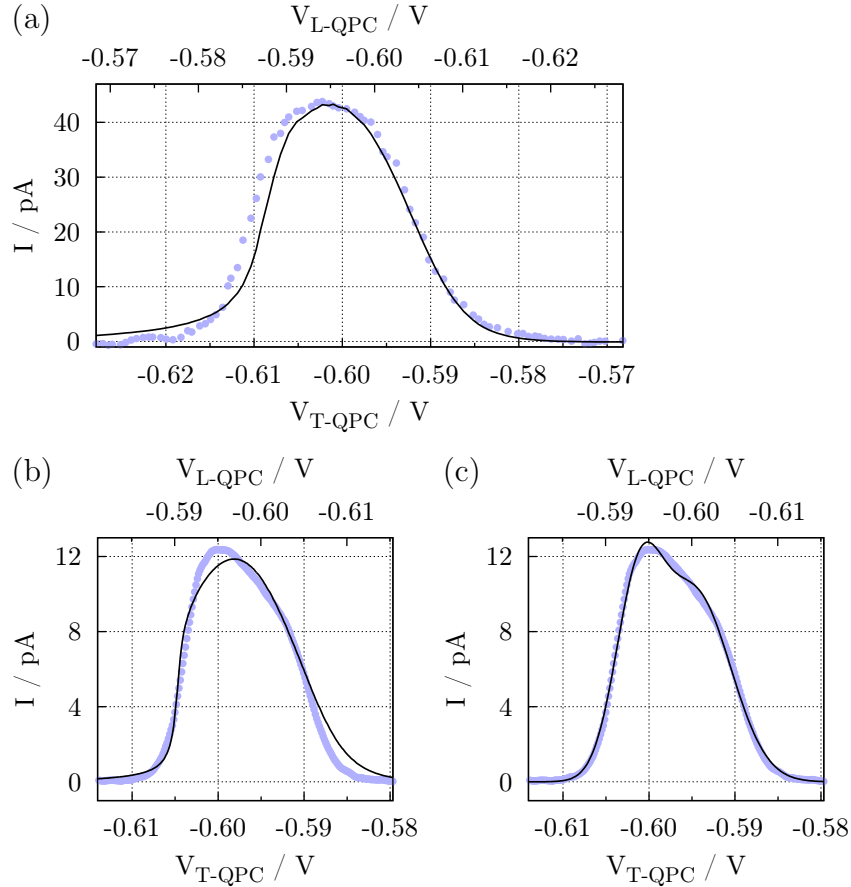


**Figure 4.26:** (a) shows an example line-scans from fitting the full QDR model to a conduction point measurement taken with  $T_l = 54$  mK and  $T_e = (105 \pm 12)$  mK. (As in previous analyses, the particular sweep was selected to include the lowest predicted value of  $T_C$ .) The observed line-shape is roughly symmetrical, and the model does not fit the data particularly well. Similarly poor fits are seen for other measurements with  $T_e \leq 120$  mK. In (b), the fit to an averaged measurement is shown. (As usual, the best fit was found by varying  $\Gamma_0$  and  $G_B$ .) The averaged data also shows a largely symmetric line-shape. We find that the data are better described by the sum of two Gaussian peaks, as shown in (c). Possible reasons for this are discussed in the text.

# Chapter 5

## Future measurements and improvements

---

In this chapter we discuss new directions for the study of quantum dot refrigerators. Firstly, we explore the utility and limitations of using a third quantum dot, coupled to the cooled 2DEG, as a probe of QDR behaviour. An experiment that demonstrates the basic principle of operation for such a probe is described. Secondly, we discuss how a pair of QDRs could potentially be used to provide a cooled environment for an arbitrary nano-scale electronic device.

### 5.1 A quantum dot thermometer

The addition of a third quantum dot to a QDR to provide an independent thermometer of the cooled 2DEG was discussed in the original proposal [2]. However, with a cooled region that is small enough to form a charge island at the device's operating temperature, this principle is no longer valid. The addition of a third dot would result in a system with four coupled charge islands, with the potential of the cooled region depending on the charge state of all four. The thermometer dot could not be considered a non-invasive probe in this situation, as changes in its charge state would have a strong perturbing effect on the rest of the system.

In future designs, the integration of a thermometer dot could be achieved by increasing the capacitance of the isolated region, thereby decreasing its charging energy and its coupling to the dots. This could be done simply by increasing the

isolated region's size, or by fabricating a large grounded gate on the surface above it. The latter technique has been used in recent investigations of the influence of Coulomb blockade in Fabry-Perot interferometers to reduce the charging energy of an  $18 \mu\text{m}^2$  2DEG region [139].

Given the agreement we have observed between predicted and measured QDR performance, it is reasonable to assume that the original theoretical analysis is largely sound. In this case, 2DEG regions with areas of  $\sim 100 \mu\text{m}^2$  should be able to be cooled at temperatures accessible by a dilution refrigerator (see Figure 3.2). The capacitance between a  $100 \mu\text{m}^2$  top-gate and a 90 nm deep 2DEG is 127 fF. This implies that the charging energy for a region of this size with such a gate above it would be less than  $1.3 \mu\text{eV}$ . (This neglects the region's self-capacitance and lateral capacitances to adjacent 2D regions, which would further reduce the charging energy.) It therefore seems highly likely that a QDR device with an isolated region of  $100 \mu\text{m}^2$  or larger could incorporate a thermometer dot.

The usefulness of a third dot would be greatly increased by the incorporation of an adjacent point-contact detector. This is a common technique used to non-invasively measure the charge state of a dot (see Section 2.2.6). With a direct measure of its charge state, it would not be necessary to pass any current through the dot. The thermometer would therefore have a negligible heat leak to the cooled region. Furthermore, the coupling between the thermometer and the cooled region could be reduced significantly, even to the regime where individual charging events in the dot could be observed and counted. Reducing the coupling increases the lifetime of the states in the dot, and therefore the intrinsic resolution of the thermometer. In the single-electron counting regime, the lifetime broadening of the dot states could trivially be reduced to  $\sim \text{nK}$ . All of the relevant techniques for implementing this measurement have been demonstrated [48, 50, 140, 141].

Incorporating a thermometer dot into a QDR would provide an independent, well calibrated measure of the temperature of the cooled 2DEG. It could also be used to provide information when operating in the out-of-equilibrium regime. In this situation we expect the distribution of occupied states in the isolated region to be driven away from a Fermi function because of the inability of the electrons to redistribute their energy through fast scattering. The thermometer dot should be able to reveal the shape of the distribution of occupied states in the out-of-equilibrium regime, just as in the quasi-equilibrium regime.

A preliminary experiment was performed to demonstrate the thermometer dot

concept using the same surface gate design as the QDR device. This is described in the following two sections.

### 5.1.1 Measurement setup

The measurements presented here were made on the device *dc-test1-2a* (for details, see Appendix A.2). The surface gate design was largely similar to the device considered in the previous two chapters, except that the area of the isolated region was only  $4 \mu\text{m}^2$ . All measurements were made in a Helium-3 cryostat with a base temperature of just under 300 mK.

The electrical measurement setup is described in Figure 5.1. It allowed the conductance of one dot to be measured at the same time as the current through its adjacent point-contact detector. The maximum bandwidth when measuring the point-contact current was 3 kHz, but in practice this had to be limited to less than 1 kHz to maintain an acceptable signal-to-noise ratio.

### 5.1.2 Results

Three gates ('L-PL', 'L-OUT' and 'L-IN') were tuned to define the left of the three dots in the device [see Figure 5.2(a)]. The adjacent point-contact was set to region of highly non-linear conductance, and therefore high detector sensitivity, with the gate 'L-QPC'. A point-contact conductance of approximately  $5 \mu\text{S}$  was found to give the best detector sensitivity. The value of  $V_{L-QPC}$  was typically tuned to give this value before every measurement.

Figure 5.2(b) shows the conductance of the dot and the detector current as a function of the voltage ( $V_{L-PL}$ ) on the plunger gate of the dot. As expected, the detector current shows clear upward steps each time the charge occupancy of the dot decreases by one electron. The steps persist long after transport through the dot is visible, providing information about the dot when it is very weakly coupled to its reservoirs. On the far left side of the plot the tunnel rates of the dot barriers are lower than the measurement bandwidth of  $I_{QPC}$ . The QPC signal therefore no longer reflects the average charge occupancy of the dot, but shows sharp steps that correspond to single electron tunnelling events.

Figure 5.3 shows the conductance of the dot and the current through the detector over a range of biases ( $V_{SD}$ ) applied across the dot. On the right side of the plots (where there is significant transport through the dot) the detector sig-

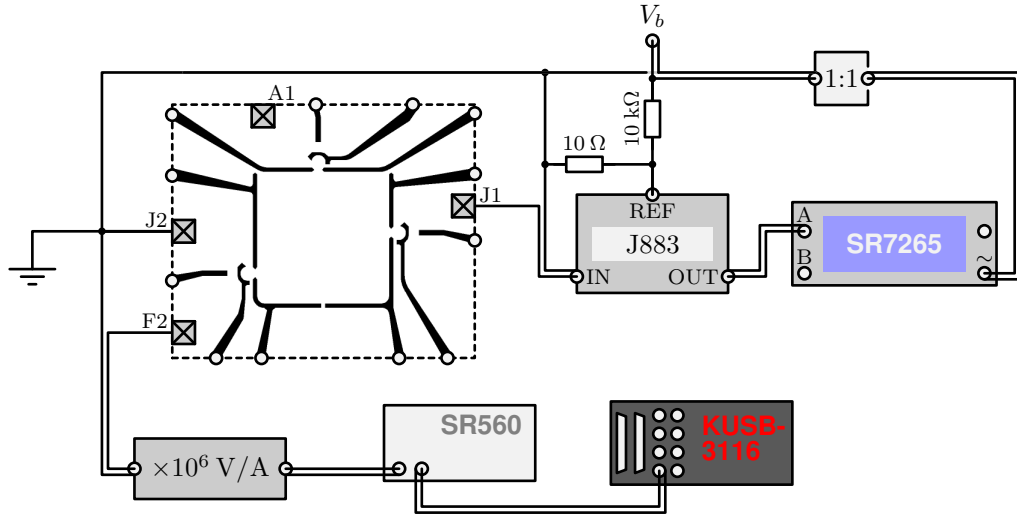


**Figure 5.1:** Setup for measuring simultaneously the conductance of the left hand dot and the current through its adjacent point-contact detector. The dot’s conductance is measured using the Signal Recovery *SR7265* lock-in amplifier and the *J883* current-to-voltage preamplifier. The excitation for this lock-in measurement is provided by the built-in oscillator of the *SR7265*. This signal is added to a constant bias voltage ( $V_b$ ), then both are divided down by a factor of 1000 and applied to the reference input of the preamplifier. The amplitude of the AC excitation applied across *J1* and *J2* is  $100\ \mu\text{V}$ , and the DC bias is  $V_{SD} = V_b/1000$ . The *1:1* audio frequency transformer breaks an earth-loop.

The setup for measuring the current through the point-contact detector was designed to allow the observation of single electron tunnelling events up to  $\sim\text{kHz}$ . The “ $\times 10^6\ \text{V/A}$ ” preamplifier drives a current through the point-contact due to an offset voltage on its input of approximately  $200\ \mu\text{V}$ . This amplifier has a bandwidth of  $3\ \text{kHz}$ . Its output is amplified by a further factor of 1000 and filtered (typically with a low-pass filter) by the Stanford Research Systems *SR560* amplifier. The result is then measured using an ADC channel of a Keithley *KUSB3116* DAC/ADC module, which can sample the signal at up to  $500\ \text{kS/s}$ .

Voltages on all the gates are provided by further Keithley *KUSB3116* modules (not shown.)

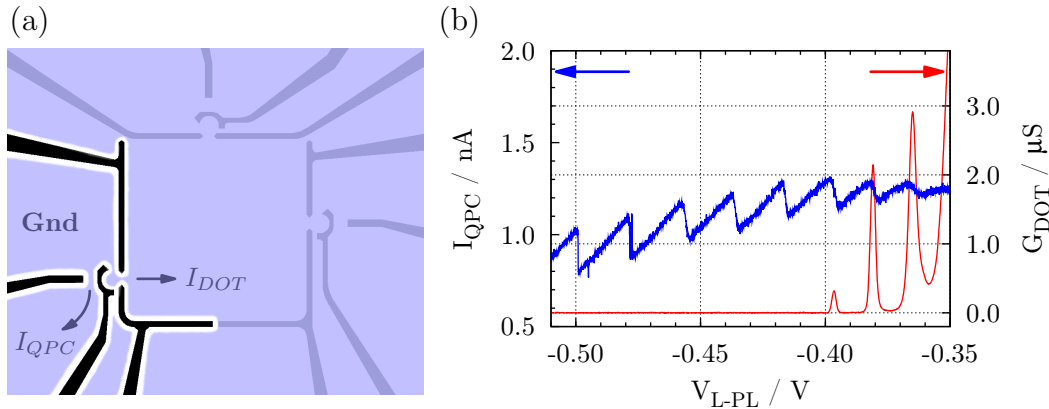


**Figure 5.2:** The gates used during this experiment are shown as black in (a), with the blue regions depicting the undepleted 2DEG. Both the conductance of the dot ( $G_{DOT} = \frac{dI_{DOT}}{dV_{SD}}$ ) and the current through the adjacent point-contact ( $I_{QPC}$ ) are plotted in (b). On the right side of the plot, the steps in  $I_{QPC}$  coincide with the Coulomb blockade peaks of the dot. They are interpreted as being caused by the change in charge state of the dot.

nal shows some, but not all features seen in the conductance of the dot. This is because, depending on the relative tunnel rates of the dot barriers, some features do not result in a change of the average charge state of the dot. These will be invisible to the detector. In the weakly coupled regime (on the left of the plots) the only visible feature in the detector signal is the dot's resonance with the unbiased reservoir. This implies that of the two tunnel barriers, the barrier to the unbiased reservoir has a significantly larger coupling.

Switching noise is observed in both plots in Figure 5.3. The detector signal is more noisy because it is intentionally very sensitive to the local electrostatic environment. In general, switching noise was a problem throughout the experiment and was most likely due to the particular material used.

In order to use a dot as a thermometer for just one of its reservoirs, it is necessary to tune its tunnel barriers to be appropriately asymmetric. The detector signal can be used to do this, as illustrated in Figure 5.4. With a constant, non-zero bias across the dot, a change of barrier asymmetry will produce a shift in the position of the detector steps. This corresponds to the steps moving from one edge of the Coulomb diamonds to the other. Such a shift is seen in Figure 5.4(b), and the change of dominant barrier is confirmed by measurements of the Coulomb diamonds either side of the transition.

The dot gates were set to a tuning for which the tunnel coupling to the biased

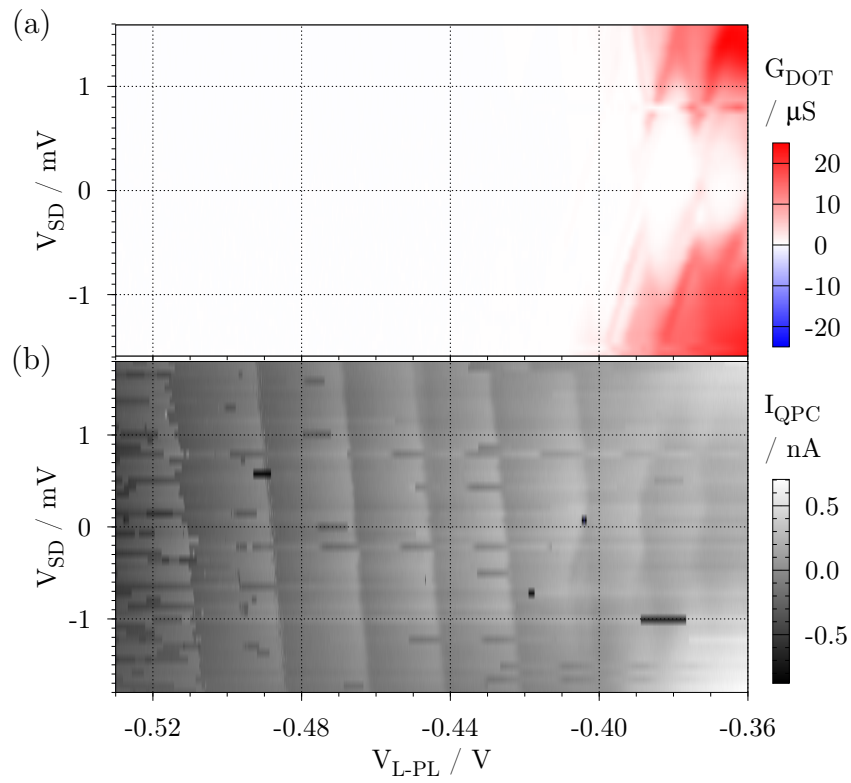


**Figure 5.3:** The conductance of the dot (a) and the point-contact current (b), as a function of the dot's bias voltage ( $V_{SD}$ ). In (b), the average value of every sweep has been subtracted to keep the signals within the same range.

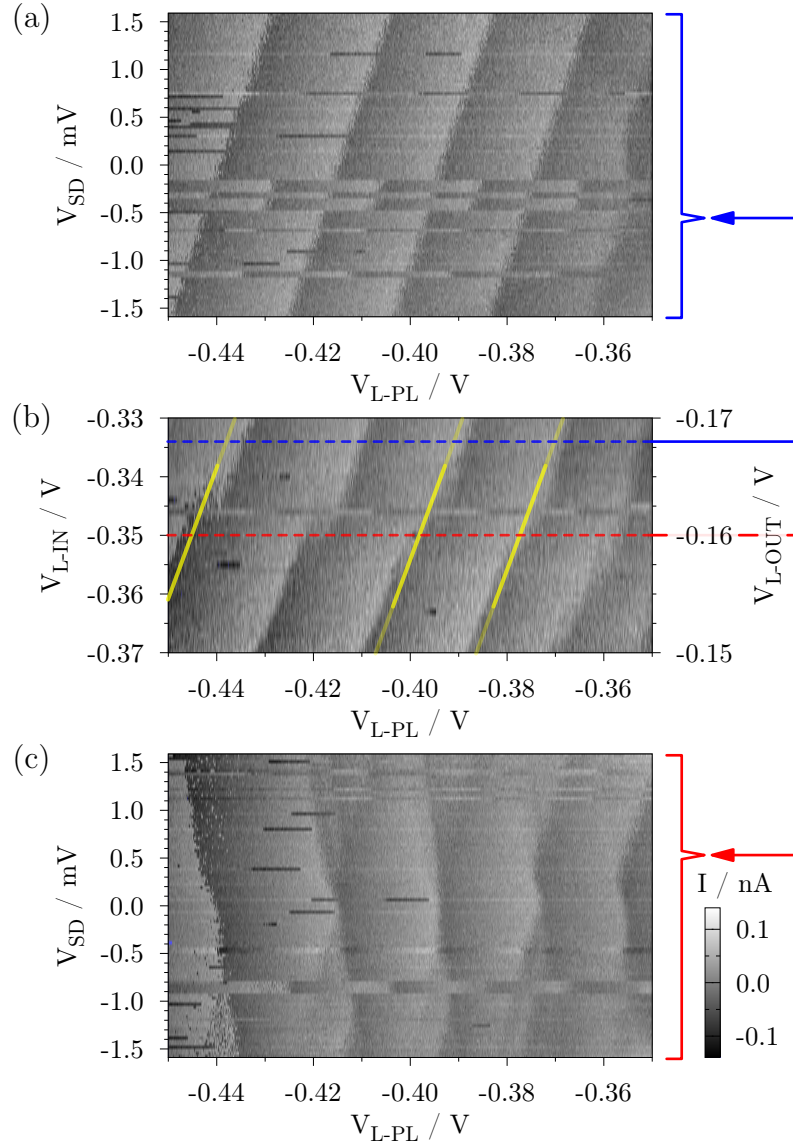


**Figure 5.4:** The relative strengths of the dot barriers were tuned by changing  $V_{L-IN}$  and  $V_{L-OUT}$ . (b) shows the detector signal with  $V_{SD} = 0.75 \text{ mV}$  as  $V_{L-IN}$  is increased and  $V_{L-OUT}$  is decreased. Around  $V_{L-IN} = -0.345 \text{ V}$ , the steps shift to the right as the dominant barrier switches. After this point, the tunnel coupling to the biased reservoir is strongest. (a) and (c) show detected Coulomb diamonds of the dot at two different tunings of  $V_{L-IN}$  and  $V_{L-OUT}$ . The direction of the steps in (a) shows that the tunnel barrier to the biased reservoir dominates. In (c), the tunnel coupling to the unbiased reservoir is stronger, although the two barriers are roughly similar. This is deduced from the fact that the signal in (c) shows evidence of both edges of the Coulomb diamonds at some points.

reservoir was much stronger than to the unbiased reservoir, and the regime where its tunnel rate was lower than the detector bandwidth was explored. While stepping across a single charge transition, the detector signal was sampled at a rate of 1 kHz for 2 s intervals. The results showed clear evidence of single electron charging events close to the transition [see Figure 5.5(a)]. By averaging the detector signal over a sufficiently long time, the Fermi-function shape of the transition is found, corresponding to the density of occupied states in the biased reservoir. The result is shown in Figure 5.5(b). The width of this transition is directly proportional to the temperature of the biased reservoir, with the conversion factor being found from the gradients of the Coulomb diamond edges.

From the plots (a) and (c) in Figure 5.4, the lever-arm for the gate ‘L-PL’ is found to be  $\alpha_G = (0.0997 \pm 0.0132)$  eV/V. The width of the Fermi function fitted to the averaged data in Figure 5.5(b) is  $(0.239 \pm 0.006)$  mV. This gives in a temperature of  $(277 \pm 37)$  mK, which is consistent with the base temperature of the cryostat being 305 mK during this measurement.

The relatively large error on the temperature comes from the estimated error on  $\alpha_G$ . This in turn is due to the measurement in Figure 5.4(c) having been made with almost symmetric tunnel barriers. The detector signal therefore showed some features of both sides of the Coulomb diamonds, as well as some excited states. This made it hard to determine the gradient of the unbiased reservoir resonance. In general, this error could easily be reduced by using more asymmetric tunnel barriers when determining the gradients of each side of the Coulomb diamonds.

The tunnelling rates across the dominant barrier can be found by analysing the statistics of the single electron tunnelling events seen in the detector signal. For Poissonian tunnelling, the probability of an electron staying on (off) the dot for a time  $t_{\text{on}}$  ( $t_{\text{off}}$ ) is expected to be proportional to  $\exp(-\Gamma_{\text{off}}t_{\text{on}})$  [ $\exp(-\Gamma_{\text{on}}t_{\text{off}})$ ], where  $\Gamma_{\text{off}}$  ( $\Gamma_{\text{on}}$ ) is the rate of tunnelling off (onto) the dot. The measurements were analysed to extract the statistics of  $t_{\text{on}}$  and  $t_{\text{off}}$  in the middle of the charge-state transition, where we expect  $\Gamma_{\text{on}} \approx \Gamma_{\text{off}}$ . Figure 5.5(c) shows that the frequency of longer dwell times ( $t_{\text{on}}$ ) falls exponentially, as expected. A fitted exponential decay gives a rate of  $\Gamma_{\text{off}} = 79$  Hz, and a similar analysis of  $t_{\text{off}}$  gives  $\Gamma_{\text{on}} = 74$  Hz.

To find the true tunnel rates, the finite bandwidth of the detector must be taken into account. For a detector bandwidth of  $\Gamma_D$ , the true tunnel rates ( $\Gamma_{\text{on}}^*$  and  $\Gamma_{\text{off}}^*$ ) are given by [142, 143]:

$$\Gamma_{\text{on}}^* = \Gamma_{\text{on}} \frac{\Gamma_D}{\Gamma_D - \Gamma_{\text{on}} - \Gamma_{\text{off}}} \quad (5.1)$$

$$\Gamma_{\text{off}}^* = \Gamma_{\text{off}} \frac{\Gamma_D}{\Gamma_D - \Gamma_{\text{on}} - \Gamma_{\text{off}}} \quad (5.2)$$

From the time taken to resolve a single charge transition, the bandwidth of our detector is estimated to be approximately 250 Hz. This implies that the true tunnel rates in the dot are  $\Gamma_{\text{on}}^* \approx 180$  Hz and  $\Gamma_{\text{off}}^* \approx 210$  Hz.

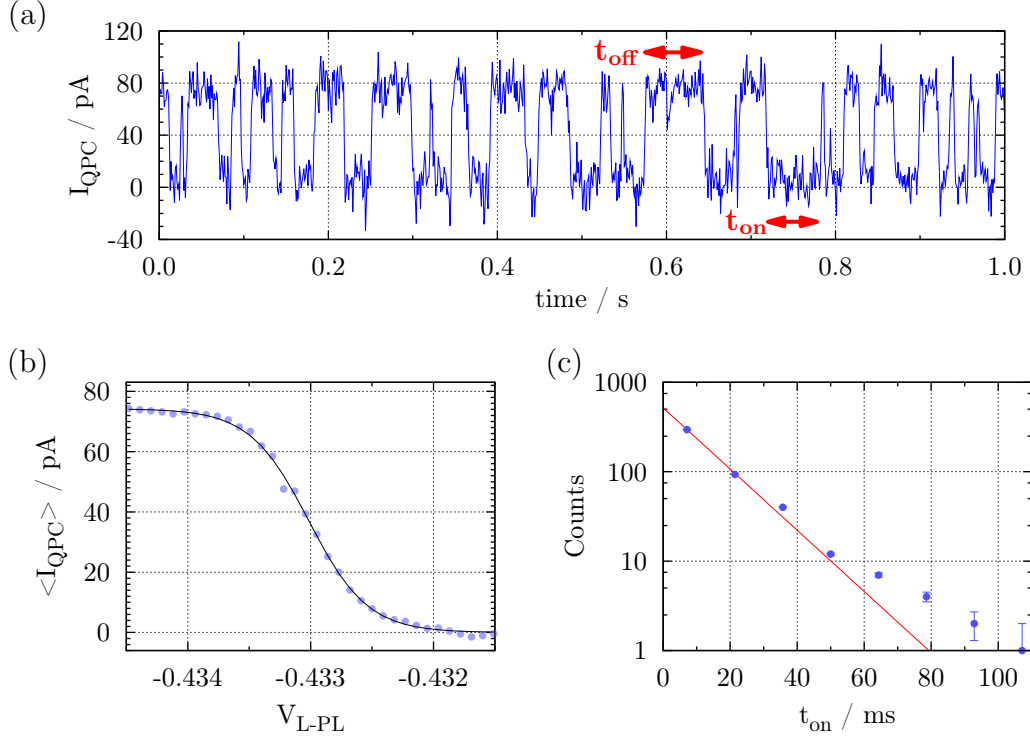
In conclusion, this experiment demonstrated the ability of a single dot of the same design as used in the QDR device to act as a non-invasive thermometer. Via the use of an adjacent point-contact detector, the thermometer can measure either its reservoirs independently with extremely low tunnel couplings to both. Low coupling minimises the heat leak through the dot. With single electron counting techniques, both the heat leak and lifetime broadening of the dot states can both be reduced to levels which pose no limitation at all on the use of this scheme in conjunction with a QDR.

## 5.2 An experimental platform

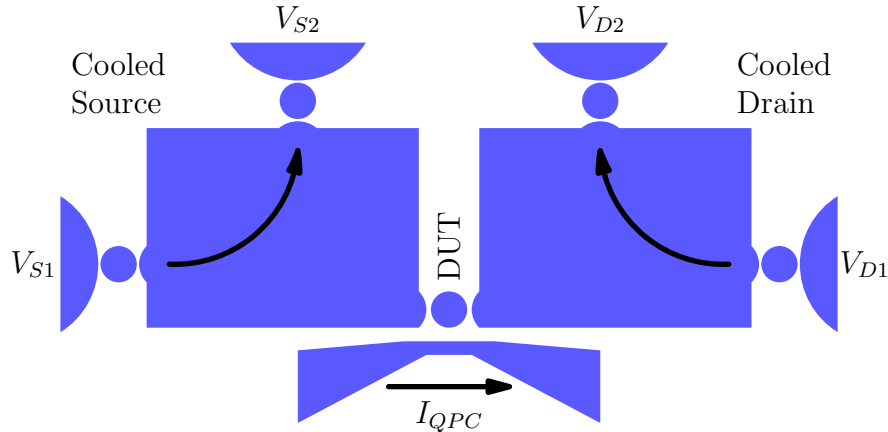
A primary motivation for developing a QDR is to obtain cold 2D electron gases with which other experiments may be performed. In achieving this, great care must be taken to keep dissipation and heat leaks small enough that the cooling power of the QDR is not overwhelmed. In particular, any direct electrical contact to the cooled regions is likely to provide too large a heat leak, meaning that most measurements must be performed non-invasively.

Figure 5.6 outlines a scheme for how two QDRs could be used to provide source and drain reservoirs for an arbitrary device. The device could be probed using a point-contact detector, which implies that the observable phenomena are limited to those which produce changes in its average charge state. One possible system would be a single quantum dot. By tuning its tunnel barriers, most signatures visible in a transport measurement could be made to result in a change of charge state. Investigating a dot with cold reservoirs could provide further insight into interactions between the two, such as the Kondo effect. More complicated systems could also be measured. For example, previous experiments have demonstrated that point-contact detectors can be used to observe the current through a double dot [140], the charge states of a quantum-cellular-automata cell [144], and single-particle interference via the Aharonov-Bohm effect [145].

If a bias voltage is applied across the device under test, a current may be able



**Figure 5.5:** Results of single-electron counting with the point-contact detector. For this experiment the dot was tuned to have a single dominant tunnel barrier. The average QPC current over a single charge-state transition in the dot is shown in (b), along with a fitted Fermi function (black line). Each point is the average of 14 s of data. A constant linear background has been subtracted from the line-shape. An example of the measured QPC current (taken from  $V_{L-PL} = -0.4333$  V) is given in (a). The signal shows switching between two distinct states, reflecting the real-time changes in the dot's charge-state. The statistics of  $t_{\text{on}}$  over 14 s of data at  $V_{L-PL} = -0.4333$  V are shown in (c). As expected, the probability for an electron to dwell on the dot falls exponentially with time. Fitting an exponential decay to the data (the red line) gives a tunnel rate for the dominant barrier of  $\Gamma_{\text{off}} = 79$  Hz. In the fitting we assume an error on each point proportional to  $1/\sqrt{N}$ , where  $N$  is the point's value.



**Figure 5.6:** The two large squares depict the cooled 2D regions. A cooling current passes through each region via a pair of quantum dots (circles). By choosing appropriately the potentials of the four external reservoirs ( $V_{S1}$ ,  $V_{S2}$ ,  $V_{D1}$ ,  $V_{D2}$ ), the cooled source and drain may have an arbitrary bias voltage between them. A proximal point-contact detector is used as a non-invasive probe of the charge state of the device under test (DUT).

to flow between the cooled reservoirs. Not only must this current remain small compared to the cooling currents but, if temperatures are to remain constant in the system, the associated heating must also be significantly less than the available cooling power. It is not possible to have both a high biases and strong coupling to the reservoir in a device under test. As an quantitative example, we consider the limitations on the applied bias and tunnel couplings for a single quantum dot placed between the reservoirs.

In the limit that the bias is much greater than the thermal broadening of the reservoirs ( $|eV_{SD}| \gg k_B T$ ), the maximum heat that a dot can dissipate in a single reservoir is approximately  $(\Gamma/2)|eV_{SD}|$  (where  $\Gamma$  is the tunnel rate of both dot barriers). We use an approximate expression from Edwards [2] for the cooling power of the current through a QDR:  $\dot{Q}_T = (0.31 \text{ pW/K}^2) \cdot T^2$ . Given that the heating from the dot must be much less than  $\dot{Q}_T$ , the following relation is true:

$$\Gamma V_{SD} \ll (0.62 \text{ pW/K}^2) \frac{T^2}{e} \quad (5.3)$$

At 100 mK, this implies that  $\Gamma V_{SD} \ll 40 \text{ MHz} \cdot \text{mV}$ , while at 1 mK the result is  $\Gamma V_{SD} \ll 4 \text{ kHz} \cdot \text{mV}$ . The dot must therefore become more isolated from the reservoirs as their temperature reduces in order to avoid excess heating. Alternatively, the maximum applied bias must be reduced. For a given bias (coupling), the dot's

tunnel coupling (bias) must decrease as  $T^2$ . Similar considerations must be taken for whatever device is to be placed between the biased reservoirs.

As well as using QDRs to cool the environment for other nano-scale electronic devices, it may be possible that a QDR device could be a useful tool for investigating various properties of 2D electron gases. For example, in the out-of-equilibrium regime, the distribution of occupied states in the isolated region of a QDR will be strongly affected by electron-electron scattering processes. By using a third dot to measure the shape of this distribution, the dependence of scattering on energy, temperature and, magnetic field could be characterised.

# Chapter 6

## Conclusions

---

In this thesis we have presented the design, fabrication and experimental investigation of a device for cooling an isolated  $6 \mu\text{m}^2$  two-dimensional electron gas (2DEG) using the energy-selective transport of electrons through a pair of quantum dots. This Quantum Dot Refrigerator (QDR) scheme was first suggested by Edwards et al. in 1993 [1, 2], but to our knowledge this is the first time it has been realised in practice.

Initial measurements of the device showed it to satisfy all the known requirements for achieving refrigeration: the  $6 \mu\text{m}^2$  region was large enough to be treated as a 2D electron gas, and the quantum dots were small enough to have widely spaced single-particle states. However, a complication arose because of the strength of the electrostatic interactions in the system. It was found that not only did the isolated 2DEG possess a significant charging energy, but also that charging either of the adjacent quantum dots with a single extra electron caused the isolated 2DEG's energy to increase by a significant amount. This capacitive coupling invalidated one of the fundamental assumptions of the original work of Edwards, namely that the cooled 2DEG be at a constant energy.

To ascertain whether a QDR could still function with significant capacitive coupling between its components, a model that took account of the electrostatic interactions in the system was developed. The results of the model indicated that the QDR could indeed still function successfully, with the coupling causing only a slight decrease in the cooling power.

While a QDR should still work in the presence of strong electrostatic interactions, it invalidated the planned scheme for measuring the temperature of the

isolated 2DEG. The preferred method for measuring this temperature would be to use a third quantum dot, weakly coupled to the isolated 2DEG. However, this cannot work if changes in the charge state of the dot alter the energy of the 2DEG it is probing. Using predictions from the model, an alternative method of determining the temperature was identified. It was found that the line-shape of the current through the QDR, as a function of the electrochemical potentials of the two dots involved in cooling, is directly affected by the temperature of the isolated 2DEG. In fact, if the QDR is successful in cooling, the line-shape will be affected by the *changing* temperature of the isolated 2DEG. By including in the model the change in temperature as a function of the electrochemical potentials of the dots, it was possible to predict how the line-shapes would be affected by different amounts of cooling.

We found that the behaviour of our device is well explained by the QDR model at ambient electron temperatures above approximately 120 mK. In the best cases, the data are consistent with cooling of the isolated 2DEG by up to 100 mK at ambient temperatures around 250 mK. Below ambient electron temperatures of approximately 120 mK the model does not provide a good description of the data. The most likely reason for this was identified as being the reduction in the rate of electron-electron scattering to below the rate at which electrons are injected and removed from the 2DEG. This is not a fundamental limitation for QDRs: the accessible base temperature can be lowered arbitrarily by increasing the size of the cooled region. This introduces more states to participate in scattering. Of course, increasing the 2DEG area also increases its thermal contact with the lattice, which necessitates a lower operating temperature. We conclude that the isolated 2DEG area in our device is best suited to operating at temperatures around 250 mK or above.

Finally, we explored future approaches for studying QDRs. In particular, an experimental demonstration showed how an additional quantum dot would be used as an independent thermometer of the isolated 2DEG. This would provide a superior measurement of a device's behaviour in all its regimes of operation (equilibrium, quasi-equilibrium, and out-of-equilibrium). However, to use this scheme would require the capacitance of the isolated 2DEG to be significantly increased in order to keep its potential constant. This could be done by fabricating a large area surface gate above it.

It may also be possible to use the cooled 2DEGs of one or more QDRs to provide

cold reservoirs for an arbitrary nano-scale device. We showed that this is viable, as long as the bias between the cooled 2DEGs and the conductance of the device are both kept low enough to avoid excessive heating.

In summary, we believe the work we have presented in this thesis demonstrates, both theoretically and experimentally, that electronic cooling with quantum dots is a practical reality. We have shown that, as a technique for cooling semiconductor 2DEGs in the mK regime, it has significant advantages over other electronic refrigeration mechanisms. It may also eventually prove preferable to standard refrigeration methods, which require a good thermal contact between the 2DEG and a separate cold bath. Hopefully further study of QDRs will result in a more rigorous understanding of their limitations, improvements in performance, and perhaps new insights into the flow of heat in low-dimensional electronic systems.

# Appendix A

## Wafers and devices

---

### A.1 Wafers

Wafer	$\mu / \text{cm}^2\text{V}^{-1}\text{s}^{-1}$	$n / \text{cm}^{-2}$	$E_F / \text{meV}$
<i>T567</i> : 90nm HEMT (see Figure A.1).	$1.25 \cdot 10^6$	$1.37 \cdot 10^{11}$	4.68
<i>A3589</i> : 90nm HEMT (see Figure A.1).	$0.93 \cdot 10^6$	$1.7 \cdot 10^{11}$	6.1

### A.2 Devices

Device	Experiment	Wafer	Gate metal
<i>dc5-4a</i>	QDR.	<i>T567</i>	Ti/Au
<i>dc-test1-2a</i>	Quantum dot thermometer test.	<i>A3589</i>	NiCr/Au

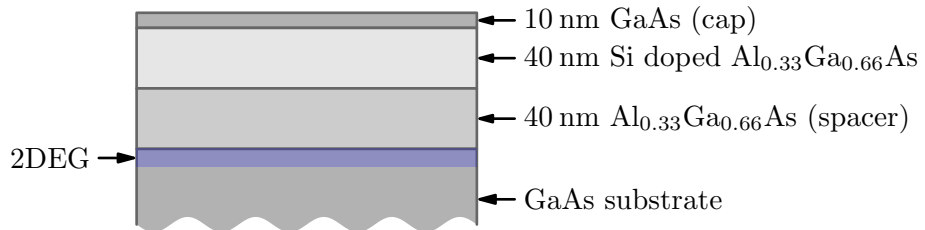


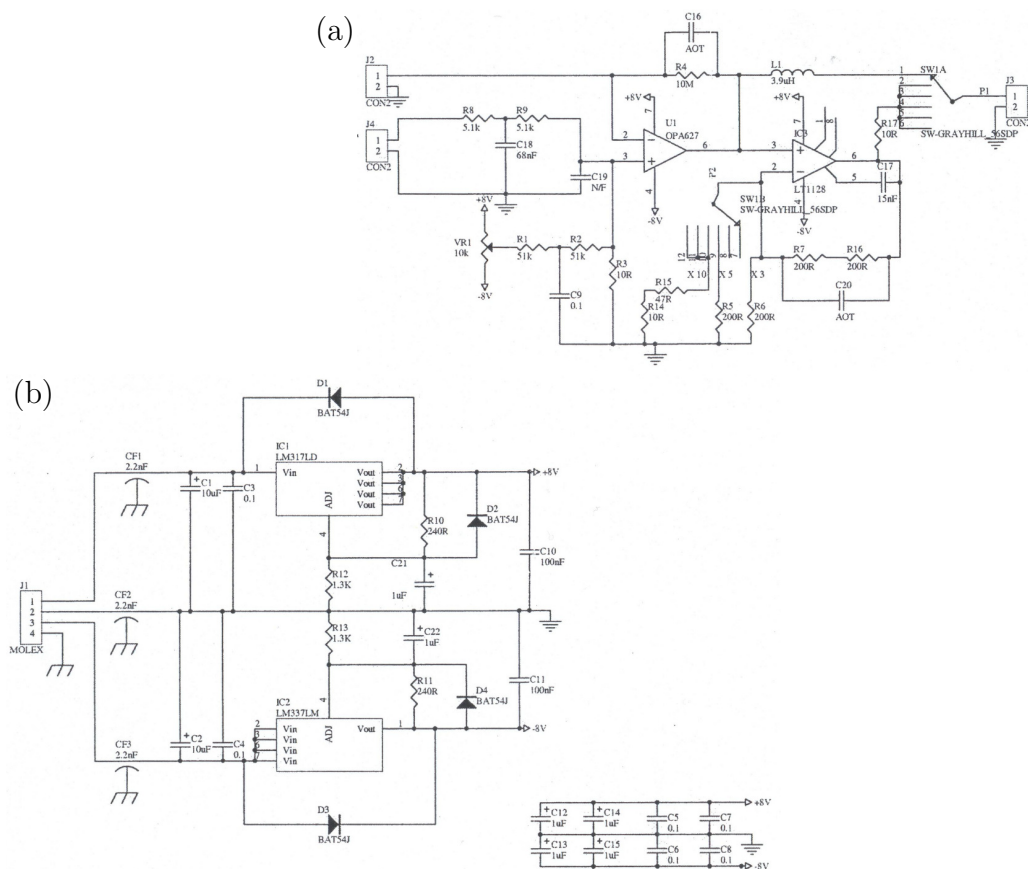
**Figure A.1:** Layers of a standard 90nm HEMT.

# Appendix B

## Measurement setup

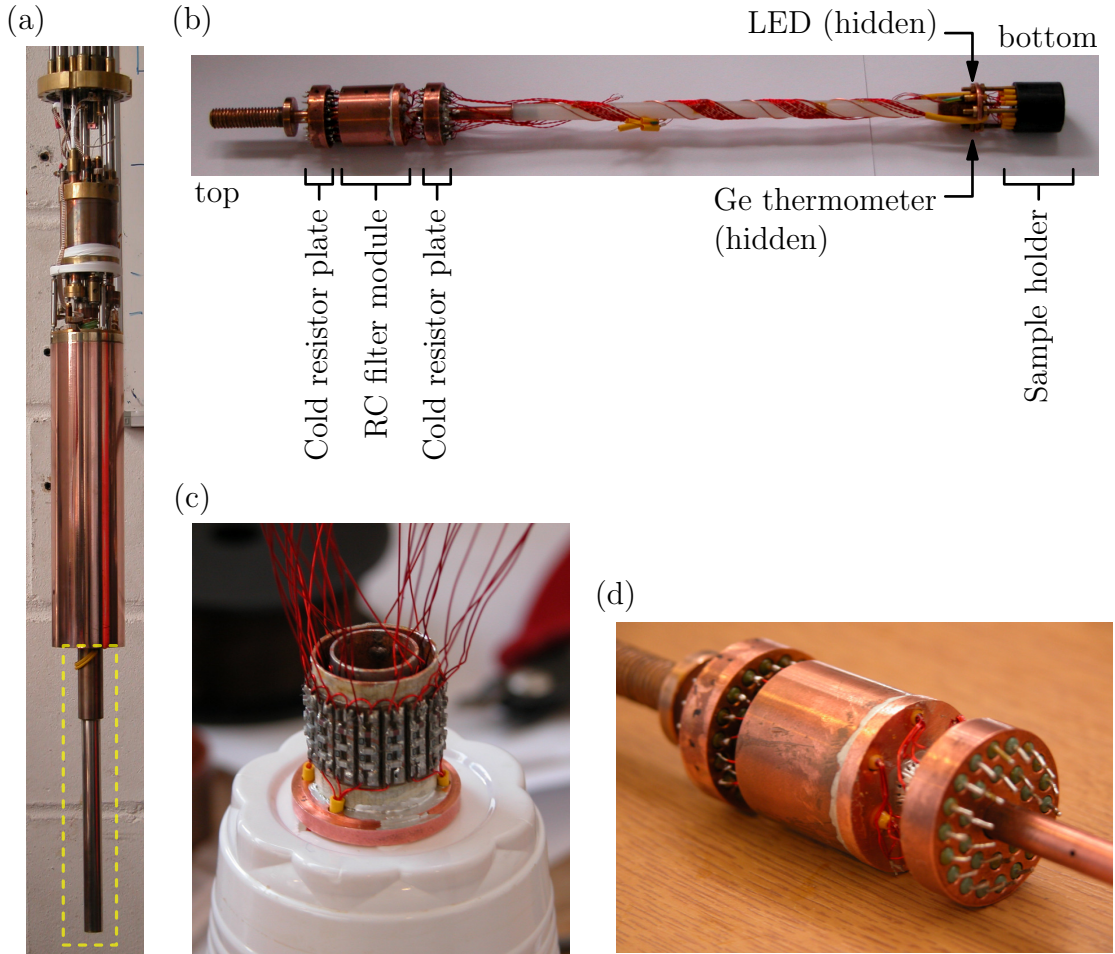
---

### B.1 Current-to-voltage amplifier



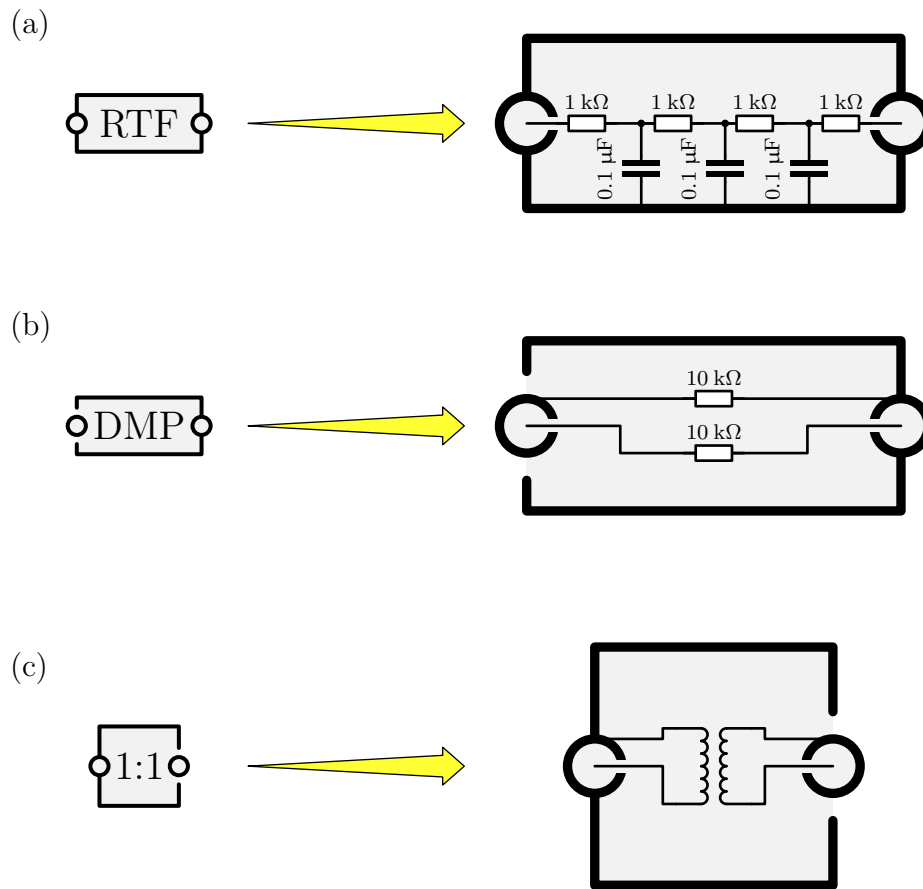
*J883* preamplifier, designed by the Cavendish electronics workshop. The amplifier is shown in (a), and (b) shows the regulation and conditioning of the supply voltages.

## B.2 Cold finger



(a) Dilution fridge used in the QDR experiment. The yellow box indicates the metal shield around the cold finger. (b) The cold finger. When in use, the metal shield fits tightly around the cold resistor plates and the RC filter module. Measurement wires enter the shield above the first resistor plate and pass through a resistor in both plates and a 3-pole RC filter in the filter module before connecting to the sample. (c) The filter module under construction. Each filter is fabricated on an individual PCB using surface-mount components. ( $200\ \Omega$  metal film resistors and COG dielectric capacitors. The capacitances of the three poles were  $100\ \text{pF}$ ,  $10\ \text{pF}$  and  $1\ \text{pF}$ . This filter is inspired by a design by Ron Potok [146].) The filter boards are affixed to two concentric copper tubes, and a third tube eventually encloses both. After assembly, the spaces between the tubes were filled with copper-matched Stycast to improve the heat-sinking of the filter components. (d) The upper part of the cold finger. The  $200\ \Omega$  resistors that feed through the resistor plates have their normal encapsulation removed and are potted in place with GE varnish. This method was first used in Charlie Marcus' lab [147].

### B.3 Room temperature electronics



Various modules used in the room temperature measurement setups. The black bounding boxes depict metal enclosures, and the circular connection nodes are BNC sockets. (a) 3-pole low-pass filter with a cut-off frequency of 10 kHz. (b) In-line resistors for the signal and ground of a coaxial line (for damping vibrations that occur when the *J883* amplifier drives the capacitive load of the screened room filters). (c) 1-to-1 audio-frequency transformer, for isolating the ground of a lock-in excitation from the rest of the circuit.

The ‘A-B’ module (not shown) simply routes the inner and outer of one coaxial connection to the inners of two further coaxial connections. The metal enclosure is connected to the outers of these last two connections, but isolated from the outer of the first.

# Appendix C

## 2DEG thermal coupling

---

Figure C.1 shows the calculated heat flows for a typical device. (The device geometry is based on the *JStar* optical mask.) The heat flow between the 2DEG and the lattice is characterised by the constant  $40 \text{ fW}\mu\text{m}^{-2}\text{K}^{-5}$  (see Section 2.3.2), and a 2DEG area of approximately  $(3 \cdot 10^6) \mu\text{m}^2$ . The heat flow between the ohmic contacts and the lattice is found assuming a total volume of  $(5 \cdot 10^4) \mu\text{m}^3$  and using the electron-phonon coupling constant for Au:  $(2.4 \cdot 10^6) \text{ fW}\mu\text{m}^{-3}\text{K}^{-5}$  [148, 96]. The heat flow between the 2DEG and the electron gas in the ohmic contacts is calculated using the Wiedemann-Franz law, for electrical resistances of both  $1 \text{ k}\Omega$  and  $10 \text{ k}\Omega$  for each of the 20 contacts.

The thermal coupling between the ohmics and the lattice is consistently three orders of magnitude greater than the coupling between the 2DEG and the lattice. It is therefore reasonable to assume that, unless the electron temperature of the 2DEG is found to be greatly elevated, there is unlikely to be sufficient power being dissipated in the device to drive the electron gas in the ohmic contacts away from the lattice temperature. However, the strong thermalisation in the ohmics does not necessarily lead to efficient cooling of the 2DEG, because the electrical resistance between the two limits their thermal contact. For the particular parameters in this calculation, and ohmic resistances of  $1 \text{ k}\Omega$ , we find that cooling through the ohmics will dominate for small increases in 2DEG electron temperature, but for  $T_e > 120 \text{ mK}$  the cooling will be mainly via coupling to the lattice phonons. For ohmic resistances of  $10 \text{ k}\Omega$ , the electron-phonon coupling is always dominant. This suggests that low ohmic contact resistances ( $< 1 \text{ k}\Omega$ ) should result in reduced electron temperatures.

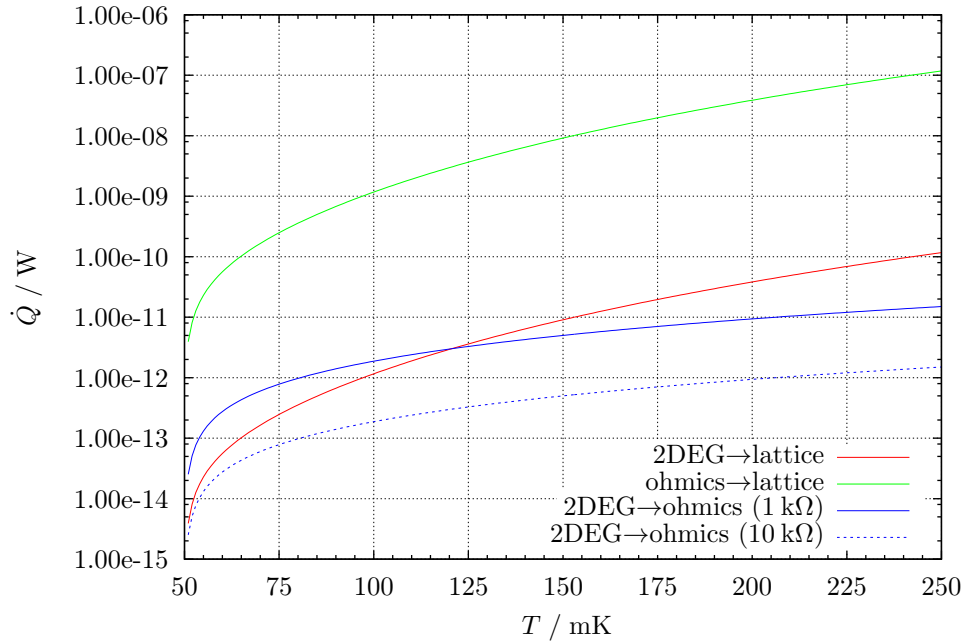


**Figure C.1:** Calculated heat flows between the ohmic contacts, 2DEG, and lattice of a typical device. For the ‘2DEG→lattice’ and ‘ohmics→lattice’ heat flows, the lattice temperature is 50 mK and the 2DEG or ohmic temperature is the  $x$ -axis. For the ‘2DEG→ohmics’ flow, the ohmic temperature is 50 mK and the 2DEG temperature is the  $x$ -axis.

# References

---

- [1] H. L. Edwards, Q. Niu, and A. L. de Lozanne. *A quantum-dot refrigerator*. Appl. Phys. Lett., **63**(13), 1815 (1993).
- [2] H. L. Edwards, Q. Niu, G. A. Georgakis, and A. L. de Lozanne. *Cryogenic cooling using tunneling structures with sharp energy features*. Phys. Rev. B, **52**(8), 5714 (1995).
- [3] K. von Klitzing, G. Dorda, and M. Pepper. *New Method for High-Accuracy Determination of the Fine-Structure Constant Based on Quantized Hall Resistance*. Phys. Rev. Lett., **45**(6), 494 (1980).
- [4] M. Dolev, M. Heiblum, V. Umansky, A. Stern, and D. Mahalu. *Observation of a quarter of an electron charge at the  $\nu = 5/2$  quantum Hall state*. Nature, **452**(7189), 829 (2008).
- [5] R. M. Potok, I. G. Rau, H. Shtrikman, Y. Oreg, and D. Goldhaber-Gordon. *Observation of the two-channel Kondo effect*. Nature, **446**, 167 (2007).
- [6] M. T. Björk, C. Thelander, A. E. Hansen, L. E. Jensen, M. W. Larsson, L. R. Wallenberg, and L. Samuelson. *Few-Electron Quantum Dots in Nanowires*. Nano Lett., **4**(9), 1621 (2004).
- [7] M. J. Biercuk, S. Garaj, N. Mason, J. M. Chow, and C. M. Marcus. *Gate-Defined Quantum Dots on Carbon Nanotubes*. Nano Lett., **5**(7), 1267 (2005).
- [8] D. C. Tsui, H. L. Stormer, and A. C. Gossard. *Two-Dimensional Magnetotransport in the Extreme Quantum Limit*. Phys. Rev. Lett., **48**(22), 1559 (1982).

- 
- [9] Y. K. Kato, R. C. Myers, A. C. Gossard, and D. D. Awschalom. *Observation of the Spin Hall Effect in Semiconductors*. *Science*, **306**(5703), 1910 (2004).
- [10] J. Wunderlich, B. Kaestner, J. Sinova, and T. Jungwirth. *Experimental Observation of the Spin-Hall Effect in a Two-Dimensional Spin-Orbit Coupled Semiconductor System*. *Phys. Rev. Lett.*, **94**(4), 047204 (2005).
- [11] C. G. Smith. *Low-dimensional quantum devices*. *Rep. Prog. Phys.*, **59**(2), 235 (1996).
- [12] H. van Houten, C. W. J. Beenakker, J. G. Williamson, M. E. I. Broekaart, P. H. M. van Loosdrecht, B. J. van Wees, J. E. Mooij, C. T. Foxon, and J. J. Harris. *Coherent electron focusing with quantum point contacts in a two-dimensional electron gas*. *Phys. Rev. B*, **39**(12), 8556 (1989).
- [13] C. J. B. Ford, S. Washburn, M. Büttiker, C. M. Knoedler, and J. M. Hong. *Influence of geometry on the Hall effect in ballistic wires*. *Phys. Rev. Lett.*, **62**(23), 2724 (1989).
- [14] J. Spector, H. L. Stormer, K. W. Baldwin, L. N. Pfeiffer, and K. W. West. *Control of ballistic electrons in macroscopic two-dimensional electron systems*. *Appl. Phys. Lett.*, **56**(10), 967 (1990).
- [15] G. Timp, A. M. Chang, J. E. Cunningham, T. Y. Chang, P. Mankiewich, R. Behringer, and R. E. Howard. *Observation of the Aharonov-Bohm effect for  $\omega_c\tau > 1$* . *Phys. Rev. Lett.*, **58**(26), 2814 (1987).
- [16] C. J. B. Ford, T. J. Thornton, R. Newbury, M. Pepper, H. Ahmed, D. C. Peacock, D. A. Ritchie, J. E. F. Frost, and G. A. C. Jones. *Electrostatically defined heterojunction rings and the Aharonov-Bohm effect*. *Appl. Phys. Lett.*, **54**(1), 21 (1989).
- [17] B. J. van Wees, H. van Houten, C. W. J. Beenakker, J. G. Williamson, L. P. Kouwenhoven, D. van der Marel, and C. T. Foxon. *Quantized conductance of point contacts in a two-dimensional electron gas*. *Phys. Rev. Lett.*, **60**(9), 848 (1988).
- [18] D. A. Wharam, T. J. Thornton, R. Newbury, M. Pepper, H. Ahmed, J. E. F. Frost, D. G. Hasko, D. C. Peacock, D. A. Ritchie, and G. A. C. Jones. *One-dimensional transport and the quantisation of the ballistic resistance*. *J. Phys. C: Sol. Stat. Phys.*, **21**(8), L209 (1988).

- 
- [19] C. G. Smith, M. Pepper, H. Ahmed, J. E. F. Frost, D. G. Hasko, D. C. Peacock, D. A. Ritchie, and G. A. C. Jones. *The transition from one- to zero-dimensional ballistic transport*. J. Phys. C: Sol. Stat. Phys., **21**(24), L893 (1988).
- [20] B. J. van Wees, L. P. Kouwenhoven, C. J. P. M. Harmans, J. G. Williamson, C. E. Timmering, M. E. I. Broekaart, C. T. Foxon, and J. J. Harris. *Observation of zero-dimensional states in a one-dimensional electron interferometer*. Phys. Rev. Lett., **62**(21), 2523 (1989).
- [21] U. Meirav, M. A. Kastner, and S. J. Wind. *Single-electron charging and periodic conductance resonances in GaAs nanostructures*. Phys. Rev. Lett., **65**(6), 771 (1990).
- [22] M. A. Reed, J. N. Randall, R. J. Aggarwal, R. J. Matyi, T. M. Moore, and A. E. Wetsel. *Observation of discrete electronic states in a zero-dimensional semiconductor nanostructure*. Phys. Rev. Lett., **60**(6), 535 (1988).
- [23] A. T. Johnson, L. P. Kouwenhoven, W. de Jong, N. C. van der Vaart, C. J. P. M. Harmans, and C. T. Foxon. *Zero-dimensional states and single electron charging in quantum dots*. Phys. Rev. Lett., **69**(10), 1592 (1992).
- [24] J. Weis, R. J. Haug, K. v. Klitzing, and K. Ploog. *Transport spectroscopy of a confined electron system under a gate tip*. Phys. Rev. B, **46**(19), 12837 (1992).
- [25] E. B. Foxman, P. L. McEuen, U. Meirav, N. S. Wingreen, Y. Meir, P. A. Belk, N. R. Belk, M. A. Kastner, and S. J. Wind. *Effects of quantum levels on transport through a Coulomb island*. Phys. Rev. B, **47**(15), 10020 (1993).
- [26] M. A. Kastner. *The single-electron transistor*. Rev. Mod. Phys., **64**(3), 849 (1992).
- [27] U. Meirav and E. B. Foxman. *Single-electron phenomena in semiconductors*. Semicond. Sci. Technol., **11**, 255 (1996).
- [28] L. Kouwenhoven, C. Marcus, P. McEuen, S. Tarucha, R. Westervelt, and N. Wingreen. *Electron transport in quantum dots*. Mesoscopic Electron Transport, **345**, 16 (1997).
- [29] W. G. van der Wiel, S. De Franceschi, J. M. Elzerman, T. Fujisawa, S. Tarucha, and L. P. Kouwenhoven. *Electron transport through double quantum dots*. Rev. Mod. Phys., **75**(1), 1 (2002).
- [30] R. Hanson, L. P. Kouwenhoven, J. R. Petta, S. Tarucha, and L. M. K. Vandersypen. *Spins in few-electron quantum dots*. Rev. Mod. Phys., **79**, 1217 (2007).

- 
- [31] R. I. Shekhter. *Zero anomalies in the resistance of a tunnel junction containing metallic inclusions in the oxide layer*. Soviet Physics JETP, **36**(4), 747 (1973).
- [32] I. O. Kulik and R. I. Shekhter. *Kinetic phenomena and charge discreteness effects in granulated media*. Soviet Physics JETP, **41**(2), 309 (1975).
- [33] S. Tarucha, D. G. Austing, T. Honda, R. J. van der Hage, and L. P. Kouwenhoven. *Shell Filling and Spin Effects in a Few Electron Quantum Dot*. Phys. Rev. Lett., **77**(17), 3613 (1996).
- [34] S. M. Reimann and M. Manninen. *Electronic structure of quantum dots*. Rev. Mod. Phys., **74**(4), 1283 (2002).
- [35] C. W. J. Beenakker. *Theory of Coulomb-blockade oscillations in the conductance of a quantum dot*. Phys. Rev. B, **44**(4), 1646 (1991).
- [36] D. V. Averin, A. N. Korotkov, and K. K. Likharev. *Theory of single-electron charging of quantum wells and dots*. Phys. Rev. B, **44**(12), 6199 (1991).
- [37] D. V. Averin and K. K. Likharev. *Mesoscopic phenomena in solids* (Elsevier Science, Amsterdam), chap. 6, pp. 173–271 (1991).
- [38] C. Fühner. *Investigations on Multi-Electron Quantum Dots: Coulomb Blockade, Kondo Effect, and Fano Regime*. Ph.D. thesis, University of Hannover (2002).
- [39] D. V. Averin and Y. V. Nazarov. *Virtual electron diffusion during quantum tunneling of the electric charge*. Phys. Rev. Lett., **65**(19), 2446 (1990).
- [40] L. J. Geerligs, D. V. Averin, and J. E. Mooij. *Observation of macroscopic quantum tunneling through the Coulomb energy barrier*. Phys. Rev. Lett., **65**(24), 3037 (1990).
- [41] S. De Franceschi, S. Sasaki, J. M. Elzerman, W. G. van der Wiel, S. Tarucha, and L. P. Kouwenhoven. *Electron Cotunneling in a Semiconductor Quantum Dot*. Phys. Rev. Lett., **86**(5), 878 (2001).
- [42] P. W. Anderson. *Localized Magnetic States in Metals*. Phys. Rev., **124**(1), 41 (1961).
- [43] D. Goldhaber-Gordon, H. Shtrikman, D. Mahalu, D. Abusch-Magder, U. Meirav, and M. A. Kastner. *Kondo effect in a single-electron transistor*. Nature, **391**, 156 (1998).
- [44] S. M. Cronenwett, T. H. Oosterkamp, and L. P. Kouwenhoven. *A Tunable Kondo Effect in Quantum Dots*. Science, **281**(5376), 540 (1998).

- 
- [45] J. Schmid, J. Weis, K. Eberl, and K. v. Klitzing. *A quantum dot in the limit of strong coupling to reservoirs*. Physica B: Condensed Matter, **256-258**, 182 (1998).
- [46] E. B. Foxman, U. Meirav, P. L. McEuen, M. A. Kastner, O. Klein, P. A. Belk, D. M. Abusch, and S. J. Wind. *Crossover from single-level to multilevel transport in artificial atoms*. Phys. Rev. B, **50**(19), 14193 (1994).
- [47] M. Field, C. G. Smith, M. Pepper, D. A. Ritchie, J. E. F. Frost, G. A. C. Jones, and D. G. Hasko. *Measurements of Coulomb blockade with a noninvasive voltage probe*. Phys. Rev. Lett., **70**(9), 1311 (1993).
- [48] R. Schleser, E. Ruh, T. Ihn, K. Ensslin, D. C. Driscoll, and A. C. Gossard. *Time-resolved detection of individual electrons in a quantum dot*. Appl. Phys. Lett., **85**(11), 2005 (2004).
- [49] L. M. K. Vandersypen, J. M. Elzerman, R. N. Schouten, L. H. W. van Beveren, R. Hanson, and L. P. Kouwenhoven. *Real-time detection of single-electron tunneling using a quantum point contact*. Appl. Phys. Lett., **85**(19), 4394 (2004).
- [50] S. Gustavsson, R. Leturcq, B. Simovic, R. Schleser, T. Ihn, P. Studerus, K. Ensslin, D. C. Driscoll, and A. C. Gossard. *Counting Statistics of Single Electron Transport in a Quantum Dot*. Phys. Rev. Lett., **96**(7), 076605 (2006).
- [51] T. Fujisawa, T. Hayashi, R. Tomita, and Y. Hirayama. *Bidirectional Counting of Single Electrons*. Science, **312**(5780), 1634 (2006).
- [52] B. L. Altshuler and A. G. Aronov. *Electron-Electron Interaction in Disordered Systems* (Elsevier, Amsterdam), chap. 1 (1985).
- [53] L. Zheng and S. Das Sarma. *Coulomb scattering lifetime of a two-dimensional electron gas*. Phys. Rev. B, **53**(15), 9964 (1996).
- [54] T. Jungwirth and A. H. MacDonald. *Electron-electron interactions and two-dimensional two-dimensional tunneling*. Phys. Rev. B, **53**(11), 7403 (1996).
- [55] G. F. Giuliani and J. J. Quinn. *Lifetime of a quasiparticle in a two-dimensional electron gas*. Phys. Rev. B, **26**(8), 4421 (1982).
- [56] A. Yacoby, M. Heiblum, H. Shtrikman, V. Umansky, and D. Mahalu. *Dephasing of ballistic electrons as a function of temperature and carrier density*. Semicond. Sci. Technol., **9**(5S), 907 (1994).
- [57] A. G. Huibers, M. Switkes, C. M. Marcus, K. Campman, and A. C. Gossard. *Dephasing in Open Quantum Dots*. Phys. Rev. Lett., **81**(1), 200 (1998).

- 
- [58] A. G. Huibers, J. A. Folk, S. R. Patel, C. M. Marcus, C. I. Duruöz, and J. S. Harris. *Low-Temperature Saturation of the Dephasing Time and Effects of Microwave Radiation on Open Quantum Dots*. Phys. Rev. Lett., **83**(24), 5090 (1999).
- [59] S. Q. Murphy, J. P. Eisenstein, L. N. Pfeiffer, and K. W. West. *Lifetime of two-dimensional electrons measured by tunneling spectroscopy*. Phys. Rev. B, **52**(20), 14825 (1995).
- [60] N. Turner, J. T. Nicholls, E. H. Linfield, K. M. Brown, G. A. C. Jones, and D. A. Ritchie. *Tunneling between parallel two-dimensional electron gases*. Phys. Rev. B, **54**(15), 10614 (1996).
- [61] N. J. Appleyard, J. T. Nicholls, M. Y. Simmons, W. R. Tribe, and M. Pepper. *Thermometer for the 2D Electron Gas using 1D Thermopower*. Phys. Rev. Lett., **81**(16), 3491 (1998).
- [62] P. J. Price. *Hot electrons in a GaAs heterolayer at low temperature*. J. Appl. Phys., **53**(10), 6863 (1982).
- [63] N. W. Ashcroft and N. D. Mermin. *Solid state physics* (Thomson Learning), chap. 22, pp. 422–450 (1976).
- [64] U. Sivan, M. Heiblum, and C. P. Umbach. *Hot ballistic transport and phonon emission in a two-dimensional electron gas*. Phys. Rev. Lett., **63**(9), 992 (1989).
- [65] H. L. Stormer, L. N. Pfeiffer, K. W. Baldwin, and K. W. West. *Observation of a Bloch-Grüneisen regime in two-dimensional electron transport*. Phys. Rev. B, **41**(2), 1278 (1990).
- [66] B. K. Ridley. *Hot electrons in low-dimensional structures*. Rep. Prog. Phys., **54**(2), 169 (1991).
- [67] Y. Y. Proskuryakov, J. T. Nicholls, D. I. Hadji-Ristic, A. Kristensen, and C. B. S. rensen. *Energy-loss rate of a two-dimensional electron gas measured using a mesoscopic thermometer*. Phys. Rev. B, **75**(4), 045308 (2007).
- [68] C. Jasiukiewicz and V. Karpus. *Electron energy relaxation rate: the influence of acoustic phonon spectrum anisotropy*. Semicond. Sci. Technol., **11**(12), 1777 (1996).
- [69] A. Mittal, R. J. Zieve, D. E. Prober, R. G. Wheeler, and R. N. Sacks. *Electron-Phonon Scattering and Heat Flow in GaAs/AlGaAs 2DEG Samples below 0.5K*. APS Meeting Abstracts, pp. K1401+ (1996).

- 
- [70] F. F. Ouali, H. R. Francis, and H. C. Rhodes. *Acoustic phonon scattering in two dimensional carriers*. Physica B: Condensed Matter, **263**, 239 (1999).
- [71] R. C. Richardson and E. N. Smith (eds.). *Experimental techniques in condensed matter physics at low temperatures* (Addison Wesley), chap. 3.5, pp. 154–165 (1988).
- [72] J. S. Xia, E. D. Adams, V. Shvarts, W. Pan, H. L. Stormer, and D. C. Tsui. *Ultra-low-temperature cooling of two-dimensional electron gas*. Physica B: Condensed Matter, **280**, 491 (2000).
- [73] Y. C. Chung, M. Heiblum, and V. Umansky. *Scattering of Bunched Fractionally Charged Quasiparticles*. Phys. Rev. Lett., **91**(21), 216804 (2003).
- [74] L. W. Molenkamp, T. Gravier, H. van Houten, O. J. A. Buijk, M. A. A. Mabesoone, and C. T. Foxon. *Peltier coefficient and thermal conductance of a quantum point contact*. Phys. Rev. Lett., **68**(25), 3765 (1992).
- [75] A. S. Dzurak, C. G. Smith, L. Martín-Moreno, M. Pepper, D. A. Ritchie, G. A. C. Jones, and D. G. Hasko. *Thermopower of a one-dimensional ballistic constriction in the non-linear regime*. J. Phys.: Condens. Matter, **5**(43), 8055 (1993).
- [76] A. S. Dzurak, C. G. Smith, C. H. W. Barnes, M. Pepper, L. Martín-Moreno, C. T. Liang, D. A. Ritchie, and G. A. C. Jones. *Thermoelectric signature of the excitation spectrum of a quantum dot*. Phys. Rev. B, **55**(16), R10197 (1997).
- [77] A. Staring, L. Molenkamp, B. Alphenaar, H. van Houten, O. Buyk, M. Mabesoone, C. J. Beenakker, and C. Foxon. *Coulomb-blockade oscillations in the thermopower of a quantum dot*. Europhys. Lett., **22**, 57 (1993).
- [78] L. Molenkamp, A. A. M. Staring, B. W. Alphenaar, H. van Houten, and C. W. J. Beenakker. *Sawtooth-like thermopower oscillations of a quantum dot in the Coulomb blockade regime*. Semicond. Sci. Technol., **9**(5S), 903 (1994).
- [79] O. Chiatti, J. T. Nicholls, Y. Y. Proskuryakov, N. Lumpkin, I. Farrer, and D. A. Ritchie. *Quantum Thermal Conductance of Electrons in a One-Dimensional Wire*. Phys. Rev. Lett., **97**(5), 056601 (2006).
- [80] R. Scheibner, H. Buhmann, D. Reuter, M. N. Kiselev, and L. W. Molenkamp. *Thermopower of a Kondo Spin-Correlated Quantum Dot*. Phys. Rev. Lett., **95**(17), 176602 (2005).
- [81] R. Scheibner, M. König, D. Reuter, A. Wieck, H. Buhmann, and L. Molenkamp. *Quantum dot as thermal rectifier*. eprint arXiv: 0703514 (2007).

- 
- [82] S. Goswami, C. Siegert, M. Baenninger, M. Pepper, I. Farrer, D. A. Ritchie, and A. Ghosh. *Highly Enhanced Thermopower in Two-Dimensional Electron Systems at Millikelvin Temperatures*. Phys. Rev. Lett., **103**(2), 026602 (2009).
- [83] J. T. Tuoriniemi, T. A. Knuuttila, K. Lefmann, K. K. Nummila, W. Yao, and F. B. Rasmussen. *Double-Spin-Flip Resonance of Rhodium Nuclei at Positive and Negative Spin Temperatures*. Phys. Rev. Lett., **84**(2), 370 (2000).
- [84] H. J. Goldsmid. *CRC Handbook of Thermoelectrics* (CRC Press), chap. 3, pp. 19–26 (1995).
- [85] S. R. Harutyunyan, V. H. Vardanyan, A. S. Kuzanyan, V. R. Nikoghosyan, S. Kunii, K. S. Wood, and A. M. Gulian. *Thermoelectric cooling at cryogenic temperatures*. Appl. Phys. Lett., **83**(11), 2142 (2003).
- [86] A. Shakouri and J. E. Bowers. *Heterostructure integrated thermionic coolers*. Appl. Phys. Lett., **71**(9), 1234 (1997).
- [87] G. D. Mahan and L. M. Woods. *Multilayer Thermionic Refrigeration*. Phys. Rev. Lett., **80**(18), 4016 (1998).
- [88] G. D. Mahan. *Thermionic refrigeration*. J. Appl. Phys., **76**(7), 4362 (1994).
- [89] A. Shakouri, C. LaBounty, J. Piprek, P. Abraham, and J. E. Bowers. *Thermionic emission cooling in single barrier heterostructures*. Appl. Phys. Lett., **74**(1), 88 (1999).
- [90] G. Zeng, A. Shakouri, C. Bounty, G. Robinson, E. Croke, P. Abraham, X. Fan, H. Reese, and J. Bowers. *SiGe micro-cooler*. Electronics Letters, **35**(24), 2146 (1999).
- [91] J. Zhang, N. G. Anderson, and K. M. Lau. *AlGaAs superlattice microcoolers*. Appl. Phys. Lett., **83**(2), 374 (2003).
- [92] Y. Hishinuma, T. H. Geballe, B. Y. Mozyshes, and T. W. Kenny. *Measurements of cooling by room-temperature thermionic emission across a nanometer gap*. J. Appl. Phys., **94**(7), 4690 (2003).
- [93] A. N. Korotkov and K. K. Likharev. *Possible cooling by resonant Fowler-Nordheim emission*. Appl. Phys. Lett., **75**(16), 2491 (1999).
- [94] S. O. Valenzuela, W. D. Oliver, D. M. Berns, K. K. Berggren, L. S. Levitov, and T. P. Orlando. *Microwave-Induced Cooling of a Superconducting Qubit*. Science, **314**(5805), 1589 (2006).

- 
- [95] M. Grajcar, S. H. W. van der Ploeg, A. Izmalkov, E. Il'ichev, H.-G. Meyer, A. Fedorov, A. Shnirman, and G. Schon. *Sisyphus cooling and amplification by a superconducting qubit*. Nat. Phys., **4**(8), 612 (2008).
- [96] F. Giazotto, T. T. Heikkilä, A. Luukanen, A. M. Savin, and J. P. Pekola. *Opportunities for mesoscopics in thermometry and refrigeration: Physics and applications*. Rev. Mod. Phys., **78**(1), 217 (2006).
- [97] M. Nahum, T. M. Eiles, and J. M. Martinis. *Electronic microrefrigerator based on a normal-insulator-superconductor tunnel junction*. Appl. Phys. Lett., **65**(24), 3123 (1994).
- [98] R. H. Parmenter. *Enhancement of Superconductivity by Extraction of Normal Carriers*. Phys. Rev. Lett., **7**(7), 274 (1961).
- [99] K. Gray. *Enhancement of superconductivity by quasiparticle tunneling*. Solid State Commun., **26**(10), 633 (1978).
- [100] C. C. Chi and J. Clarke. *Enhancement of the energy gap in superconducting aluminum by tunneling extraction of quasiparticles*. Phys. Rev. B, **20**(11), 4465 (1979).
- [101] R. G. Melton, J. L. Paterson, and S. B. Kaplan. *Superconducting tunnel-junction refrigerator*. Phys. Rev. B, **21**(5), 1858 (1980).
- [102] M. G. Blamire, E. C. G. Kirk, J. E. Evetts, and T. M. Klapwijk. *Extreme critical-temperature enhancement of Al by tunneling in Nb/AlOx/Al/AlOx/Nb tunnel junctions*. Phys. Rev. Lett., **66**(2), 220 (1991).
- [103] D. R. Heslinga and T. M. Klapwijk. *Enhancement of superconductivity far above the critical temperature in double-barrier tunnel junctions*. Phys. Rev. B, **47**(9), 5157 (1993).
- [104] M. M. Leivo, J. P. Pekola, and D. V. Averin. *Efficient Peltier refrigeration by a pair of normal metal/insulator/superconductor junctions*. Appl. Phys. Lett., **68**(14), 1996 (1996).
- [105] R. Leoni, G. Arena, M. G. Castellano, and G. Torrioli. *Electron cooling by arrays of submicron tunnel junctions*. J. Appl. Phys., **85**(7), 3877 (1999).
- [106] P. A. Fisher, J. N. Ullom, and M. Nahum. *High-power on-chip microrefrigerator based on a normal-metal/insulator/superconductor tunnel junction*. Appl. Phys. Lett., **74**(18), 2705 (1999).

- 
- [107] J. P. Pekola, T. T. Heikkilä, A. M. Savin, J. T. Flyktman, F. Giazotto, and F. W. J. Hekking. *Limitations in Cooling Electrons using Normal-Metal-Superconductor Tunnel Junctions*. Phys. Rev. Lett., **92**(5), 056804 (2004).
- [108] H. Pothier, S. Guéron, N. O. Birge, D. Esteve, and M. H. Devoret. *Energy Distribution Function of Quasiparticles in Mesoscopic Wires*. Phys. Rev. Lett., **79**(18), 3490 (1997).
- [109] J. N. Ullom and P. A. Fisher. *Quasiparticle behavior in tunnel junction refrigerators*. Physica B: Condensed Matter, **284-288**(Part 2), 2036 (2000).
- [110] A. M. Clark, A. Williams, S. T. Ruggiero, M. L. van den Berg, and J. N. Ullom. *Practical electron-tunneling refrigerator*. Appl. Phys. Lett., **84**(4), 625 (2004).
- [111] A. J. Manninen, M. M. Leivo, and J. P. Pekola. *Refrigeration of a dielectric membrane by superconductor/insulator/normal-metal/insulator/superconductor tunneling*. Appl. Phys. Lett., **70**(14), 1885 (1997).
- [112] M. M. Leivo, A. J. Manninen, and J. P. Pekola. *Microrefrigeration by normal-metal/insulator/superconductor tunnel junctions*. Appl. Supercond., **5**(7-12), 227 (1997).
- [113] M. M. Leivo and J. P. Pekola. *Thermal characteristics of silicon nitride membranes at sub-Kelvin temperatures*. Appl. Phys. Lett., **72**(11), 1305 (1998).
- [114] J. T. Muhonen, A. O. Niskanen, M. Meschke, Y. A. Pashkin, J. S. Tsai, L. Sainiemi, S. Franssila, and J. P. Pekola. *Electronic cooling of a submicron-sized metallic beam*. Appl. Phys. Lett., **94**(7), 073101 (2009).
- [115] P. J. Koppinen and I. J. Maasilta. *Phonon Cooling of Nanomechanical Beams with Tunnel Junctions*. Phys. Rev. Lett., **102**(16), 165502 (2009).
- [116] A. M. Clark, N. A. Miller, A. Williams, S. T. Ruggiero, G. C. Hilton, L. R. Vale, J. A. Beall, K. D. Irwin, and J. N. Ullom. *Cooling of bulk material by electron-tunneling refrigerators*. Appl. Phys. Lett., **86**(17), 173508 (2005).
- [117] A. J. Ferguson. *Quasiparticle cooling of a single Cooper pair transistor*. Appl. Phys. Lett., **93**(5), 052501 (2008).
- [118] J. M. Rowell and D. C. Tsui. *Hot electron temperature in InAs measured by tunneling*. Phys. Rev. B, **14**(6), 2456 (1976).

- 
- [119] A. M. Savin, M. Prunnila, P. P. Kivinen, J. P. Pekola, J. Ahopelto, and A. J. Manninen. *Efficient electronic cooling in heavily doped silicon by quasiparticle tunneling*. Appl. Phys. Lett., **79**(10), 1471 (2001).
- [120] A. Savin, M. Prunnila, J. Ahopelto, P. Kivinen, P. Trm, and J. Pekola. *Application of superconductor-semiconductor Schottky barrier for electron cooling*. Physica B: Condensed Matter, **329-333**(Part 2), 1481 (2003). Proceedings of the 23rd International Conference on Low Temperature Physics.
- [121] E. A. Johnson. *Low-dimensional semiconductor structures* (Cambridge University Press), chap. 2, pp. 56–78 (2001).
- [122] C. Marcus, S. Patel, A. Huibers, S. Cronenwett, M. Switkes, I. Chan, R. Clarke, J. Folk, S. Godijn, K. Campman, et al. *Quantum Chaos in Open Versus Closed Quantum Dots: Signatures of Interacting Particles*. Chaos, Solitons and Fractals, **8**(7), 1261 (1997).
- [123] C. Wasshuber. *Computational Single-Electronics* (Springer), chap. 2, pp. 9–42 (2001).
- [124] M. J. Hagmann. *Determination of barrier traversal time by modulation of the incident wave*. Appl. Phys. Lett., **62**(2), 199 (1993).
- [125] W. H. Press, B. P. Flannery, S. A. Teukolsky, and W. T. Vetterling. *Numerical Recipes in C* (Cambridge University Press), chap. 2, pp. 32–102 (1992).
- [126] H. Pothier, P. Lafarge, C. Urbina, D. Esteve, and M. H. Devoret. *Single-Electron Pump Based on Charging Effects*. EPL (Europhysics Letters), **17**(3), 249 (1992).
- [127] F. Hofmann, T. Heinzel, D. Wharam, J. Kotthaus, G. Böhm, W. Klein, G. Tränkle, and G. Weimann. *Single electron switching in a parallel quantum dot*. Phys. Rev. B, **51**(19), 13872 (1995).
- [128] A. Vidan, R. M. Westervelt, M. Stopa, M. Hanson, and A. C. Gossard. *Charging and Spin Effects in Triple Dot Artificial Molecules*. J. Supercond., **18**, 223 (2005).
- [129] L. Gaudreau, S. A. Studenikin, A. S. Sachrajda, P. Zawadzki, A. Kam, J. Lapointe, M. Korkusinski, and P. Hawrylak. *Stability Diagram of a Few-Electron Triple Dot*. Phys. Rev. Lett., **97**(3), 036807 (2006).
- [130] D. Schröer, A. D. Greentree, L. Gaudreau, K. Eberl, L. C. L. Hollenberg, J. P. Kotthaus, and S. Ludwig. *Electrostatically defined serial triple quantum dot charged with few electrons*. Phys. Rev. B, **76**(7), 075306 (2007).

- 
- [131] R. L. Kautz, G. Zimmerli, and J. M. Martinis. *Self-heating in the Coulomb-blockade electrometer*. J. Appl. Phys., **73**(5), 2386 (1993).
- [132] A. N. Korotkov, M. R. Samuelsen, and S. A. Vasenko. *Effects of overheating in a single-electron transistor*. J. Appl. Phys., **76**(6), 3623 (1994).
- [133] C. Liu and Q. Niu. *Non-equilibrium effects and self-heating in single-electron Coulomb blockade devices*. Physics Reports, **286**(6), 349 (1997).
- [134] M. Switkes, A. G. Huibers, C. M. Marcus, K. Campman, and A. C. Gossard. *High bias transport and magnetometer design in open quantum dots*. Appl. Phys. Lett., **72**(4), 471 (1998).
- [135] A. Huibers. *Electron transport and dephasing in semiconductor quantum dots*. Ph.D. thesis, Stanford University (1999).
- [136] M. S. Fairbanks, C. A. Marlow, R. P. Taylor, and H. Linke. *Nonlinear characteristics in the magnetoconductance of electron billiards*. Current Applied Physics, **8**(3-4), 340 (2008). AMN-3 (Third International Conference on Advanced Materials and Nanotechnology), Third International Conference on Advanced Materials and Nanotechnology.
- [137] J. P. Pekola, F. Giazotto, and O.-P. Saira. *Radio-Frequency Single-Electron Refrigerator*. Phys. Rev. Lett., **98**(3), 037201 (2007).
- [138] O.-P. Saira, M. Meschke, F. Giazotto, A. M. Savin, M. Möttönen, and J. P. Pekola. *Heat Transistor: Demonstration of Gate-Controlled Electronic Refrigeration*. Phys. Rev. Lett., **99**(2), 027203 (2007).
- [139] Y. Zhang, D. T. McClure, E. M. Levenson-Falk, C. M. Marcus, L. N. Pfeiffer, and K. W. West. *Distinct signatures for Coulomb blockade and Aharonov-Bohm interference in electronic Fabry-Perot interferometers*. Phys. Rev. B, **79**(24), 241304 (2009).
- [140] T. Fujisawa, T. Hayashi, and S. Sasaki. *Time-dependent single-electron transport through quantum dots*. Rep. Prog. Phys., **69**(3), 759 (2006).
- [141] K. MacLean, S. Amasha, I. P. Radu, D. M. Zumbühl, M. A. Kastner, M. P. Hanson, and A. C. Gossard. *Energy-Dependent Tunneling in a Quantum Dot*. Phys. Rev. Lett., **98**(3), 036802 (2007).
- [142] O. Naaman and J. Aumentado. *Poisson Transition Rates from Time-Domain Measurements with a Finite Bandwidth*. Phys. Rev. Lett., **96**(10), 100201 (2006).

- [143] S. Gustavsson, R. Leturcq, M. Studer, I. Shorubalko, T. Ihn, K. Ensslin, D. Driscoll, and A. Gossard. *Electron counting in quantum dots*. Surf. Sci. Rep., **64**(6), 191 (2009).
- [144] F. Perez-Martinez, I. Farrer, D. Anderson, G. A. C. Jones, D. A. Ritchie, S. J. Chorley, and C. G. Smith. *Demonstration of a quantum cellular automata cell in a GaAs/AlGaAs heterostructure*. Appl. Phys. Lett., **91**(3), 032102 (2007).
- [145] S. Gustavsson, R. Leturcq, M. Studer, T. Ihn, K. Ensslin, D. C. Driscoll, and A. C. Gossard. *Time-Resolved Detection of Single-Electron Interference*. Nano Lett., **8**(8), 2547 (2008).
- [146] R. M. Potok. *Probing Many Body Effects in Semiconductor Nanostructures*. Ph.D. thesis, Harvard University (2006).
- [147] A. C. Johnson. *Charge Sensing and Spin Dynamics in GaAs Quantum Dots*. Ph.D. thesis, Harvard University (2005).
- [148] P. M. Echternach, M. R. Thoman, C. M. Gould, and H. M. Bozler. *Electron-phonon scattering rates in disordered metallic films below 1 K*. Phys. Rev. B, **46**(16), 10339 (1992).